MODULATION AND MANIPULATION OF TRANSITION METAL DICHALCOGENIDES

By
Erick C. Sadler

A dissertation submitted to Johns Hopkins University in conformity with the requirements for the degree of Doctor of Philosophy

Baltimore, Maryland
May 2021

Abstract

Low-dimensional Transition metal dichalcogenides (TMDs) have received extensive attention as candidates for a variety of applications such as catalysis, optoelectronics, next generation memory and quantum information technology. The majority of research of low-dimensional TMDs has centered on two-dimensional variants. However, by exploiting substrate – material interactions we have developed novel strategies to control the morphology of TMD materials.

Herein we demonstrate the ability to selectively tune substrate – material interactions to produce a further confinement in the growth of two-dimensional TMDs into confined quasi one-dimensional nanoribbons. We manipulate the growth surface prior to any growth by utilizing PH_3 gas to promote the anisotropic bottom-up growth of these materials. We found that this new surface was tunable and influenced the morphology of the nanoribbons. The nanoribbon width, a key physical characteristic, was manipulated within an order of magnitude by modulating the novel designer surface. Further, these materials demonstrated anomalous optical properties due to their confinement in an additional dimension when compared to their two-dimensional counterparts. These crystals also exhibited high edge fidelity and low defect densities. The material composition was also varied successfully demonstrating the general

applicability of tuning substrate – crystal interactions to direct confined growth of material.

We also found that modulation of the growth parameters can significantly couple with the underlying designer substrate in ways traditional growth substrates cannot. We explored the morphological dependance on growth parameters such as carrier gas flow and composition. The novel labile surfaces employed by our group are sensitive to their reaction environment, allowing the further manipulation of material morphology and therefore properties based on these parameters. This new growth method also showed the ability to selectively disrupt the crystal growth during synthesis of these nanoribbons to achieve desirable widths. This method shows promise for approaching technologically relevant material dimensionality in TMD nanoribbons.

This work offers a unique approach to bottom-up TMD synthesis. By combining gas phase surface reactions with traditional materials science and chemistry routes, we have shown the ability to produce technologically relevant materials that can push the limits of confinement effects in TMD crystals.

Advisor: Professor Thomas J. Kempa
Reader: Professor Howard Fairbrother
Reader: Professor Tyrel McQueen

Acknowledgements

First, I would like to thank my advisor, Professor Thomas. J. Kempa, for his unwavering support during my graduate school tenure. He has been a true mentor in science and beyond.

I want to thank my thesis committee, Professor Tyrel McQueen and Professor Howard Fairbrother, for their support during my time at Johns Hopkins.

Thank you to the Kempa Lab as a whole. It has been an honor to work with this collection of scientists and I truly do not think there could have been any group of people better suited for my time in graduate school.

A special thanks to Tomojit, Jamie, Ben, Eric, and Marta for being my partners for the better part of five years at Johns Hopkins and for being my friends. You all made the Kempa group an exceptionally special place to work and grow and I look forward to seeing what life holds for all of us.

Thank you to my family. Thank you to my father. I know for a certainty I would not be the man I am today, nor would I be writing these acknowledgements without your parenting and guidance over many years. Thank you to my mother who taught me to be resilient through adversity and teaching me that anyone can accomplish their goals with dedication. Thank you to my sister, Nicole. You have always been a source of inspiration in my life and making my little sister proud has always driven me to do the best that I can.

Lastly, I must thank my wife, Kristen. The last 8 years together have been the most incredible journey anyone could ask for. Knowing you has been knowing a true partner and friend. Without your unwavering support, from my undergraduate journey to this point, there is no question I would not have arrived here. Your love is constant source of inspiration and guidance. You have shown me that kindness, humility, and gratitude are truly important no matter what you do. Thank you for making this achievement possible.

Table of Contents

List of Figures

Chapter 1: Introduction to Low-Dimensional Materials

1.1 Introduction to 2D Materials

Nanoscale materials have revealed a plethora of emergent catalytic, optical, biological and electronic phenomena and have become ubiquitous in these fields.[1–6] There exists an increasing need in the fields of catalysis, opto-electronics, and quantum computing that nanoscale materials can fill thanks to their myriad dimensionally-based phenomena. Particularly, 2D materials represent a growing class of materials that have permeated every area of science. The canonical 2D material, graphene, was exfoliated from graphite in 2004.[7] Graphene has since been expanded upon and now there are a wide array of 2D materials with varying chemical compositions. Graphene is a two-dimensional sheet of carbons atoms, an allotrope of carbon like graphite, its 3D counterpart. Graphene and composites assembled with graphene have displayed remarkable mechanical strength, strong light-matter interactions, and promising conductivities.[8–23] Further research into graphene produced a number of exciting advancements in devices for many applications including photodetectors, transistors, sensors, and catalysts. The atom thick nature of the two-dimensional

sheet confers these remarkable properties due to many factors including reduced dielectric screening and strong columbic attraction between excitonic species.

Since the discovery of graphene, many different chemical compositions have been explored in two-dimensional variants. Other prominent 2D materials include hexagonal boron nitride (h-BN), silicene, phosphorene, transition metal dichalcogenides, MOFs and perovskites. h-BN is an extension of graphene as it is isoelectronic with graphene. However, h-BN is planar whereas graphene has a buckled sheet geometry and the optical properties of h-BN differ dramatically from its graphene cousin.[24–28] For example, the band gap in h-BN is finite at low layer numbers and tunable. Silicene is the silicon analogue of graphene, creating a two-dimensional sheet of Si atoms, however, it possess significantly different band structure characteristics than graphene (Fig. 1.1 (a)).[29–39]

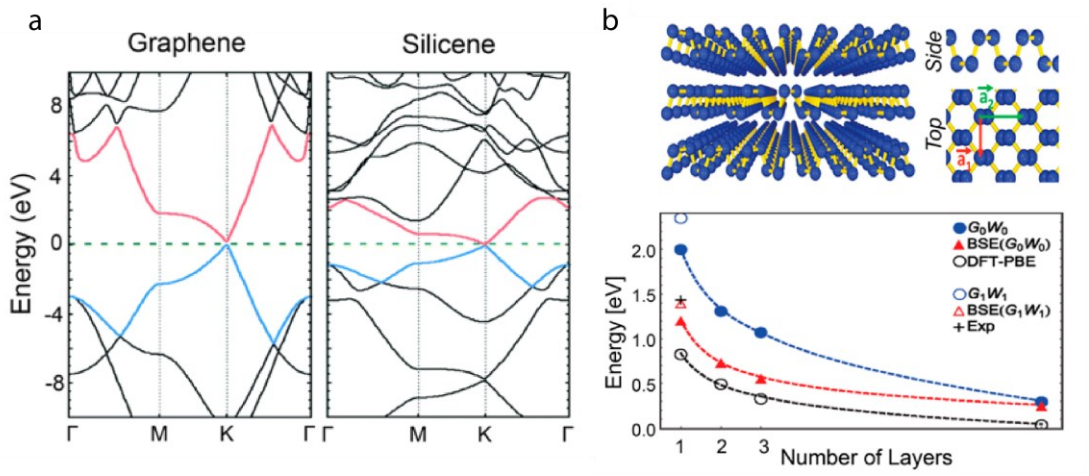

Figure 1.1. (a) Band structures for graphene and silicene with conduction band and valence band highlights red and blue, respectively.[38] (b) Cartoon of phosphorene with enhanced side and part views showing phosphorene's structure (top).[40] Experimental and theoretical data for the band gap energy of phosphorene as a function of the number of layers (bottom).[39]

Phosphorene is the P containing analogue to graphene and physical characteristics such as edge termination differs greatly from graphene (Fig. 1.1 (b).[40–44] Organic and hybrid organic materials such as covalent organic frameworks, metal organic frameworks and inorganic and hybrid perovskites all have exhibited unique 2D morphologically-derived properties as well.[45–54] These systems differ for not being on the order of an atom thick slab as graphene and its cousins, instead comprised of inorganic cluster building units instead of single atoms. These materials are extremely modular, meaning different building blocks can be substituted for a wide range of different functional capabilities. However, acquiring 2D versions of these molecular structure materials can be a great

challenge, and are often utilized as thin films (< 100 nm) rather than true 2D few atom thick materials such as graphene.

1.2 Transition Metal Dichalcogenides

Perhaps the most promising of the post-graphene 2D materials are the transition metal dichalcogenides. Transition metal dichalcogenides are composed of a transition metal and a member of the chalcogen family. Common TMDs are of the Mo family namely, MoS_2, $MoSe_2$, WS_2, and WSe_2. Though these materials are similar to graphene in that they are comprised of individual layers held together by weak van der Waals forces in the vertical direction, there is no single component chemical specificity given to TMDs like graphene, silicene, and phosphorene. TMDs can compromise a wide range of elements, mainly including Mo, W, S, Se, and Te. We also see that TMDs exhibit a wide range of phenomena that compliment but deviate significantly from other 2D materials like graphene.

It is important to understand the variety of synthetic tools available for creating and modulating 2D materials because they all possess advantages and disadvantages towards specific material outcomes and inform experimental design. The first synthetic technique used to assemble 2D materials was the "Scotch tape method" developed at the initial discovery of graphene.[55–57] This method involves using tape to mechanically exfoliate a bulk sample (in the

original case, graphene) and removes mono- and few- layer graphene moieties. This mechanical exfoliation is extremely practical and easy to administer. However, the resulting 2D materials are not of the highest quality and the dispersion in layer number between different exfoliation attempts is large, though defect engineering through exfoliation techniques present new opportunities.[57–62] Another early method of 2D material production was chemical exfoliation. In this method, the weak van der Waals forces holding the layers in the bulk material together in the vertical direction are broken apart by the intercalation of chemical species.[63–67] This creates 2D materials in a similar way to mechanical exfoliation, by disrupting the weak interlayer forces in a bulk crystal. The resulting materials for chemical exfoliation generally are of higher quality than mechanical exfoliation, however, their dispersity in layer thickness is not improved over mechanical exfoliation. It is notable that solution processing can afford new properties such as phase changes, capacitance, and catalytic capabilities that are different than those obtained via mechanical exfoliation.[68–71]

When scientists discovered the utility of 2D materials, synthetic methods were quickly developed that sought to assemble 2D materials from constituent pieces rather than exfoliation from bulk material. To this end, chemical vapor deposition (CVD) has been greatly utilized in the formation of 2D materials. In this method, solid phase precursors are volatilized in the gas phase to react to

form new species which deposit on a substrate and propagate to form 2D materials.[72–75] Several factors can be tuned to alter the layer number, size, and dispersity of the resulting materials. The level of control exhibited by this gas phase method is many orders of magnitude higher than in exfoliation methods and the resulting materials generated are of generally very high quality. Other gas phase methods to produce 2D materials include atomic layer deposition (ALD), metal-organic chemical vapor deposition (MOCVD), and molecular beam epitaxy (MBE).[76–89] ALD focuses on synthesizing layered materials by utilizing sequential gas phase precursors to deposit material on a substrate. There are many different forms of ALD including thermal, plasma, photo-assisted and catalytic methods.[80,81,83] ALD creates well-defined material domains over large substrate areas and is conducive to large scale industrial use. However, unlike CVD processes it is extremely costly in both resources and time. Alternatively, MOCVD utilizes the same principles of CVD in that it is a scalable, relatively inexpensive process. MOCVD can produce high quality materials with the wide range of metal organic precursors available and is an extremely versatile method. However, the same metal-organic precursors that enable a wide range of material outcomes also can be extremely toxic to the environment raising questions about its long-term viability for high-throughput material synthesis. Finally, MBE is another gas phase method that creates2D materials through

effusion of various precursors to produce explicit epitaxial growth for pure monolayer or hetero-layer materials. This method achieves the highest quality materials but is slow and requires a large instrumentation investment.

Though many 2D materials exist and are active subjects or research, transition metal dichalcogenides offer several intriguing properties that are useful in basic research and technological application. TMD materials are composed of layers held together in the vertical direction by van der Waals forces with metal and chalcogen atoms covalently bonded laterally (Fig. 1.2). These crystals can be structured in different ways, with many TMDs exhibiting a lower energy semiconducting '2H' phase where each layer of TMD composed of 6 chalcogen atoms making a trigonal prism around a metal atom.[90,91]

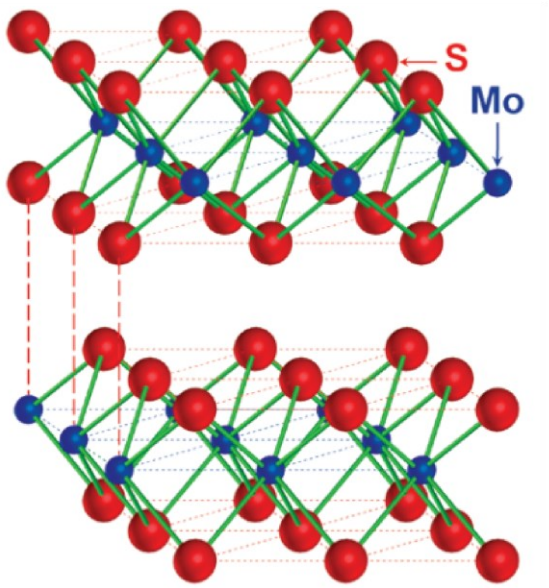

Figure 1.2. Ball and stick model of MoS_2 where red and blue balls represent S and Mo atoms respectively. The structure is depicted as a 2H trigonal prism phase with a finite layer separation held together by van der Waals forces.[90]

When the crystal structure of the TMD is distorted from its trigonal prismatic geometry, a 1T octahedral phase can be created, which is metallic. This metallic phase has found utility in several applications such as catalysis and optical phenomena.[92–95] Finally, a less common 3R rhombohedral phase is possible through non-conventional synthetic means, where a rhombohedron of chalcogen atoms is formed around a central metal atom.[96–100] For all these structures, the unit cells repeat laterally but there is a finite distanced van der Waals gap that exists between layers, held together by weak van der Waals

forces. The exploitation of these weak forces allows for the creation of low-dimensional materials with great ease as discussed previously with exfoliation and direct synthesis methods.

While graphene is a semimetal absent a bandgap at the K symmetry point without external perturbation, transition metal dichalcogenides do have a bandgap in the monolayer limit. In MoS_2, the electronic structure can be modulated where, the bandgap undergoes a shift from indirect to direct when the layer number approaches the monolayer limit. Band diagrams show a shift from indirect (bulk) and direct (monolayer) bandgaps respectively for MoS_2 (Fig. 1.3). [101–103]

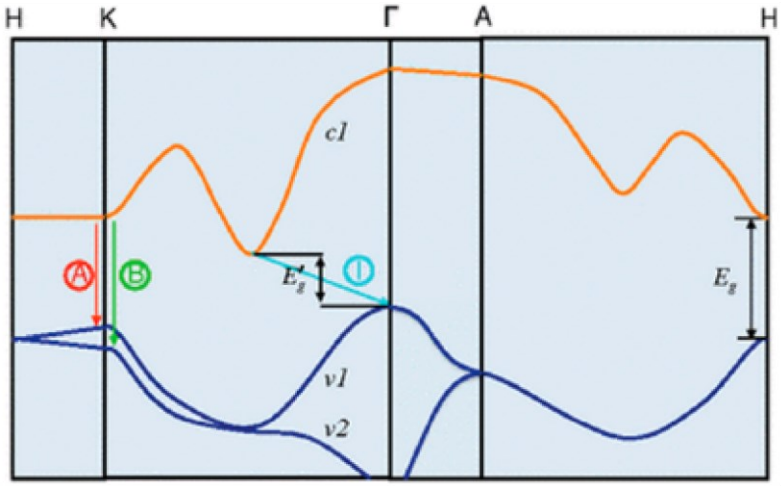

Figure 1.3. Band diagram for MoS_2. The indirect transition at the (R) point is highlighted in blue. Direct band gap transitions are highlighted in red and green for the A and B transitions respectively.[101]

This direct bandgap has multiple transitions including a primary A exciton and a B exciton at approximately 150 meV greater energy.[104–106] TMDs exhibit several intense characteristic peaks in low wavenumber regions that provide ready identification of material and layer number as discussed in several reports via Raman scattering measurements.[107–114]

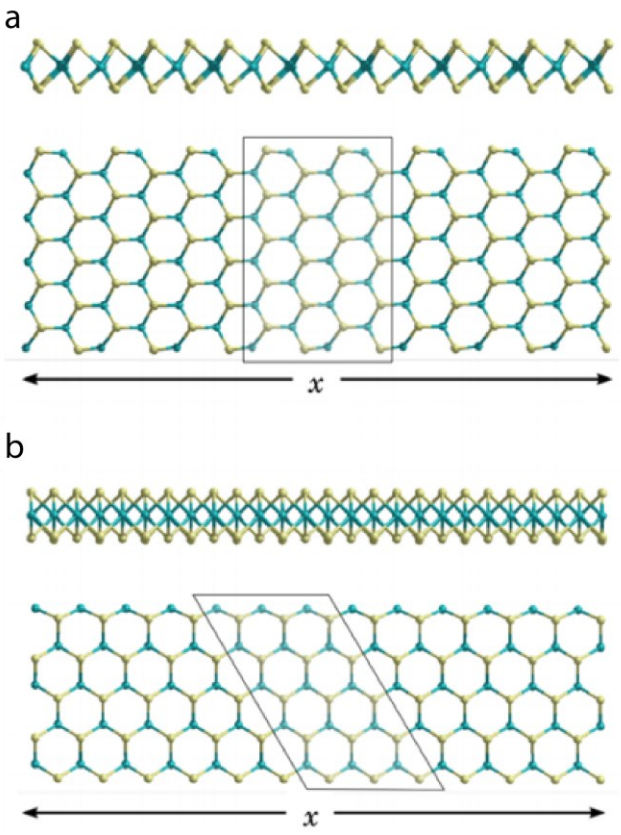

Figure 1.4. Model of MoS_2 nanoribbon geometries with side and top views for both the armchair (a) and zigzag (b) configuration of nanoribbons.[115] Blue and yellow spheres represent Mo and S atoms respectively.

In low-dimensional TMDs, the edge structure influences properties of TMDs dramatically as the edges compose a large percentage of the exposed atoms. The edges are also exposed and unsaturated which often allows for functionalization or other modulation in many low dimensional materials. For low-dimensional TMDs, edges can configure in either armchair or zigzag fashion

(Fig. 1.4).[115–119] These edges can impart catalytic, electronic, optical and magnetic properties to low-dimensional TMDs. Further, edges of TMDs are even more important in one-dimensional TMDs such as nanoribbons due to their greater edge to basal plane ratio.[120–123]

A key advantage of crystals of low-dimensional materials which have layers held together by weak inter-layer forces is vertically stacking heterostructures of different materials. This advantage is not conferred on covalently bonded heterostructures and is possibly the most attractive feature of van der Waals low dimensional materials. Assembly of low dimensional materials into vertical heterostructures has greatly expanded the library of effective properties available to researchers.[124–131] Many alloyed and heterostructured non-2D materials have incredible difficulty effectively integrating materials in a truly mixed system which does not phase separate in a manner that impacts material performance.[132,133] For example, patterning vertical heterostructure through external probes, such as lasers, can allow for the scalable and general creation of van der Waals vertically stacked heterostructures (Fig 1.5).[127,134] Vertical heterostructures have seen uses in catalysis, memory, and next generation computing.[1,135–138] Additionally, the relative rotation of vertically stacked layers can influence properties as discussed later in this chapter.

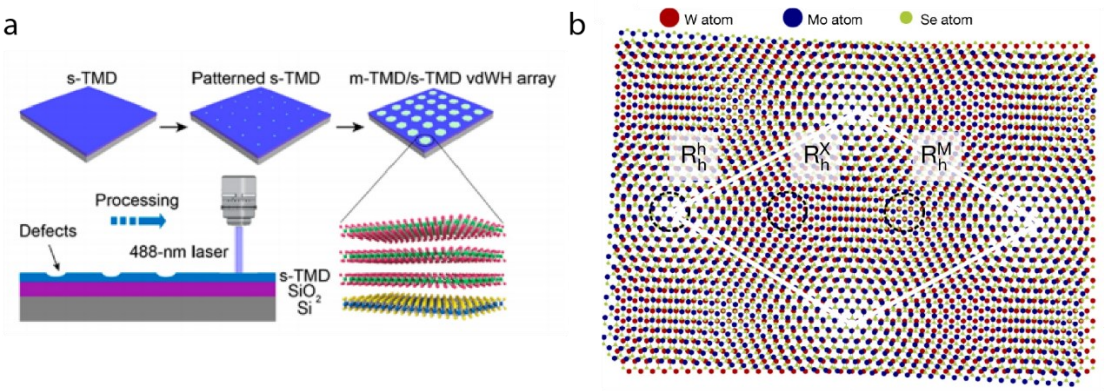

Figure 1.5. (a) Schematic illustrating the process of fabricating metallic-semiconducting TMD heterostructures. Laser induced local defects are seeded with a secondary TMD to create a heterostructure system.[134] (b) Illustration of a vertical heterostructure of $MoSe_2/WSe_2$ with slightly misaligned layers creating Moire interference patterns that regain three fold symmetry at certain points in the superstructure denoted by R^y.[127]

Lateral heterostructures, complementing vertical heterostructures, have also been constructed with TMDs and other 2D materials. In these heterostructures new functionality is imparted primarily in the interfacial region between the heterostructures as has been noted with one-dimensional contact regions with other materials such as graphene. In recent years exceptional control has been generated over lateral heterostructures (Fig. 1.6). Progress has been made in creating edge boundary regions of a different TMD and recent research has demonstrated the ability to systematically engineer multiple interfacial regions within a single domain of a TMD crystal.[139–142]

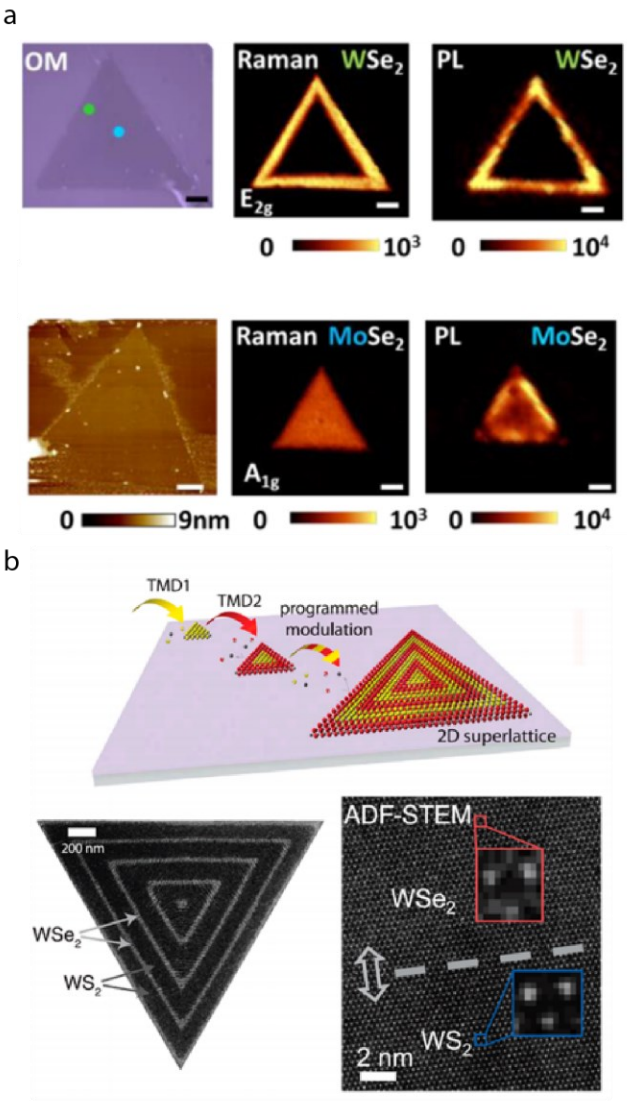

Figure 1.6. (a) Optimal microscopy, atomic force microscopy, and photoluminescence and Raman mapping of a $MoSe_2/WSe_2$ lateral heterostructure. The data demonstrates a core of $MoSe_2$ with a edge region dominated by WSe_2. Scale bars, 5 μm.[141] (b) Schematic illustrating the process for constructing repeating lateral heterostructures in TMDs that can create a lateral 2D superlattice. Electron micrograph image of a lateral heterostructure composed of WSe_2/WS_2 that repeats over several units. STEM image with insets show a clear and sharp interface between the two constituent TMD materials.[142]

Control over the dimensionality of low-dimensionality materials at will is paramount in unlocking new phenomena in a multitude of materials. Single component low-dimensional TMDs have seen uses in applications such as transistors, photodetectors, catalysis, single photon emission, spintronics, valleytronics, memristors and more. Here, we will provide a brief overview of why transition metal dichalcogenides are promising materials for these applications.

First, transistor properties are superlative due to their high on/off ratios and superior particle mobilities.[143–146] Photoresponsivity in low dimensional TMDs has proven to be more than adequate to compete with other prominent low-dimensional materials such as graphene.[147–149] Edge properties dominate several applications such as catalysis as catalytic activity is focused at exposed edge sites, particularly for the useful hydrogen evolution reaction (HER).[1,3,150] Further, the basal planes of the TMDs can be activated for catalysis through electrical means.[151] Atomic defects in low-dimensional TMDs have been exploited for their utility as single photon emitters.[152–154] Next generation computing utilizing spins, valleys, and neuromorphic strategies all take advantage of the variety and complexity of edges, phases, and compositions that can manifest in low dimensional TMDs.[138,155–159] Methods such as scanning probes

have been demonstrated as a method for deterministically placing defects in 2D materials and probing localized emission (Fig. 1.7).[160,161]

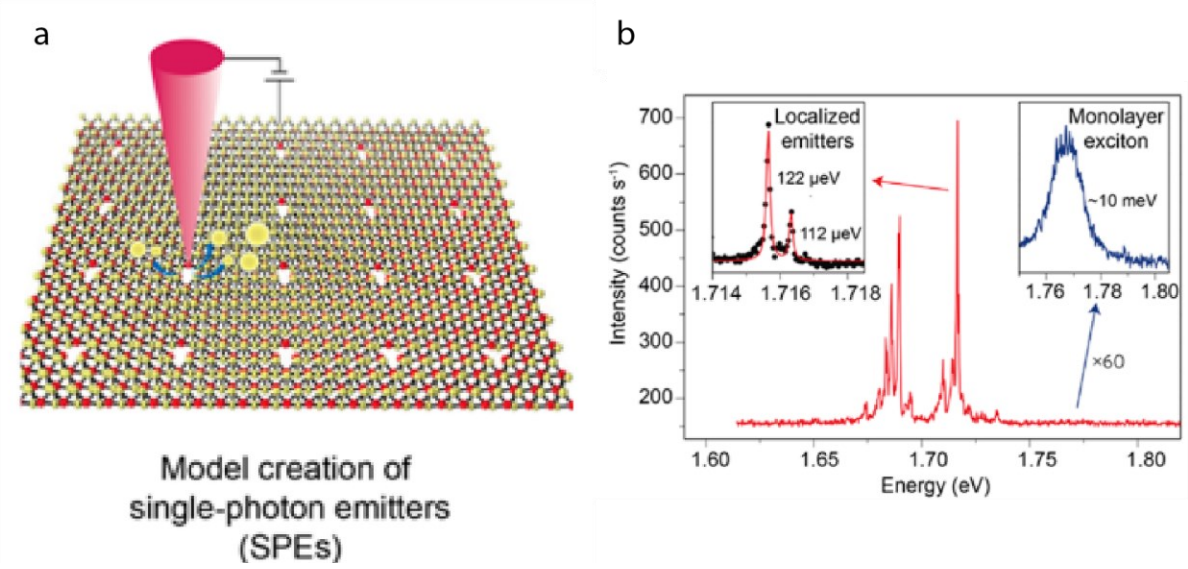

Figure 1.7. (a) Schematic illustrating creating well-defined defects through scanning probe lithography for use in single-photon emitters.[161] (b) Single quantum emitter behavior in a single layer of WSe_2 as demonstrated by very sharp spectral features with very little peak broadening.[160]

Though single component systems are extremely useful for many applications, much of the current research has centered around heterostructures with multi-component TMDs or interfacing TMD monolayers with monolayers of other materials, such as graphene or h-BN. These heterostructures open up more flexibility and increase effectiveness in many of the applications mentioned previously as discussed in several reviews. Emergent phenomena in van der Waals heterostructures open up the possibility of utilizing relative rotation of

individual layers to achieve intriguing physical phenomena such as Moire interference patterns as seen in Fig 1.5.[127,162–165] These Moire interference patterns exert unique control over excitonic properties in two-dimensional materials and have even been shown to exhibit superconductivity in magic angle graphene.[166–171]

1.3 Overview of Other Dimensionalities

Though 2D materials present an interesting platform on which to examine rich chemistry and physics, nanocrystals encompassing 0D and 1D are equally promising. 0D TMDs have been synthesized using laser ablation techniques and mechanical sonication.[93,172,173] Due to their intrinsic 0D nature they offer advantages in catalysis, charge transfer, and quantum optics.[160,174–182] 0D TMDs will not be a focus of this work but present an intriguing platform for further research.

1D TMDs will be discussed more in a future chapter, but these moieties are a rapidly evolving material class of materials. Though graphene nanoribbons and carbon nanotubes have dominated 1D materials, recent advances in high quality, scalable TMD synthesis affords the opportunity to utilize 1D TMDs as a platform next generation technologies.[183]

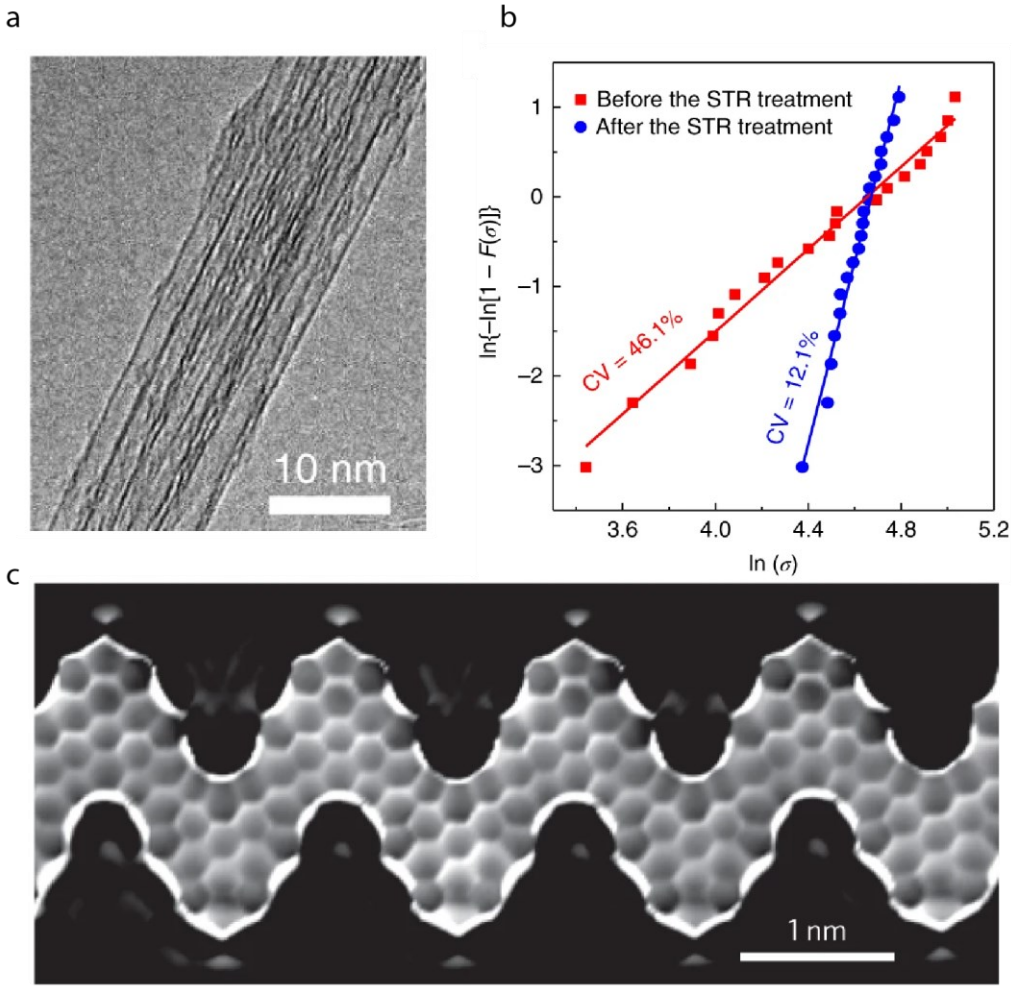

Figure 1.8. (a) Transmission electron micrograph of a carbon nanotube bundle that was tested in (b) for its tensile strength before and after treatment with synchronous tightening and relaxing (STR) strategies.[184] (c) Bond-resolved scanning tunnel microscopy (BRSTM) micrograph showing functionalized graphene nanoribbon moieties and their well-defined heterojunctions.[185]

In addition to two-dimensional graphene, other morphologies utilizing carbon, such as one-dimensional carbon nanotubes (CNTs) and graphene nanoribbons (GNRs), have been investigated. Both of these 1D materials possess unique properties from the other dimensionally reduced allotropes (graphene)

such as metallicity, chirality, and incredibly high tensile strength in CNTs, while exotic edge phenomena, precise heterojunction control, and optical anisotropy are hallmarks of GNRs[122,185–195]. Carbon-based 1D systems present a number of attractive features, including tensile strength and modularity based on functional group placement (Fig 1.8).[184,185,196,197] In addition, carbon based 0D quantum dots have garnered some interest to which their confinement in all three dimensions exerts different control on its behavior compared to 2D and 1D varieties. nevertheless, the number of reports devoted to discussion of 0D materials is relatively few compared to their 2D and 1D counterparts.

Analogues to graphene, two-dimensional transition metal dichalcogenide materials also present in one dimensional varieties including nanotubes and planar nanoribbons. These 1D materials have unique attributes that make them attractive candidates for catalysis, opto-electronics, and next generation computing. However, to date this area of research has been neglected. One-dimensional TMD nanoribbons will be the focus of chapters 3 through 5.

To date, much of the research into transition metal dichalcogenides and other two-dimensional materials has centered around the investigation of physical properties. However, researchers have not critically examined the role of morphology in these systems. That is, less focus has been generated on manipulating low-dimensional materials beyond two dimensional for desired

properties until recently. The goal of this work is to further understand how external factors beyond the material, i.e. surfaces, reaction conditions, etc. influence material properties. Particularly, this work focuses on three pillars. First, understanding how canonical surfaces, such as SiO_2, and reaction conditions can cause deviation from the normal outcomes in intermediate formation of TMDs. Second, we discuss a novel synthetic method of creating prescribed substrates for particular substrate-crystal interactions to create directed growth in a nanoribbon morphology. Lastly, we study the evolution of morphology-property relationships in decreasing dimensionality from two dimensions down to one. The combination of these three thrusts centers on the idea that we should be critically examining overlooked growth parameters, such as intermediate formation and substrate choice. The modulation of these parameterswill yield new and useful information about TMD synthesis which will allow us to impart new levels of control on TMD materials.

The chapters following will explore efforts used to understand how reaction conditions influence growth of transition metal dichalcogenides. Results herein demonstrate novel strategies to gain mechanistic insights into the chalcogen incorporation towards TMD growth by utilizing an unusual two-step synthesis. This method can aid in both understanding low-dimensional TMD synthesis and unlocking milder conditions than traditionally used in TMD

synthesis, that may allow synthesis of vertical heterostructures or integration with less robust materials. The main thrust of this thesis discusses a novel synthetic strategy developed by our group that greatly expands the ability to controllably synthesize one dimensional TMD nanoribbons. We have demonstrated the ability to grow multiple compositions of TMDs utilizing this method and have shown two distinct methods of significantly controlling the morphology of the resulting materials. This new method underscores exciting opportunities in the growth of transition metal dichalcogenides beyond that of two dimensions.

1.4 References

(1) Deng, D.; Novoselov, K. S.; Fu, Q.; Zheng, N.; Tian, Z.; Bao, X. Catalysis with Two-Dimensional Materials and Their Heterostructures. *Nat. Nanotechnol.* **2016**, *11* (3), 218–230.

(2) Liu, X.; Guo, Q.; Qiu, J. Emerging Low-Dimensional Materials for Nonlinear Optics and Ultrafast Photonics. *Adv. Mater.* **2017**, *29* (14), 1605886.

(3) Voiry, D.; Shin, H. S.; Loh, K. P.; Chhowalla, M. Low-Dimensional Catalysts for Hydrogen Evolution and CO_2 Reduction. *Nat. Rev. Chem.* **2018**, *2* (1), 1–17.

(4) Wu, W. Inorganic Nanomaterials for Printed Electronics: A Review. *Nanoscale* **2017**, *9* (22), 7342–7372.

(5) Gu, M.; Zhang, Q.; Lamon, S. Nanomaterials for Optical Data Storage. *Nat. Rev. Mater.* **2016**, *1* (12), 1–14.

(6) Holzinger, M.; Le Goff, A.; Cosnier, S. Nanomaterials for Biosensing Applications: A Review. *Front. Chem.* **2014**, *2*.

(7) Novoselov, K. S.; Geim, A. K.; Morozov, S. V.; Jiang, D.; Zhang, Y.; Dubonos, S. V.; Grigorieva, I. V.; Firsov, A. A. Electric Field Effect in Atomically Thin Carbon Films. *Science* **2004**, *306* (5696), 666–669.

(8) Geim, A. K.; Novoselov, K. S. The Rise of Graphene. *Nat, Mater.* **2007**, *6* (3), 183–191.

(9) Engel, M.; Steiner, M.; Lombardo, A.; Ferrari, A. C.; Löhneysen, H. v; Avouris, P.; Krupke, R. Light–Matter Interaction in a Microcavity-Controlled Graphene Transistor. *Nat. Commun.* **2012**, *3* (1), 906.

(10) Gan, X.; Mak, K. F.; Gao, Y.; You, Y.; Hatami, F.; Hone, J.; Heinz, T. F.; Englund, D. Strong Enhancement of Light–Matter Interaction in Graphene Coupled to a Photonic Crystal Nanocavity. *Nano Lett.* **2012**, *12* (11), 5626–5631.

(11) Koppens, F. H. L.; Chang, D. E.; García de Abajo, F. J. Graphene Plasmonics: A Platform for Strong Light–Matter Interactions. *Nano Lett.* **2011**, *11* (8), 3370–3377.

(12) Frank, I. W.; Tanenbaum, D. M.; van der Zande, A. M.; McEuen, P. L. Mechanical Properties of Suspended Graphene Sheets. *Journal of Vacuum Science & Technology B: Microelectronics and Nanometer Structures Processing, Measurement, and Phenomena* **2007**, *25* (6), 2558–2561.

(13) Tang, L.-C.; Wan, Y.-J.; Yan, D.; Pei, Y.-B.; Zhao, L.; Li, Y.-B.; Wu, L.-B.; Jiang, J.-X.; Lai, G.-Q. The Effect of Graphene Dispersion on the Mechanical Properties of Graphene/Epoxy Composites. *Carbon* **2013**, *60*, 16–27.

(14) Suk, J. W.; Piner, R. D.; An, J.; Ruoff, R. S. Mechanical Properties of Monolayer Graphene Oxide. *ACS Nano* **2010**, *4* (11), 6557–6564.

(15) Rafiee, M. A.; Rafiee, J.; Wang, Z.; Song, H.; Yu, Z.-Z.; Koratkar, N. Enhanced Mechanical Properties of Nanocomposites at Low Graphene Content. *ACS Nano* **2009**, *3* (12), 3884–3890.

(16) Falkovsky, L. A.; Varlamov, A. A. Space-Time Dispersion of Graphene Conductivity. *Eur. Phys. J. B* **2007**, *56* (4), 281–284.

(17) Mak, K. F.; Sfeir, M. Y.; Wu, Y.; Lui, C. H.; Misewich, J. A.; Heinz, T. F. Measurement of the Optical Conductivity of Graphene. *Phys. Rev. Lett.* **2008**, *101* (19), 196405.
(18) Balandin, A. A.; Ghosh, S.; Bao, W.; Calizo, I.; Teweldebrhan, D.; Miao, F.; Lau, C. N. Superior Thermal Conductivity of Single-Layer Graphene. *Nano Lett.* **2008**, *8* (3), 902–907.
(19) Tan, Y.-W.; Zhang, Y.; Bolotin, K.; Zhao, Y.; Adam, S.; Hwang, E. H.; Das Sarma, S.; Stormer, H. L.; Kim, P. Measurement of Scattering Rate and Minimum Conductivity in Graphene. *Phys. Rev. Lett.* **2007**, *99* (24), 246803.
(20) Gusynin, V. P.; Sharapov, S. G.; Carbotte, J. P. Magneto-Optical Conductivity in Graphene. *J. Phys.: Condens. Matter* **2006**, *19* (2), 026222.
(21) Chen, S.; Wu, Q.; Mishra, C.; Kang, J.; Zhang, H.; Cho, K.; Cai, W.; Balandin, A. A.; Ruoff, R. S. Thermal Conductivity of Isotopically Modified Graphene. *Nature Materials* **2012**, *11* (3), 203–207.
(22) Worsley, M. A.; Pauzauskie, P. J.; Olson, T. Y.; Biener, J.; Satcher, J. H.; Baumann, T. F. Synthesis of Graphene Aerogel with High Electrical Conductivity. *J. Am. Chem. Soc.* **2010**, *132* (40), 14067–14069.
(23) Jung, I.; Dikin, D. A.; Piner, R. D.; Ruoff, R. S. Tunable Electrical Conductivity of Individual Graphene Oxide Sheets Reduced at "Low" Temperatures. *Nano Lett.* **2008**, *8* (12), 4283–4287.
(24) Liu, L.; Feng, Y. P.; Shen, Z. X. Structural and Electronic Properties of H-BN. *Phys. Rev. B* **2003**, *68* (10), 104102.
(25) Li, Y.; Rao, Y.; Mak, K. F.; You, Y.; Wang, S.; Dean, C. R.; Heinz, T. F. Probing Symmetry Properties of Few-Layer MoS 2 and h-BN by Optical Second-Harmonic Generation. *Nano Lett.* **2013**, *13* (7), 3329–3333.
(26) Wang, S.; Wang, X.; Warner, J. H. All Chemical Vapor Deposition Growth of MoS2:H-BN Vertical van Der Waals Heterostructures. *ACS Nano* **2015**, *9* (5), 5246–5254.
(27) Behera, H.; Mukhopadhyay, G. Strain-Tunable Band Gap in Graphene/h-BN Hetero-Bilayer. *Journal of Physics and Chemistry of Solids* **2012**, *73* (7), 818–821.
(28) Radhakrishnan, S.; Das, D.; Samanta, A.; Reyes, C. A. de los; Deng, L.; Alemany, L. B.; Weldeghiorghis, T. K.; Khabashesku, V. N.; Kochat, V.; Jin, Z.; Sudeep, P. M.; Martí, A. A.; Chu, C.-W.; Roy, A.; Tiwary, C. S.; Singh, A. K.; Ajayan, P. M. Fluorinated H-BN as a Magnetic Semiconductor. *Sci. Adv.* **2017**, *3* (7), e1700842.
(29) Kara, A.; Enriquez, H.; Seitsonen, A. P.; Lew Yan Voon, L. C.; Vizzini, S.; Aufray, B.; Oughaddou, H. A Review on Silicene — New Candidate for Electronics. *Surf. Sci. Rep.* **2012**, *67* (1), 1–18.
(30) Houssa, M.; Dimoulas, A.; Molle, A. Silicene: A Review of Recent Experimental and Theoretical Investigations. *J. Phys.: Condens. Matter* **2015**, *27* (25), 253002.
(31) Chowdhury, S.; Jana, D. A Theoretical Review on Electronic, Magnetic and Optical Properties of Silicene. *Rep. Prog. Phys.* **2016**, *79* (12), 126501.
(32) Drummond, N. D.; Zólyomi, V.; Fal'ko, V. I. Electrically Tunable Band Gap in Silicene. *Phys. Rev. B* **2012**, *85* (7), 075423.

(33) Vogt, P.; De Padova, P.; Quaresima, C.; Avila, J.; Frantzeskakis, E.; Asensio, M. C.; Resta, A.; Ealet, B.; Le Lay, G. Silicene: Compelling Experimental Evidence for Graphenelike Two-Dimensional Silicon. *Phys. Rev. Lett.* **2012**, *108* (15), 155501.
(34) Kara, A.; Enriquez, H.; Seitsonen, A. P.; Lew Yan Voon, L. C.; Vizzini, S.; Aufray, B.; Oughaddou, H. A Review on Silicene — New Candidate for Electronics. *Surf. Sci. Rep.* **2012**, *67* (1), 1–18.
(35) Lin, C.-L.; Arafune, R.; Kawahara, K.; Tsukahara, N.; Minamitani, E.; Kim, Y.; Takagi, N.; Kawai, M. Structure of Silicene Grown on Ag(111). *Appl. Phys. Express* **2012**, *5* (4), 045802.
(36) Lalmi, B.; Oughaddou, H.; Enriquez, H.; Kara, A.; Vizzini, S.; Ealet, B.; Aufray, B. Epitaxial Growth of a Silicene Sheet. *Appl. Phys. Lett.* **2010**, *97* (22), 223109.
(37) Zhao, J.; Liu, H.; Yu, Z.; Quhe, R.; Zhou, S.; Wang, Y.; Liu, C. C.; Zhong, H.; Han, N.; Lu, J.; Yao, Y.; Wu, K. Rise of Silicene: A Competitive 2D Material. *Prog. in Mater. Sci.* **2016**, *83*, 24–151.
(38) Miró, P.; Audiffred, M.; Heine, T. An Atlas of Two-Dimensional Materials. *Chem. Soc. Rev.* **2014**, *43* (18), 6537–6554.
(39) Tran, V.; Soklaski, R.; Liang, Y.; Yang, L. Layer-Controlled Band Gap and Anisotropic Excitons in Few-Layer Black Phosphorus. *Phys. Rev. B* **2014**, *89* (23), 235319.
(40) Liu, H.; Neal, A. T.; Zhu, Z.; Luo, Z.; Xu, X.; Tománek, D.; Ye, P. D. Phosphorene: An Unexplored 2D Semiconductor with a High Hole Mobility. *ACS Nano* **2014**, *8* (4), 4033–4041.
(41) Carvalho, A.; Wang, M.; Zhu, X.; Rodin, A. S.; Su, H.; Castro Neto, A. H. Phosphorene: From Theory to Applications. *Nat. Rev. Mater.* **2016**, *1* (11), 1–16.
(42) Das, S.; Zhang, W.; Demarteau, M.; Hoffmann, A.; Dubey, M.; Roelofs, A. Tunable Transport Gap in Phosphorene. *Nano Lett.* **2014**, *14* (10), 5733–5739.
(43) Kou, L.; Chen, C.; Smith, S. C. Phosphorene: Fabrication, Properties, and Applications. *J. Phys. Chem. Lett.* **2015**, *6* (14), 2794–2805.
(44) Batmunkh, M.; Bat-Erdene, M.; Shapter, J. G. Phosphorene and Phosphorene-Based Materials – Prospects for Future Applications. *Adv. Mater.* **2016**, *28* (39), 8586–8617.
(45) Milot, R. L.; Sutton, R. J.; Eperon, G. E.; Haghighirad, A. A.; Martinez Hardigree, J.; Miranda, L.; Snaith, H. J.; Johnston, M. B.; Herz, L. M. Charge-Carrier Dynamics in 2D Hybrid Metal–Halide Perovskites. *Nano Lett.* **2016**, *16* (11), 7001–7007.
(46) Dou, L.; Wong, A. B.; Yu, Y.; Lai, M.; Kornienko, N.; Eaton, S. W.; Fu, A.; Bischak, C. G.; Ma, J.; Ding, T.; Ginsberg, N. S.; Wang, L.-W.; Alivisatos, A. P.; Yang, P. Atomically Thin Two-Dimensional Organic-Inorganic Hybrid Perovskites. *Science* **2015**, *349* (6255), 1518–1521.
(47) Campbell, M. G.; Liu, S. F.; Swager, T. M.; Dincă, M. Chemiresistive Sensor Arrays from Conductive 2D Metal–Organic Frameworks. *J. Am. Chem. Soc.* **2015**, *137* (43), 13780–13783.
(48) Campbell, M. G.; Sheberla, D.; Liu, S. F.; Swager, T. M.; Dincă, M. Cu_3(Hexaiminotriphenylene)$_2$: An Electrically Conductive 2D Metal–Organic

Framework for Chemiresistive Sensing. *Angewandte Chemie International Edition* **2015**, *54* (14), 4349–4352.
(49) Zhu, H.; Liu, D. The Synthetic Strategies of Metal–Organic Framework Membranes, Films and 2D MOFs and Their Applications in Devices. *J. Mater. Chem. A* **2019**, *7* (37), 21004–21035.
(50) Rui, K.; Zhao, G.; Chen, Y.; Lin, Y.; Zhou, Q.; Chen, J.; Zhu, J.; Sun, W.; Huang, W.; Dou, S. X. Hybrid 2D Dual-Metal–Organic Frameworks for Enhanced Water Oxidation Catalysis. *Adv. Funct. Mater.* **2018**, *28* (26), 1801554.
(51) Zhan, X.; Chen, Z.; Zhang, Q. Recent Progress in Two-Dimensional COFs for Energy-Related Applications. *J. Mater. Chem. A* **2017**, *5* (28), 14463–14479.
(52) Ding, S.-Y.; Wang, W. Covalent Organic Frameworks (COFs): From Design to Applications. *Chem. Soc. Rev.* **2012**, *42* (2), 548–568.
(53) Niu, G.; Guo, X.; Wang, L. Review of Recent Progress in Chemical Stability of Perovskite Solar Cells. *J. Mater. Chem. A* **2015**, *3* (17), 8970–8980.
(54) Zhao, M.; Wang, Y.; Ma, Q.; Huang, Y.; Zhang, X.; Ping, J.; Zhang, Z.; Lu, Q.; Yu, Y.; Xu, H.; Zhao, Y.; Zhang, H. Ultrathin 2D Metal–Organic Framework Nanosheets. *Advanced Materials* **2015**, *27* (45), 7372–7378.
(55) Kanazawa, T.; Amemiya, T.; Ishikawa, A.; Upadhyaya, V.; Tsuruta, K.; Tanaka, T.; Miyamoto, Y. Few-Layer HfS_2 Transistors. *Sci. Rep.* **2016**, *6* (1), 22277.
(56) Zhang, H.; Chhowalla, M.; Liu, Z. 2D Nanomaterials: Graphene and Transition Metal Dichalcogenides. *Chem. Soc. Rev.* **2018**, *47* (9), 3015–3017.
(57) Li, H.; Lu, G.; Wang, Y.; Yin, Z.; Cong, C.; He, Q.; Wang, L.; Ding, F.; Yu, T.; Zhang, H. Mechanical Exfoliation and Characterization of Single- and Few-Layer Nanosheets of WSe_2, TaS_2, and $TaSe_2$. *Small* **2013**, *9* (11), 1974–1981.
(58) Coleman, J. N.; Lotya, M.; O'Neill, A.; Bergin, S. D.; King, P. J.; Khan, U.; Young, K.; Gaucher, A.; De, S.; Smith, R. J.; Shvets, I. V.; Arora, S. K.; Stanton, G.; Kim, H.-Y.; Lee, K.; Kim, G. T.; Duesberg, G. S.; Hallam, T.; Boland, J. J.; Wang, J. J.; Donegan, J. F.; Grunlan, J. C.; Moriarty, G.; Shmeliov, A.; Nicholls, R. J.; Perkins, J. M.; Grieveson, E. M.; Theuwissen, K.; McComb, D. W.; Nellist, P. D.; Nicolosi, V. Two-Dimensional Nanosheets Produced by Liquid Exfoliation of Layered Materials. *Science* **2011**, *331* (6017), 568–571.
(59) Lin, Z.; Carvalho, B. R.; Kahn, E.; Lv, R.; Rao, R.; Terrones, H.; Pimenta, M. A.; Terrones, M. Defect Engineering of Two-Dimensional Transition Metal Dichalcogenides. *2D Mater.* **2016**, *3* (2), 022002.
(60) Chow, P. K.; Jacobs-Gedrim, R. B.; Gao, J.; Lu, T.-M.; Yu, B.; Terrones, H.; Koratkar, N. Defect-Induced Photoluminescence in Monolayer Semiconducting Transition Metal Dichalcogenides. *ACS Nano* **2015**, *9* (2), 1520–1527.
(61) Li, H.; Wu, J.; Yin, Z.; Zhang, H. Preparation and Applications of Mechanically Exfoliated Single-Layer and Multilayer MoS_2 and WSe_2 Nanosheets. *Acc. Chem. Res.* **2014**, *47* (4), 1067–1075.
(62) Ottaviano, L.; Palleschi, S.; Perrozzi, F.; D'Olimpio, G.; Priante, F.; Donarelli, M.; Benassi, P.; Nardone, M.; Gonchigsuren, M.; Gombosuren, M.; Lucia, A.; Moccia, G.;

Cacioppo, O. A. Mechanical Exfoliation and Layer Number Identification of MoS_2 Revisited. *2D Mater.* **2017**, *4* (4), 045013.
(63) Smith, R. J.; King, P. J.; Lotya, M.; Wirtz, C.; Khan, U.; De, S.; O'Neill, A.; Duesberg, G. S.; Grunlan, J. C.; Moriarty, G.; Chen, J.; Wang, J.; Minett, A. I.; Nicolosi, V.; Coleman, J. N. Large-Scale Exfoliation of Inorganic Layered Compounds in Aqueous Surfactant Solutions. *Adv. Mater.* **2011**, *23* (34), 3944–3948.
(64) Yu, X.; Prévot, M. S.; Sivula, K. Multiflake Thin Film Electronic Devices of Solution Processed 2D MoS_2 Enabled by Sonopolymer Assisted Exfoliation and Surface Modification. *Chem. Mater.* **2014**, *26* (20), 5892–5899.
(65) Guan, G.; Zhang, S.; Liu, S.; Cai, Y.; Low, M.; Teng, C. P.; Phang, I. Y.; Cheng, Y.; Duei, K. L.; Srinivasan, B. M.; Zheng, Y.; Zhang, Y.-W.; Han, M.-Y. Protein Induces Layer-by-Layer Exfoliation of Transition Metal Dichalcogenides. *J. Am. Chem. Soc.* **2015**, *137* (19), 6152–6155.
(66) Eng, A. Y. S.; Ambrosi, A.; Sofer, Z.; Šimek, P.; Pumera, M. Electrochemistry of Transition Metal Dichalcogenides: Strong Dependence on the Metal-to-Chalcogen Composition and Exfoliation Method. *ACS Nano* **2014**, *8* (12), 12185–12198.
(67) Zhang, Q.; Mei, L.; Cao, X.; Tang, Y.; Zeng, Z. Intercalation and Exfoliation Chemistries of Transition Metal Dichalcogenides. *J. Mater. Chem. A* **2020**, *8* (31), 15417–15444.
(68) Leong, S. X.; Mayorga-Martinez, C. C.; Chia, X.; Luxa, J.; Sofer, Z.; Pumera, M. 2H → 1T Phase Change in Direct Synthesis of WS_2 Nanosheets via Solution-Based Electrochemical Exfoliation and Their Catalytic Properties. *ACS Appl. Mater. Interfaces* **2017**, *9* (31), 26350–26356.
(69) Mayorga-Martinez, C. C.; Ambrosi, A.; Eng, A. Y. S.; Sofer, Z.; Pumera, M. Transition Metal Dichalcogenides (MoS_2, $MoSe_2$, WS_2 and WSe_2) Exfoliation Technique Has Strong Influence upon Their Capacitance. *Electrochem. Commun.* **2015**, *56*, 24–28.
(70) Tan, S. M.; Sofer, Z.; Luxa, J.; Pumera, M. Aromatic-Exfoliated Transition Metal Dichalcogenides: Implications for Inherent Electrochemistry and Hydrogen Evolution. *ACS Catal.* **2016**, *6* (7), 4594–4607.
(71) Yang, Y.; Hou, H.; Zou, G.; Shi, W.; Shuai, H.; Li, J.; Ji, X. Electrochemical Exfoliation of Graphene-like Two-Dimensional Nanomaterials. *Nanoscale* **2019**, *11* (1), 16–33.
(72) Shi, Y.; Li, H.; Li, L.-J. Recent Advances in Controlled Synthesis of Two-Dimensional Transition Metal Dichalcogenides via Vapour Deposition Techniques. *Chem. Soc. Rev.* **2015**, *44* (9), 2744–2756.
(73) Zhang, Y.; Yao, Y.; Sendeku, M. G.; Yin, L.; Zhan, X.; Wang, F.; Wang, Z.; He, J. Recent Progress in CVD Growth of 2D Transition Metal Dichalcogenides and Related Heterostructures. *Adv. Mater.* **2019**, *31* (41), 1901694.
(74) Xie, L. M. Two-Dimensional Transition Metal Dichalcogenide Alloys: Preparation, Characterization and Applications. *Nanoscale* **2015**, *7* (44), 18392–18401.
(75) Zhang, Y.; Zhang, L.; Zhou, C. Review of Chemical Vapor Deposition of Graphene and Related Applications. *Acc. Chem. Res.* **2013**, *46* (10), 2329–2339.

(76) Yue, R.; Barton, A. T.; Zhu, H.; Azcatl, A.; Pena, L. F.; Wang, J.; Peng, X.; Lu, N.; Cheng, L.; Addou, R.; McDonnell, S.; Colombo, L.; Hsu, J. W. P.; Kim, J.; Kim, M. J.; Wallace, R. M.; Hinkle, C. L. $HfSe_2$ Thin Films: 2D Transition Metal Dichalcogenides Grown by Molecular Beam Epitaxy. *ACS Nano* **2015**, *9* (1), 474–480.
(77) Jiao, L.; Liu, H. J.; Chen, J. L.; Yi, Y.; Chen, W. G.; Cai, Y.; Wang, J. N.; Dai, X. Q.; Wang, N.; Ho, W. K.; Xie, M. H. Molecular-Beam Epitaxy of Monolayer $MoSe_2$: Growth Characteristics and Domain Boundary Formation. *New J. Phys.* **2015**, *17* (5), 053023.
(78) Liu, H. J.; Jiao, L.; Xie, L.; Yang, F.; Chen, J. L.; Ho, W. K.; Gao, C. L.; Jia, J. F.; Cui, X. D.; Xie, M. H. Molecular-Beam Epitaxy of Monolayer and Bilayer WSe_2 : A Scanning Tunneling Microscopy/Spectroscopy Study and Deduction of Exciton Binding Energy. *2D Mater.* **2015**, *2* (3), 034004.
(79) Yue, R.; Nie, Y.; Walsh, L. A.; Addou, R.; Liang, C.; Lu, N.; Barton, A. T.; Zhu, H.; Che, Z.; Barrera, D.; Cheng, L.; Cha, P.-R.; Chabal, Y. J.; Hsu, J. W. P.; Kim, J.; Kim, M. J.; Colombo, L.; Wallace, R. M.; Cho, K.; Hinkle, C. L. Nucleation and Growth of WSe_2 : Enabling Large Grain Transition Metal Dichalcogenides. *2D Mater.* **2017**, *4* (4), 045019.
(80) Balasubramanyam, S.; Merkx, M. J. M.; Verheijen, M. A.; Kessels, W. M. M.; Mackus, A. J. M.; Bol, A. A. Area-Selective Atomic Layer Deposition of Two-Dimensional WS_2 Nanolayers. *ACS Mater. Lett.* **2020**, *2* (5), 511–518.
(81) Wirtz, C.; Hallam, T.; Cullen, C. P.; Berner, N. C.; O'Brien, M.; Marcia, M.; Hirsch, A.; Duesberg, G. S. Atomic Layer Deposition on 2D Transition Metal Chalcogenides: Layer Dependent Reactivity and Seeding with Organic Ad-Layers. *Chem. Commun.* **2015**, *51* (92), 16553–16556.
(82) Kim, Y.; Choi, D.; Woo, W. J.; Lee, J. B.; Ryu, G. H.; Lim, J. H.; Lee, S.; Lee, Z.; Im, S.; Ahn, J.-H.; Kim, W.-H.; Park, J.; Kim, H. Synthesis of Two-Dimensional MoS_2/Graphene Heterostructure by Atomic Layer Deposition Using MoF_6 Precursor. *Appl. Surf. Sci.* **2019**, *494*, 591–599.
(83) Kim, H. G.; Lee, H.-B.-R. Atomic Layer Deposition on 2D Materials. *Chem. Mater.* **2017**, *29* (9), 3809–3826.
(84) Mun, J.; Park, H.; Park, J.; Joung, D.; Lee, S.-K.; Leem, J.; Myoung, J.-M.; Park, J.; Jeong, S.-H.; Chegal, W.; Nam, S.; Kang, S.-W. High-Mobility MoS_2 Directly Grown on Polymer Substrate with Kinetics-Controlled Metal–Organic Chemical Vapor Deposition. *ACS Appl. Electron. Mater.* **2019**, *1* (4), 608–616.
(85) Kim, T.; Mun, J.; Park, H.; Joung, D.; Diware, M.; Won, C.; Park, J.; Jeong, S.-H.; Kang, S.-W. Wafer-Scale Production of Highly Uniform Two-Dimensional MoS_2 by Metal-Organic Chemical Vapor Deposition. *Nanotechnology* **2017**, *28* (18), 18LT01.
(86) Mun, J.; Park, H.; Park, J.; Joung, D.; Lee, S.-K.; Leem, J.; Myoung, J.-M.; Park, J.; Jeong, S.-H.; Chegal, W.; Nam, S.; Kang, S.-W. High-Mobility MoS_2 Directly Grown on Polymer Substrate with Kinetics-Controlled Metal–Organic Chemical Vapor Deposition. *ACS Appl. Electron. Mater.* **2019**, *1* (4), 608–616.
(87) Cwik, S.; Mitoraj, D.; Reyes, O. M.; Rogalla, D.; Peeters, D.; Kim, J.; Schütz, H. M.; Bock, C.; Beranek, R.; Devi, A. Direct Growth of MoS_2 and WS_2 Layers by Metal Organic Chemical Vapor Deposition. *Adv. Mater. Interfaces* **2018**, *5* (16), 1800140.

(88) Kalanyan, B.; Kimes, W. A.; Beams, R.; Stranick, S. J.; Garratt, E.; Kalish, I.; Davydov, A. V.; Kanjolia, R. K.; Maslar, J. E. Rapid Wafer-Scale Growth of Polycrystalline 2H-MoS_2 by Pulsed Metal–Organic Chemical Vapor Deposition. *Chem. Mater.* **2017**, *29* (15), 6279–6288.
(89) Eichfeld, S. M.; Hossain, L.; Lin, Y.-C.; Piasecki, A. F.; Kupp, B.; Birdwell, A. G.; Burke, R. A.; Lu, N.; Peng, X.; Li, J.; Azcatl, A.; McDonnell, S.; Wallace, R. M.; Kim, M. J.; Mayer, T. S.; Redwing, J. M.; Robinson, J. A. Highly Scalable, Atomically Thin WSe_2 Grown *via* Metal–Organic Chemical Vapor Deposition. *ACS Nano* **2015**, *9* (2), 2080–2087.
(90) Ataca, C.; Şahin, H.; Ciraci, S. Stable, Single-Layer MX_2 Transition-Metal Oxides and Dichalcogenides in a Honeycomb-Like Structure. *J. Phys. Chem. C* **2012**, *116* (16), 8983–8999.
(91) Enyashin, A. N.; Yadgarov, L.; Houben, L.; Popov, I.; Weidenbach, M.; Tenne, R.; Bar-Sadan, M.; Seifert, G. New Route for Stabilization of 1T-WS_2 and MoS_2 Phases. *J. Phys. Chem. C* **2011**, *115* (50), 24586–24591.
(92) Tan, S. J. R.; Abdelwahab, I.; Ding, Z.; Zhao, X.; Yang, T.; Loke, G. Z. J.; Lin, H.; Verzhbitskiy, I.; Poh, S. M.; Xu, H.; Nai, C. T.; Zhou, W.; Eda, G.; Jia, B.; Loh, K. P. Chemical Stabilization of 1T′ Phase Transition Metal Dichalcogenides with Giant Optical Kerr Nonlinearity. *J. Am. Chem. Soc.* **2017**, *139* (6), 2504–2511.
(93) Tan, C.; Luo, Z.; Chaturvedi, A.; Cai, Y.; Du, Y.; Gong, Y.; Huang, Y.; Lai, Z.; Zhang, X.; Zheng, L.; Qi, X.; Goh, M. H.; Wang, J.; Han, S.; Wu, X.-J.; Gu, L.; Kloc, C.; Zhang, H. Preparation of High-Percentage 1T-Phase Transition Metal Dichalcogenide Nanodots for Electrochemical Hydrogen Evolution. *Adv. Mater.* **2018**, *30* (9), 1705509.
(94) Yu, Y.; Nam, G.-H.; He, Q.; Wu, X.-J.; Zhang, K.; Yang, Z.; Chen, J.; Ma, Q.; Zhao, M.; Liu, Z.; Ran, F.-R.; Wang, X.; Li, H.; Huang, X.; Li, B.; Xiong, Q.; Zhang, Q.; Liu, Z.; Gu, L.; Du, Y.; Huang, W.; Zhang, H. High Phase-Purity 1T′-MoS_2 - and 1T′-$MoSe_2$ - Layered Crystals. *Nat. Chem.***2018**, *10* (6), 638–643.
(95) Friedman, A. L.; Hanbicki, A. T.; Perkins, F. K.; Jernigan, G. G.; Culbertson, J. C.; Campbell, P. M. Evidence for Chemical Vapor Induced 2H to 1T Phase Transition in MoX_2 (X = Se, S) Transition Metal Dichalcogenide Films. *Sci. Rep.* **2017**, *7* (1), 3836.
(96) Feng, Y.; Gong, S.; Du, E.; Chen, X.; Qi, R.; Yu, K.; Zhu, Z. 3R TaS_2 Surpasses the Corresponding 1T and 2H Phases for the Hydrogen Evolution Reaction. *J. Phys. Chem. C* **2018**, *122* (4), 2382–2390.
(97) Jun Toh, R.; Sofer, Z.; Luxa, J.; Sedmidubský, D.; Pumera, M. 3R Phase of MoS_2 and WS_2 Outperforms the Corresponding 2H Phase for Hydrogen Evolution. *Chem. Commun.* **2017**, *53* (21), 3054–3057.
(98) Zeng, Z.; Sun, X.; Zhang, D.; Zheng, W.; Fan, X.; He, M.; Xu, T.; Sun, L.; Wang, X.; Pan, A. Controlled Vapor Growth and Nonlinear Optical Applications of Large-Area 3R Phase WS_2 and WSe_2 Atomic Layers. *Adv. Funct. Mater.* **2019**, *29* (11), 1806874.
(99) Voiry, D.; Mohite, A.; Chhowalla, M. Phase Engineering of Transition Metal Dichalcogenides. *Chem. Soc. Rev.* **2015**, *44* (9), 2702–2712.
(100) Wang, R.; Yu, Y.; Zhou, S.; Li, H.; Wong, H.; Luo, Z.; Gan, L.; Zhai, T. Strategies on Phase Control in Transition Metal Dichalcogenides. *Adv. Funct. Mater.* **2018**, *28* (47), 1802473.

(101) Mak, K. F.; Lee, C.; Hone, J.; Shan, J.; Heinz, T. F. Atomically Thin MoS_2: A New Direct-Gap Semiconductor. *Phys. Rev. Lett.* **2010**, *105* (13), 136805.
(102) Zhang, Y.; Tang, T.-T.; Girit, C.; Hao, Z.; Martin, M. C.; Zettl, A.; Crommie, M. F.; Shen, Y. R.; Wang, F. Direct Observation of a Widely Tunable Bandgap in Bilayer Graphene. *Nature* **2009**, *459* (7248), 820–823.
(103) Balog, R.; Jørgensen, B.; Nilsson, L.; Andersen, M.; Rienks, E.; Bianchi, M.; Fanetti, M.; Lægsgaard, E.; Baraldi, A.; Lizzit, S.; Sljivancanin, Z.; Besenbacher, F.; Hammer, B.; Pedersen, T. G.; Hofmann, P.; Hornekær, L. Bandgap Opening in Graphene Induced by Patterned Hydrogen Adsorption. *Nat. Mater.* **2010**, *9* (4), 315–319.
(104) Steinhoff, A.; Kim, J.-H.; Jahnke, F.; Rösner, M.; Kim, D.-S.; Lee, C.; Han, G. H.; Jeong, M. S.; Wehling, T. O.; Gies, C. Efficient Excitonic Photoluminescence in Direct and Indirect Band Gap Monolayer MoS_2. *Nano Lett.* **2015**, *15* (10), 6841–6847.
(105) Sim, S.; Park, J.; Song, J.-G.; In, C.; Lee, Y.-S.; Kim, H.; Choi, H. Exciton Dynamics in Atomically Thin MoS_2: Interexcitonic Interaction and Broadening Kinetics. *Phys. Rev. B* **2013**, *88* (7), 075434.
(106) Lin, Y.; Ling, X.; Yu, L.; Huang, S.; Hsu, A. L.; Lee, Y.-H.; Kong, J.; Dresselhaus, M. S.; Palacios, T. Dielectric Screening of Excitons and Trions in Single-Layer MoS_2. *Nano Lett.* **2014**, *14* (10), 5569–5576.
(107) Late, D. J.; Shirodkar, S. N.; Waghmare, U. V.; Dravid, V. P.; Rao, C. N. R. Thermal Expansion, Anharmonicity and Temperature-Dependent Raman Spectra of Single- and Few-Layer $MoSe_2$ and WSe_2. *ChemPhysChem* **2014**, *15* (8), 1592–1598.
(108) Chen, S.-Y.; Zheng, C.; Fuhrer, M. S.; Yan, J. Helicity-Resolved Raman Scattering of MoS_2, $MoSe_2$, WS_2, and WSe_2 Atomic Layers. *Nano Lett.* **2015**, *15* (4), 2526–2532.
(109) Bilgin, I.; Raeliarijaona, A. S.; Lucking, M. C.; Hodge, S. C.; Mohite, A. D.; de Luna Bugallo, A.; Terrones, H.; Kar, S. Resonant Raman and Exciton Coupling in High-Quality Single Crystals of Atomically Thin Molybdenum Diselenide Grown by Vapor-Phase Chalcogenization. *ACS Nano* **2018**, *12* (1), 740–750.
(110) Nam, D.; Lee, J.-U.; Cheong, H. Excitation Energy Dependent Raman Spectrum of $MoSe_2$. *Sci. Rep.* **2015**, *5* (1), 17113.
(111) Saito, R.; Tatsumi, Y.; Huang, S.; Ling, X.; Dresselhaus, M. S. Raman Spectroscopy of Transition Metal Dichalcogenides. *J. Phys.: Condens. Matter* **2016**, *28* (35), 353002.
(112) Zhang, X.; Han, W. P.; Wu, J. B.; Milana, S.; Lu, Y.; Li, Q. Q.; Ferrari, A. C.; Tan, P. H. Raman Spectroscopy of Shear and Layer Breathing Modes in Multilayer MoS_2 *Phys. Rev. B* **2013**, *87* (11), 115413.
(113) Li, H.; Zhang, Q.; Yap, C.; Tay, B.; Edwin, T.; Oliver, A.; Baillargeat, D. From Bulk to Monolayer MoS_2: Evolution of Raman Scattering *Adv. Funct. Mater.* **2012,** *22* (7), 1385-1390
(114) Tonndorf, P.; Schmidt, R.; Böttger, P.; Zhang, X.; Börner, J.; Liebig, A.; Albrecht, M.; Kloc, C.; Gordan, O.; Zahn, D. R. T.; Vasconcellos, S. M. de; Bratschitsch, R. Photoluminescence Emission and Raman Response of Monolayer MoS_2, $MoSe_2$, and WSe_2. *Opt. Express, OE* **2013**, *21* (4), 4908–4916.

(115) Botello-Méndez, A. R.; López-Urías, F.; Terrones, M.; Terrones, H. Metallic and Ferromagnetic Edges in Molybdenum Disulfide Nanoribbons. *Nanotechnology* **2009**, *20* (32), 325703.
(116) Jaramillo, T.; Jørgensen, K.; Bonde, J.; Nielsen, J.; Horch, S.; Chorkendorff, I. Identification of Active Edge Sites for Electrochemical H_2 Evolution from MoS_2 Nanocatalysts *Science* **2007,** *317* (5834), 100-102
(117) Aljarb, A.; Fu, J.-H.; Hsu, C.-C.; Chuu, C.-P.; Wan, Y.; Hakami, M.; Naphade, D. R.; Yengel, E.; Lee, C.-J.; Brems, S.; Chen, T.-A.; Li, M.-Y.; Bae, S.-H.; Hsu, W.-T.; Cao, Z.; Albaridy, R.; Lopatin, S.; Chang, W.-H.; Anthopoulos, T. D.; Kim, J.; Li, L.-J.; Tung, V. Ledge-Directed Epitaxy of Continuously Self-Aligned Single-Crystalline Nanoribbons of Transition Metal Dichalcogenides. *Nat. Mater.* **2020**, 1–7.
(118) Sang, X.; Li, X.; Zhao, W.; Dong, J.; Rouleau, C. M.; Geohegan, D. B.; Ding, F.; Xiao, K.; Unocic, R. R. In Situ Edge Engineering in Two-Dimensional Transition Metal Dichalcogenides. *Nat. Commun.* **2018**, *9* (1), 2051.
(119) Karunadasa, H. I.; Montalvo, E.; Sun, Y.; Majda, M.; Long, J. R.; Chang, C. J. A Molecular MoS_2 Edge Site Mimic for Catalytic Hydrogen Generation. *Science* **2012**, *335* (6069), 698–702.
(120) Zhang, H.; Zhao, X.; Gao, Y.; Wang, H.; Wang, T.; Wei, S. Electronic and Magnetic Properties of $MoSe_2$ Armchair Nanoribbons Controlled by the Different Edge Structures. *Superlattices and Microstruct.* **2018**, *115*, 30–39.
(121) Wang, R.; Sun, H.; Ma, B.; Hu, J.; Pan, J. Edge Passivation Induced Single-Edge Ferromagnetism of Zigzag MoS_2 Nanoribbons. *Physics Letters A* **2017**, *381* (4), 301–306.
(122) Wang, Z. F.; Li, Q.; Zheng, H.; Ren, H.; Su, H.; Shi, Q. W.; Chen, J. Tuning the Electronic Structure of Graphene Nanoribbons through Chemical Edge Modification: A Theoretical Study. *Phys. Rev. B* **2007**, *75* (11), 113406.
(123) Rostami, H.; Asgari, R.; Guinea, F. Edge Modes in Zigzag and Armchair Ribbons of Monolayer MoS_2. *J. Phys.: Condens. Matter* **2016**, *28* (49), 495001.
(124) Zhao, G.; Rui, K.; Dou, S. X.; Sun, W. Heterostructures for Electrochemical Hydrogen Evolution Reaction: A Review. *Adv. Funct. Mater.* **2018**, *28* (43), 1803291.
(125) Sun, Z.; Martinez, A.; Wang, F. Optical Modulators with 2D Layered Materials. *Nat. Photon.* **2016**, *10* (4), 227–238..
(126) Geim, A. K.; Grigorieva, I. V. Van Der Waals Heterostructures. *Nature* **2013**, *499* (7459), 419–425.
(127) Tran, K.; Moody, G.; Wu, F.; Lu, X.; Choi, J.; Kim, K.; Rai, A.; Sanchez, D. A.; Quan, J.; Singh, A.; Embley, J.; Zepeda, A.; Campbell, M.; Autry, T.; Taniguchi, T.; Watanabe, K.; Lu, N.; Banerjee, S. K.; Silverman, K. L.; Kim, S.; Tutuc, E.; Yang, L.; MacDonald, A. H.; Li, X. Evidence for Moiré Excitons in van Der Waals Heterostructures. *Nature* **2019**, *567* (7746), 71–75.
(128) Liu, Y.; Weiss, N. O.; Duan, X.; Cheng, H.-C.; Huang, Y.; Duan, X. Van Der Waals Heterostructures and Devices. *Nat. Rev. Mater.* **2016**, *1* (9), 1–17.
(129) Wang, H.; Liu, F.; Fu, W.; Fang, Z.; Zhou, W.; Liu, Z. Two-Dimensional Heterostructures: Fabrication, Characterization, and Application. *Nanoscale* **2014**, *6* (21), 12250–12272.

(130) Komsa, H.-P.; Krasheninnikov, A. V. Electronic Structures and Optical Properties of Realistic Transition Metal Dichalcogenide Heterostructures from First Principles. *Phys. Rev. B* **2013**, *88* (8), 085318.
(131) Tartakovskii, A. Excitons in 2D Heterostructures. *Nat. Rev. Phys.* **2020**, *2* (1), 8–9.
(132) Xu, Y.-H.; Wang, J.-P. Direct Gas-Phase Synthesis of Heterostructured Nanoparticles through Phase Separation and Surface Segregation. *Adv. Mater.* **2008**, *20* (5), 994–999.
(133) Singh, R.; Doppalapudi, D.; Moustakas, T. D.; Romano, L. T. Phase Separation in InGaN Thick Films and Formation of InGaN/GaN Double Heterostructures in the Entire Alloy Composition. *Appl. Phys. Lett.* **1997**, *70* (9), 1089–1091.
(134) Li, J.; Yang, X.; Liu, Y.; Huang, B.; Wu, R.; Zhang, Z.; Zhao, B.; Ma, H.; Dang, W.; Wei, Z.; Wang, K.; Lin, Z.; Yan, X.; Sun, M.; Li, B.; Pan, X.; Luo, J.; Zhang, G.; Liu, Y.; Huang, Y.; Duan, X.; Duan, X. General Synthesis of Two-Dimensional van Der Waals Heterostructure Arrays. *Nature* **2020**, *579* (7799), 368–374.
(135) Jiang, C.; Xu, W.; Rasmita, A.; Huang, Z.; Li, K.; Xiong, Q.; Gao, W. Microsecond Dark-Exciton Valley Polarization Memory in Two-Dimensional Heterostructures. *Nat. Commun.* **2018**, *9* (1), 753.
(136) Kim, J.; Jin, C.; Chen, B.; Cai, H.; Zhao, T.; Lee, P.; Kahn, S.; Watanabe, K.; Taniguchi, T.; Tongay, S.; Crommie, M. F.; Wang, F. Observation of Ultralong Valley Lifetime in WSe_2/MoS_2 Heterostructures. *Sci. Adv.* **2017**, *3* (7), e1700518.
(137) Rasmita, A.; Gao, W. Opto-Valleytronics in the 2D van Der Waals Heterostructure. *Nano Res.* **2020**.
(138) Schaibley, J. R.; Yu, H.; Clark, G.; Rivera, P.; Ross, J. S.; Seyler, K. L.; Yao, W.; Xu, X. Valleytronics in 2D Materials. *Nat. Rev. Mater.* **2016**, *1* (11), 1–15.
(139) Duan, X.; Wang, C.; Shaw, J. C.; Cheng, R.; Chen, Y.; Li, H.; Wu, X.; Tang, Y.; Zhang, Q.; Pan, A.; Jiang, J.; Yu, R.; Huang, Y.; Duan, X. Lateral Epitaxial Growth of Two-Dimensional Layered Semiconductor Heterojunctions. *Nat. Nanotechnol.* **2014**, *9* (12), 1024–1030.
(140) Huang, C.; Wu, S.; Sanchez, A. M.; Peters, J. J. P.; Beanland, R.; Ross, J. S.; Rivera, P.; Yao, W.; Cobden, D. H.; Xu, X. Lateral Heterojunctions within Monolayer $MoSe_2$ – WSe_2 Semiconductors. *Nat. Mater.* **2014**, *13* (12), 1096–1101.
(141) Zhang, X.-Q.; Lin, C.-H.; Tseng, Y.-W.; Huang, K.-H.; Lee, Y.-H. Synthesis of Lateral Heterostructures of Semiconducting Atomic Layers. *Nano Lett.* **2015**, 6.
(142) Xie, S.; Tu, L.; Han, Y.; Huang, L.; Kang, K.; Lao, K. U.; Poddar, P.; Park, C.; Muller, D. A.; DiStasio, R. A.; Park, J. Coherent, Atomically Thin Transition-Metal Dichalcogenide Superlattices with Engineered Strain. *Science* **2018**, *359* (6380), 1131–1136.
(143) Pradhan, N. R.; Rhodes, D.; Xin, Y.; Memaran, S.; Bhaskaran, L.; Siddiq, M.; Hill, S.; Ajayan, P. M.; Balicas, L. Ambipolar Molybdenum Diselenide Field-Effect Transistors: Field-Effect and Hall Mobilities. *ACS Nano* **2014**, *8* (8), 7923–7929.
(144) Abderrahmane, A.; Ko, P. J.; Thu, T. V.; Ishizawa, S.; Takamura, T.; Sandhu, A. High Photosensitivity Few-Layered $MoSe_2$ Back-Gated Field-Effect Phototransistors. *Nanotechnology* **2014**, *25* (36), 365202.

(145) Das, S. R.; Kwon, J.; Prakash, A.; Delker, C. J.; Das, S.; Janes, D. B. Low-Frequency Noise in $MoSe_2$ Field Effect Transistors. *Appl. Phys. Lett.* **2015**, *106* (8), 083507.
(146) Larentis, S.; Fallahazad, B.; Tutuc, E. Field-Effect Transistors and Intrinsic Mobility in Ultra-Thin $MoSe_2$ Layers. *Appl. Phys. Lett.* **2012**, *101* (22), 223104.
(147) Yu, P.; Yu, X.; Lu, W.; Lin, H.; Sun, L.; Du, K.; Liu, F.; Fu, W.; Zeng, Q.; Shen, Z.; Jin, C.; Wang, Q. J.; Liu, Z. Fast Photoresponse from 1T Tin Diselenide Atomic Layers. *Adv. Funct. Mater.* **2016**, *26* (1), 137–145.
(148) Wang, Q.; Lai, J.; Sun, D. Review of Photo Response in Semiconductor Transition Metal Dichalcogenides Based Photosensitive Devices. *Opt. Mater. Express, OME* **2016**, *6* (7), 2313–2327.
(149) Massicotte, M.; Schmidt, P.; Vialla, F.; Schädler, K. G.; Reserbat-Plantey, A.; Watanabe, K.; Taniguchi, T.; Tielrooij, K. J.; Koppens, F. H. L. Picosecond Photoresponse in van Der Waals Heterostructures. *Nat. Nanotechnol.* **2016**, *11* (1), 42–46.
(150) Voiry, D.; Yang, J.; Chhowalla, M. Recent Strategies for Improving the Catalytic Activity of 2D TMD Nanosheets Toward the Hydrogen Evolution Reaction. *Adv. Mater.* **2016**, *28* (29), 6197–6206.
(151) Tsai, C.; Li, H.; Park, S.; Park, J.; Han, H. S.; Nørskov, J. K.; Zheng, X.; Abild-Pedersen, F. Electrochemical Generation of Sulfur Vacancies in the Basal Plane of MoS_2 for Hydrogen Evolution. *Nat. Commun.* **2017**, *8* (1), 15113.
(152) Koperski, M.; Nogajewski, K.; Arora, A.; Cherkez, V.; Mallet, P.; Veuillen, J.-Y.; Marcus, J.; Kossacki, P.; Potemski, M. Single Photon Emitters in Exfoliated WSe_2 Structures. *Nat. Nanotechnol.* **2015**, *10* (6), 503–506.
(153) Senellart, P.; Solomon, G.; White, A. High-Performance Semiconductor Quantum-Dot Single-Photon Sources. *Nat. Nanotechnol.* **2017**, *12* (11), 1026–1039.
(154) He, Y.-M.; Clark, G.; Schaibley, J. R.; He, Y.; Chen, M.-C.; Wei, Y.-J.; Ding, X.; Zhang, Q.; Yao, W.; Xu, X.; Lu, C.-Y.; Pan, J.-W. Single Quantum Emitters in Monolayer Semiconductors. *Nat. Nanotechnol.* **2015**, *10* (6), 497–502.
(155) Aivazian, G.; Gong, Z.; Jones, A. M.; Chu, R.-L.; Yan, J.; Mandrus, D. G.; Zhang, C.; Cobden, D.; Yao, W.; Xu, X. Magnetic Control of Valley Pseudospin in Monolayer WSe_2. *Nat. Phys.* **2015**, *11* (2), 148–152.
(156) Cha, S.; Noh, M.; Kim, J.; Son, J.; Bae, H.; Lee, D.; Kim, H.; Lee, J.; Shin, H.-S.; Sim, S.; Yang, S.; Lee, S.; Shim, W.; Lee, C.-H.; Jo, M.-H.; Kim, J. S.; Kim, D.; Choi, H. Generation, Transport and Detection of Valley-Locked Spin Photocurrent in WSe_2 – Graphene–Bi_2Se_3 Heterostructures. *Nat. Nanotechnol.* **2018**, *13* (10), 910–914.
(157) Liu, Y.; Gao, Y.; Zhang, S.; He, J.; Yu, J.; Liu, Z. Valleytronics in Transition Metal Dichalcogenides Materials. *Nano Res.* **2019**, *12* (11), 2695–2711.
(158) Ahn, E. C. 2D Materials for Spintronic Devices. *npj 2D Mater. Appl.* **2020**, *4* (1), 1–14.
(159) Grollier, J.; Querlioz, D.; Camsari, K. Y.; Everschor-Sitte, K.; Fukami, S.; Stiles, M. D. Neuromorphic Spintronics. *Nat. Electron.* **2020**, *3* (7), 360–370.
(160) He, Y.-M.; Clark, G.; Schaibley, J. R.; He, Y.; Chen, M.-C.; Wei, Y.-J.; Ding, X.; Zhang, Q.; Yao, W.; Xu, X.; Lu, C.-Y.; Pan, J.-W. Single Quantum Emitters in Monolayer Semiconductors. *Nat. Nanotechnol.* **2015**, *10* (6), 497–502.

(161) Liu, X.; Hersam, M. C. 2D Materials for Quantum Information Science. *Nat. Rev. Mater.* **2019**, *4* (10), 669–684.
(162) Bai, Y.; Zhou, L.; Wang, J.; Wu, W.; McGilly, L. J.; Halbertal, D.; Lo, C. F. B.; Liu, F.; Ardelean, J.; Rivera, P.; Finney, N. R.; Yang, X.-C.; Basov, D. N.; Yao, W.; Xu, X.; Hone, J.; Pasupathy, A. N.; Zhu, X.-Y. Excitons in Strain-Induced One-Dimensional Moiré Potentials at Transition Metal Dichalcogenide Heterojunctions. *Nat. Mater.* **2020**, 1–6.
(163) Choi, J.; Hsu, W.-T.; Lu, L.-S.; Sun, L.; Cheng, H.-Y.; Lee, M.-H.; Quan, J.; Tran, K.; Wang, C.-Y.; Staab, M.; Jones, K.; Taniguchi, T.; Watanabe, K.; Chu, M.-W.; Gwo, S.; Kim, S.; Shih, C.-K.; Li, X.; Chang, W.-H. Moiré Potential Impedes Interlayer Exciton Diffusion in van Der Waals Heterostructures. *Sci. Adv.* **2020**, *6* (39), eaba8866.
(164) Seyler, K. L.; Rivera, P.; Yu, H.; Wilson, N. P.; Ray, E. L.; Mandrus, D. G.; Yan, J.; Yao, W.; Xu, X. Signatures of Moiré-Trapped Valley Excitons in $MoSe_2/WSe_2$ Heterobilayers. *Nature* **2019**, *567* (7746), 66–70.
(165) Xu, Y.; Horn, C.; Zhu, J.; Tang, Y.; Ma, L.; Li, L.; Liu, S.; Watanabe, K.; Taniguchi, T.; Hone, J. C.; Shan, J.; Mak, K. F. Creation of Moiré Bands in a Monolayer Semiconductor by Spatially Periodic Dielectric Screening. *Nat. Mater.* **2021**, 1–5.
(166) Cao, Y.; Fatemi, V.; Fang, S.; Watanabe, K.; Taniguchi, T.; Kaxiras, E.; Jarillo-Herrero, P. Unconventional Superconductivity in Magic-Angle Graphene Superlattices. *Nature* **2018**, *556* (7699), 43–50.
(167) Cao, Y.; Fatemi, V.; Demir, A.; Fang, S.; Tomarken, S. L.; Luo, J. Y.; Sanchez-Yamagishi, J. D.; Watanabe, K.; Taniguchi, T.; Kaxiras, E.; Ashoori, R. C.; Jarillo-Herrero, P. Correlated Insulator Behaviour at Half-Filling in Magic-Angle Graphene Superlattices. *Nature* **2018**, *556* (7699), 80–84.
(168) Tarnopolsky, G.; Kruchkov, A. J.; Vishwanath, A. Origin of Magic Angles in Twisted Bilayer Graphene. *Phys. Rev. Lett.* **2019**, *122* (10), 106405.
(169) Kerelsky, A.; McGilly, L. J.; Kennes, D. M.; Xian, L.; Yankowitz, M.; Chen, S.; Watanabe, K.; Taniguchi, T.; Hone, J.; Dean, C.; Rubio, A.; Pasupathy, A. N. Maximized Electron Interactions at the Magic Angle in Twisted Bilayer Graphene. *Nature* **2019**, *572* (7767), 95–100.
(170) Choi, Y.; Kemmer, J.; Peng, Y.; Thomson, A.; Arora, H.; Polski, R.; Zhang, Y.; Ren, H.; Alicea, J.; Refael, G.; von Oppen, F.; Watanabe, K.; Taniguchi, T.; Nadj-Perge, S. Electronic Correlations in Twisted Bilayer Graphene near the Magic Angle. *Nat. Phys.* **2019**, *15* (11), 1174–1180.
(171) Lu, X.; Stepanov, P.; Yang, W.; Xie, M.; Aamir, M. A.; Das, I.; Urgell, C.; Watanabe, K.; Taniguchi, T.; Zhang, G.; Bachtold, A.; MacDonald, A. H.; Efetov, D. K. Superconductors, Orbital Magnets and Correlated States in Magic-Angle Bilayer Graphene. *Nature* **2019**, *574* (7780), 653–657.
(172) Zhang, X.; Lai, Z.; Liu, Z.; Tan, C.; Huang, Y.; Li, B.; Zhao, M.; Xie, L.; Huang, W.; Zhang, H. A Facile and Universal Top-Down Method for Preparation of Monodisperse Transition-Metal Dichalcogenide Nanodots. *Angew. Chem. Int. Ed.* **2015**, *54* (18), 5425–5428.

(173) Wu, H.; Yang, R.; Song, B.; Han, Q.; Li, J.; Zhang, Y.; Fang, Y.; Tenne, R.; Wang, C. Biocompatible Inorganic Fullerene-Like Molybdenum Disulfide Nanoparticles Produced by Pulsed Laser Ablation in Water. *ACS Nano* **2011**, *5* (2), 1276–1281.
(174) Roy, S.; Neupane, G. P.; Dhakal, K. P.; Lee, J.; Yun, S. J.; Han, G. H.; Kim, J. Observation of Charge Transfer in Heterostructures Composed of $MoSe_2$ Quantum Dots and a Monolayer of MoS_2 or WSe_2. *J. Phys. Chem. C* **2017**, *121* (3), 1997–2004.
(175) Zhang, S.; Liu, X.; Liu, C.; Luo, S.; Wang, L.; Cai, T.; Zeng, Y.; Yuan, J.; Dong, W.; Pei, Y.; Liu, Y. MoS_2 Quantum Dot Growth Induced by S Vacancies in a $ZnIn_2S_4$ Monolayer: Atomic-Level Heterostructure for Photocatalytic Hydrogen Production. *ACS Nano* **2018**, *12* (1), 751–758.
(176) Ou, G.; Fan, P.; Ke, X.; Xu, Y.; Huang, K.; Wei, H.; Yu, W.; Zhang, H.; Zhong, M.; Wu, H.; Li, Y. Defective Molybdenum Sulfide Quantum Dots as Highly Active Hydrogen Evolution Electrocatalysts. *Nano Res.* **2018**, *11* (2), 751–761.
(177) Srivastava, A.; Sidler, M.; Allain, A. V.; Lembke, D. S.; Kis, A.; Imamoğlu, A. Optically Active Quantum Dots in Monolayer WSe_2. *Nat. Nanotechnol.* **2015**, *10* (6), 491–496.
(178) Chakraborty, C.; Kinnischtzke, L.; Goodfellow, K. M.; Beams, R.; Vamivakas, A. N. Voltage-Controlled Quantum Light from an Atomically Thin Semiconductor. *Nat. Nanotechnol.* **2015**, *10* (6), 507–511.
(179) Lu, X.; Chen, X.; Dubey, S.; Yao, Q.; Li, W.; Wang, X.; Xiong, Q.; Srivastava, A. Optical Initialization of a Single Spin-Valley in Charged WSe_2 Quantum Dots. *Nat. Nanotechnol.* **2019**, *14* (5), 426–431.
(180) Altaisky, M. V.; Zolnikova, N. N.; Kaputkina, N. E.; Krylov, V. A.; Lozovik, Y. E.; Dattani, N. S. Towards a Feasible Implementation of Quantum Neural Networks Using Quantum Dots. *Appl. Phys. Lett.* **2016**, *108* (10), 103108.
(181) Kumar, S.; Kaczmarczyk, A.; Gerardot, B. D. Strain-Induced Spatial and Spectral Isolation of Quantum Emitters in Mono- and Bilayer WSe_2. *Nano Lett.* **2015**, *15* (11), 7567–7573.
(182) Mortemousque, P.-A.; Chanrion, E.; Jadot, B.; Flentje, H.; Ludwig, A.; Wieck, A. D.; Urdampilleta, M.; Bäuerle, C.; Meunier, T. Coherent Control of Individual Electron Spins in a Two-Dimensional Quantum Dot Array. *Nat. Nanotechnol.* **2020**, 1–6.
(183) Chowdhury, T.; Sadler, E. C.; Kempa, T. J. Progress and Prospects in Transition-Metal Dichalcogenide Research Beyond 2D. *Chem. Rev.* **2020**, *120* (22), 12563–12591.
(184) Bai, Y.; Zhang, R.; Ye, X.; Zhu, Z.; Xie, H.; Shen, B.; Cai, D.; Liu, B.; Zhang, C.; Jia, Z.; Zhang, S.; Li, X.; Wei, F. Carbon Nanotube Bundles with Tensile Strength over 80 GPa. *Nat. Nanotechnol.* **2018**, *13* (7), 589–595.
(185) Nguyen, G. D.; Tsai, H.-Z.; Omrani, A. A.; Marangoni, T.; Wu, M.; Rizzo, D. J.; Rodgers, G. F.; Cloke, R. R.; Durr, R. A.; Sakai, Y.; Liou, F.; Aikawa, A. S.; Chelikowsky, J. R.; Louie, S. G.; Fischer, F. R.; Crommie, M. F. Atomically Precise Graphene Nanoribbon Heterojunctions from a Single Molecular Precursor. *Nat. Nanotechnol.* **2017**, *12* (11), 1077–1082.

(186) Yang, D. J.; Zhang, Q.; Chen, G.; Yoon, S. F.; Ahn, J.; Wang, S. G.; Zhou, Q.; Wang, Q.; Li, J. Q. Thermal Conductivity of Multiwalled Carbon Nanotubes. *Phys. Rev. B* **2002**, *66* (16), 165440.
(187) Tapasztó, L.; Dobrik, G.; Lambin, P.; Biró, L. P. Tailoring the Atomic Structure of Graphene Nanoribbons by Scanning Tunnelling Microscope Lithography. *Nat. Nanotechnol.* **2008**, *3* (7), 397–401.
(188) Fujii, M.; Zhang, X.; Xie, H.; Ago, H.; Takahashi, K.; Ikuta, T.; Abe, H.; Shimizu, T. Measuring the Thermal Conductivity of a Single Carbon Nanotube. *Phys. Rev. Lett.* **2005**, *95* (6), 065502.
(189) Gaulke, M.; Janissek, A.; Peyyety, N. A.; Alamgir, I.; Riaz, A.; Dehm, S.; Li, H.; Lemmer, U.; Flavel, B. S.; Kappes, M. M.; Hennrich, F.; Wei, L.; Chen, Y.; Pyatkov, F.; Krupke, R. Low-Temperature Electroluminescence Excitation Mapping of Excitons and Trions in Short-Channel Monochiral Carbon Nanotube Devices. *ACS Nano* **2020**, *14* (3), 2709–2717.
(190) Wan, H.; Cao, Y.; Lo, L.-W.; Zhao, J.; Sepúlveda, N.; Wang, C. Flexible Carbon Nanotube Synaptic Transistor for Neurological Electronic Skin Applications. *ACS Nano* **2020**, *14* (8), 10402–10412.
(191) Kim, S.; Yoon, J.; Kim, H.-D.; Choi, S.-J. Carbon Nanotube Synaptic Transistor Network for Pattern Recognition. *ACS Appl. Mater. Interfaces* **2015**, *7* (45), 25479–25486.
(192) Kim, K.; Chen, C.-L.; Truong, Q.; Shen, A. M.; Chen, Y. A Carbon Nanotube Synapse with Dynamic Logic and Learning. *Adv. Mater.* **2013**, *25* (12), 1693–1698.
(193) Rizzo, D. J.; Veber, G.; Cao, T.; Bronner, C.; Chen, T.; Zhao, F.; Rodriguez, H.; Louie, S. G.; Crommie, M. F.; Fischer, F. R. Topological Band Engineering of Graphene Nanoribbons. *Nature* **2018**, *560* (7717), 204–208.
(194) Pan, M.; Girão, E. C.; Jia, X.; Bhaviripudi, S.; Li, Q.; Kong, J.; Meunier, V.; Dresselhaus, M. S. Topographic and Spectroscopic Characterization of Electronic Edge States in CVD Grown Graphene Nanoribbons. *Nano Lett.* **2012**, *12* (4), 1928–1933.
(195) Orlof, A.; Ruseckas, J.; Zozoulenko, I. V. Effect of Zigzag and Armchair Edges on the Electronic Transport in Single-Layer and Bilayer Graphene Nanoribbons with Defects. *Phys. Rev. B* **2013**, *88* (12), 125409.
(196) Demczyk, B. G.; Wang, Y. M.; Cumings, J.; Hetman, M.; Han, W.; Zettl, A.; Ritchie, R. O. Direct Mechanical Measurement of the Tensile Strength and Elastic Modulus of Multiwalled Carbon Nanotubes. *Mater. Sci. Eng. A* **2002**, *334* (1), 173–178.
(197) Li, F.; Cheng, H. M.; Bai, S.; Su, G.; Dresselhaus, M. S. Tensile Strength of Single-Walled Carbon Nanotubes Directly Measured from Their Macroscopic Ropes. *Appl. Phys. Lett.* **2000**, *77* (20), 3161–3163.

Chapter 2: Chalcogen Incorporation in Reduced Molybdenum Oxides

The work presented in this chapter has been published as:

E. C. Sadler, T. J. Kempa "Chalcogen Incorporation Process During High Vacuum Conversion of Bulk Mo Oxides to Mo Dichalcogenides"

ACS Appl. Elect. Mater. **2**, 1020-1025 (2020)

2.1 Introduction

In the development of 2D TMDs one of the principal questions has remained the mechanism of growth for these materials during gas phase processes such as chemical vapor deposition. While this topic has been untouched by a large portion of the community, understanding the formation of low-dimensional TMDs offers the opportunity to modify these materials in situ during growth to engender novel and exotic compositions, morphologies and therefore modulate resulting properties on these materials. Additionally, understanding how TMD reactions proceed at milder reaction conditions opens up a wide range of new chemistries that can be introduced to TMD materials. Particularly in the advancement of sophisticated synthetic tools, such as labile surfaces used in the directed growth of TMDs, or in vapor-liquid-solid growth of

TMDs, being able to influence TMD growths *in situ* with milder conditions is extremely advantageous.

Generally, the formation of transition metal dichalcogenides involve the chalcogenation of a parent material. These parent materials can be oxides, carbonyls or pure metals.[1–6] At present, there have been two main pathways for chalcogenation of a transition metal reactant. In the first (concerted) pathway, the vaporized metal species (normally an oxide, such as MoO_3 or MoO_2) in the gas phase encounters gas phase chalcogen molecules which reduce the Mo containing species to form an intermediate MoO_xA_y where A is a chalcogen. This intermediate deposits on the surface and is suffused with chalcogen vapor and grows laterally to form a low-dimensional fully chalcogenated TMD material. There are other Mo containing precursors utilized heavily in 2D and bulk TMD growth, such as $Mo(CO)_6$ or MoO_2. For the former, MOCVD techniques utilize liquid metal organic material precursors to have more precise control over the diffusion of reactant materials into the reaction chambers.[7–9] Other nonvolatile reactants, such as MoO_2, offer an already +4 valency metal which greatly reduces the thermodynamic barrier to reduction and incorporation of chalcogen into the Mo- material, though MoO_2 has not been utilized in the majority of cases. The mechanistic outcomes from MOCVD may differ greatly from utilizing CVD methods and is not a focus of this work. The principal avenue towards growth of

TMDs is chemical vapor deposition therefore this method requires careful examination to uncover mechanistic fundamentals.

Earlier works demonstrate that the chalcogen species can form a substitutional reduction of Mo from +6 to +4 valency. The structure of MoO_3 causes an O atom to stick out in space away from the surface of the material and the initial substitutional chalcogenation reaction conserves the +6 valency before forming a +4 TMD (Fig. 2.1).[10]

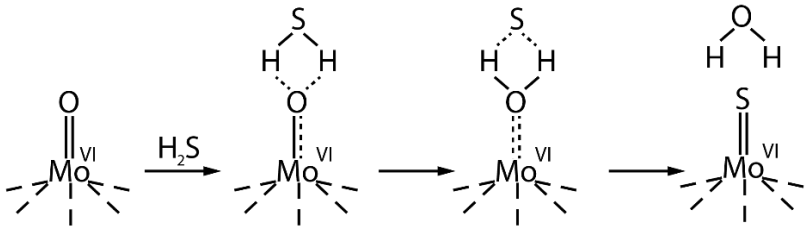

Figure 2.1. Scheme showing a proposed mechanism for the initial abstraction of a Mo atom in a MoO_3 crystal possessing +6 valency. A H_2S molecule abstracts O to Create H_2O and is left with a single S atom on the Mo.[10]

This geometry allows the S atom, in the form of H_2S as depicted in Fig. 2.1, to substitute a S atom for an O atom and create a leaving group of H_2O. However, many sulfur containing TMD reactions do not utilize H_2S due to the inherent toxicity in that precursor and in the majority of syntheses most likely do not directly follow the mechanism depicted in Fig. 2.1.[10–13]. Most low-dimensional TMD reactions utilize a metal precursor and chalcogen powder. In these reactions, the mechanism of sulfur reduction has been less clear. In this chapter,

bulk intermediates of MoS_2, namely MoO_{3-x} are isolated and used to elucidate the route of incorporation of sulfur atoms into the material. Bulk crystals were specifically chosen over low-dimensional crystals because the isolation of partially chalcogenated intermediates is extremely difficult owing to their rapid synthesis time upon deposition and the practical challenges in monitoring a cross-section of a monolayer.

The gas phase reaction pathway of volatilized Mo oxide powder with sulfur has been explored by several studies that isolate the intermediate MoO_xA_y species from reduction by chalcogens.[14,15] These studies demonstrate that these moieties have a radial conversion to create fullerene like nano-structures with the chalcogen species on the exterior (Fig. 2.2).

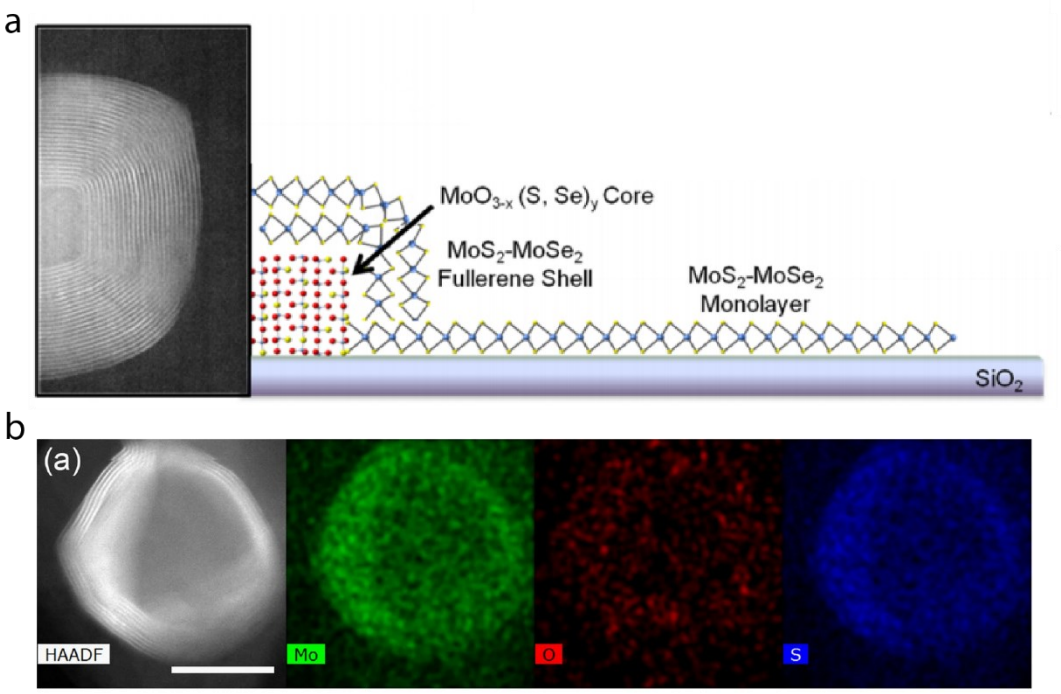

Figure 2.2. (a) Transmission electron micrograph of a core-shell fullerene structure derived from a gaseous reaction and following deposition process where the core is a intermediate partially sulfidated MoO_3 and the shell is a fully chalcogenated TMD. Scheme depicting this chemical topology and ensuing lateral growth for 2D TMDs.[14] (b) HAADF-STEM image of a core-shell fullerene structure derived from a gaseous reaction and following deposition process. STEM-EDS maps show considerably more S, and therefore MoS_2, character at the edges of the fullerene structure.[15]

One unanswered question is the identification of the S containing moieties that cause the reduction on the surface of Mo containing species. It has been hypothesized that an S_2 moiety is the reducing species in the reaction, though more work is required on this front.[16] Because these S_2 species are most likely not highly reductive species, earlier efforts at synthesizing sulfide-based TMDs

utilized highly reductive species such as H_2S as mentioned previously most likely cannot be used as precedence in understanding how chalcogen powder based reactions proceed. Though this is an important aspect of current TMD synthesis, it is outside the scope of this work.

There is currently little understanding in how the solid-vapor interface behaves when sub-oxide species undergo chalcogenation. This work seeks to further understand that interface. Though this work does not comment on the nature of the S containing moiety participating in the reduction of the oxide precursor, it does comment on how intermediates in the TMD process preferentially form TMD moieties. This result may unlock the potential to reliably and at large scales integrate with bulk processing capabilities to create wide ranging TMD heterostructures more efficiently.

Additionally, the limited work on investigating the mechanism of TMD synthesis has focused on a concerted pathway like what is observed in Fig. 2.2 These reaction pathways, while the dominant method in assembling low-dimensional TMDs, do not constitute the entirety of low-dimensional TMD growths. Many studies have also utilized a two-step growth process where some metal precursor already exists on the surface prior to vaporization of the chalcogen source.[17–20] These two-step routes have advantages in several cases including a lower number of synthetic variables with only one interface, namely

the solid-gas interface, requiring tuning instead of both the gas phase reaction and deposition process. Further, by using the two-step pathway we can investigate partially reduced intermediates as starting materials that are difficult to isolate for concerted growths. To date there have been an increasing emphasis on utilizing multi-step deposition and conversion of materials. The stark advantages in this method is the synthesis of controllable and large area TMD 2D materials. The chalcogenation of large area Mo metal deposited on a surface has shown to result in both large scale area 2D TMDs and in a different experiment showed that the Mo metal can break apart and form normal mesoscale TMD domains.[20] One of the main benefits of this method is the processability of TMD crystals utilizing this method. Wafer-scale metals evaporation combined with two-step sulfurization procedures, would create a far simpler reaction pathway for wide-scale adoption of TMDs compared to concerted, single-step, powder-reliant syntheses.

The goal of this work was to take inspiration from the two-step pathways in forming TMD materials that can inform on several aspects of TMD growth including low-dimensional MoS_2 growth. To this end we first deposit a reduced Mo containing oxide. Following preparation of this precursor, we sulfidate the partially reduced oxide and analyze what the preferential chalcogenation sites are in the reduced oxo-sulfide crystal. We carry out this chalcogenation at lower

temperatures, down to 300 °C, which is far from the norm of 650 – 800 °C used in the majority of MoS_2 reactions to date and show that milder conditions can yield partially chalcogenated samples which may be useful in future methods that explore interfacing TMD materials with other materials such as polymers and metal organic frameworks that are not as amenable to high reaction temperatures.[21,22]

2.2 Experimental Methods

CVD Reactor. Our home-built chemical vapor deposition (CVD) system is a versatile quartz tube hot-wall reactor design with a manifold of mass flow controllers (MKS Instruments: GM50A series MFCs) and a closed-loop pressure control system (MKS Instruments: 640B pressure controller). The manifold and pressure control circuits are both operated through custom LabView scripts running on a PC. The furnace (Thermo Scientific-Lindberg Blue M 3-Zone) has three independently controllable zones; each of which measures 25 cm in length and can reach temperatures of 1200 °C. A 400 °C temperature differential can be maintained between adjacent zones through the use of thermal inserts. A high-vacuum pump (Leybold: LV80 screw pump) is used to evacuate our CVD system to a base pressure of < 0.01 mTorr and is able to safely manage any toxic or pyrophoric effluent. The metal-sealed GM50A series mass flow controllers on our CVD reactor permit highly accurate (1% setpoint accuracy) flow control and

are accompanied by NIST traceable calibration sheets. Prior to all CVD reactions, we thoroughly washed and then performed a bake-out of quartz tubes (Quartz Plus: 22 mm inner diameter, 25.4 mm outer diameter) at 500 °C for 2 h under a 50 sccm N_2 flow. A schematic of this reactor is shown here (Fig. 2.3).

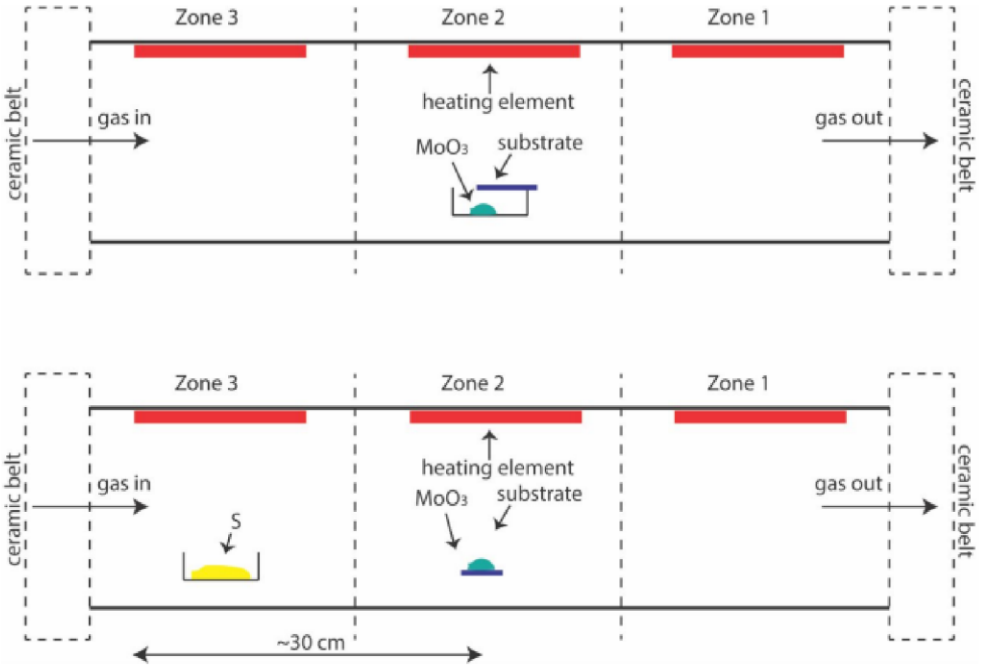

Figure 2.3. Schematic of the deposition of MoO_{3-x} (top) utilizing custom-built chemical vapor deposition instrument. Schematic of the sulfidation of MoO_{3-x} with sulfur powder (bottom) utilizing custom-built chemical vapor deposition instrument.

Deposition of MoO_{3-x}. Twenty milligrams of MoO_3 powder (Strem Chemicals) was placed in a 5 mm × 5 mm × 10 mm alumina crucible. This crucible was placed in the middle-heated zone of our CVD reactor. A Si substrate (Nova Electronic Materials) with a 200 nm SiO_2 topmost layer was cleaned by

sonication in acetone and isopropanol. Following sonication, a 15 min O_2 plasma treatment was conducted to remove residual organic contaminants from the surface SiO_2 layer. The substrate was placed face-down on the alumina boat containing MoO_3 powder. After the CVD reactor was evacuated to a base pressure of 1×10^{-5} Torr, the furnace zone containing the crucible and SiO_2 substrate was heated to 500 °C over 40 min. Once the temperature of the middle zone had reached 400 °C, N_2 at a flow rate of 20 sccm was introduced. At 500 °C, the system was pressurized to 40 Torr and held at these conditions for 15 min After 15 min, the reaction was quenched by ending the heating process, opening the furnace lid, and increasing the N_2 flow to 100 sccm.

Sulfidation or Selenation of MoO_{3-x}. SiO_2 on a Si substrate covered with MoO_{3-x} deposits (prepared as described in Deposition of MoO_{3-x}) was placed face-up in the middle-heated zone of our CVD reactor. An amount of 160 mg of S or Se powder (Sigma-Aldrich) was loaded into an alumina crucible and positioned in a zone immediately upstream of the middle zone. This upstream zone was maintained at a set point temperature of 250 or 450 °C for sulfidation or selenation, respectively. After evacuating the CVD reactor to a base pressure of 1×10^{-5} Torr, heating was initiated. The middle zone was heated to a desired set point at a heating rate of 12.5 °C/min. N_2 at a flow of 20 sccm was introduced, and the CVD reactor was pressurized to 40 Torr. Thereafter, heating was

initiated, and once the furnace reached the desired set point, the reaction was allowed to proceed at these conditions for varying lengths of time.

Concurrent or Stepwise Chalcogenation of MoO_{3-x}. Concurrent: We followed the methods described in Sulfidation or Selenation except that both S and Se powders were loaded into the upstream zone, which was held at 400 °C. Stepwise: We followed the methods described in Sulfidation or Selenation with one additional step. After quenching the reaction and cooling the reactor to below 100 °C, 160 mg of the chalcogen not used in the previous step was placed in a clean crucible. Raman spectra collected from the products of (a) selenation, (b) concurrent selenation and sulfidation, and (c) a stepwise process of selenation followed by sulfidation.

Preparation of Fiducial Markers. A JEOL JSM 6400 system running Nanometer Program Generation Software (JC Nabity Lithography Systems) was used to pattern custom features (drafted within a 2D ASCII CAD file) into a polymethyl methacrylate (MicroChem) electron beam resist, which had been previously spin coated onto the SiO_2 substrate. Following development in methyl isobutyl ketone, rinsing in isopropyl alcohol, and drying, the patterned substrate was introduced into the chamber of a thermal evaporator (Leybold Univex 250) and 20 nm of Au was deposited. Following Au lift-off in acetone, the substrate with fiducial markers were cleaned and used as is.

Raman Spectroscopy. Micro-Raman scattering was measured from various spots in a backscattering geometry using a Horiba Jobin Yvon T46000 spectrometer equipped with a liquid N_2-cooled CCD detector. Excitation at 514 nm was provided by an Ar/Kr laser. A 50x objective lens was used, and the laser power was maintained at 1 mW. The laser probe size was ~2 μm

AFM. The topographies of MoO_{3-x} deposits before and after sulfidation were obtained using a Keysight 5500 atomic force microscope (AFM). AFM raw files (.mi) were processed in Gwyddion 2.51. A "Facet Level" function was applied to the raw data. Four line profiles in close proximity to one another were extracted from the leveled raw data and averaged to produce the topographic profile of the crystals.

FIB Milling of Deposits for STEM Analysis. Focused ion-beam milling of the single deposit studied was performed on a Tescan GAIA FIB–SEM with a Ga ion beam. A thin coating of tungsten was deposited in situ over the sample to protect the cross section during the milling process. The FIB process was carried out at 30 kV with a probe current of 2 nA for the cross-sectioning and initial polishing of the crystal. Final polishing of the cross section to a 100 nm thickness was performed with a 40 pA probe current.

STEM Imaging and EDS Mapping. STEM imaging was performed using JEOL JEM 2100 field-emission TEM. EDS mapping was performed at 200 kV. Line profiles were extracted by integrating detector X-ray counts for each element in the STEM map. The normalized data shown were obtained by dividing the total counts for each element by the sum of all X-ray counts detected from the sample (Mo, O, S, and Si). Such normalization accounts for any changes in the overall signal arising from, for example, local differences in sample thickness.

XPS. XPS analysis was performed using a PHI 5600 X-ray photoelectron spectrometer equipped with a Mg Kα flood source (1253.6 eV) and a hemispherical energy analyzer. High-resolution multiplex scans were collected at ultrahigh vacuum (8×10^{-8} Torr) with a source power of 300 W, a pass energy of 23.5 eV, 5 sweeps/ spectrum, and 0.025 eV/step. Survey scans (1200−0 eV binding energy) were collected at the same ultrahigh vacuum condition with a pass energy of 187.785 eV, 2 sweeps/spectrum, and 1.6 eV/step. Spectra were analyzed using CASA XPS software.

pXRD. Powder X-ray diffraction data were collected on a Bruker D8 Focus diffractometer using a Cu X-ray source (Kα = 8.04 keV, 1.5406 Å).

2.3 Discussion

The vast majority of low-dimensional TMD synthesis is done at temperatures ranging from 650 °C to 1000 °C. However, these high temperatures limit any opportunity to isolate selected intermediates that may give clues to how TMD growth reactions proceed. In this work we utilized a two-step process that allows us to do isolate sub-oxides and isolate the chalcogenation portion of the TMD reaction. (Fig. 2.4).

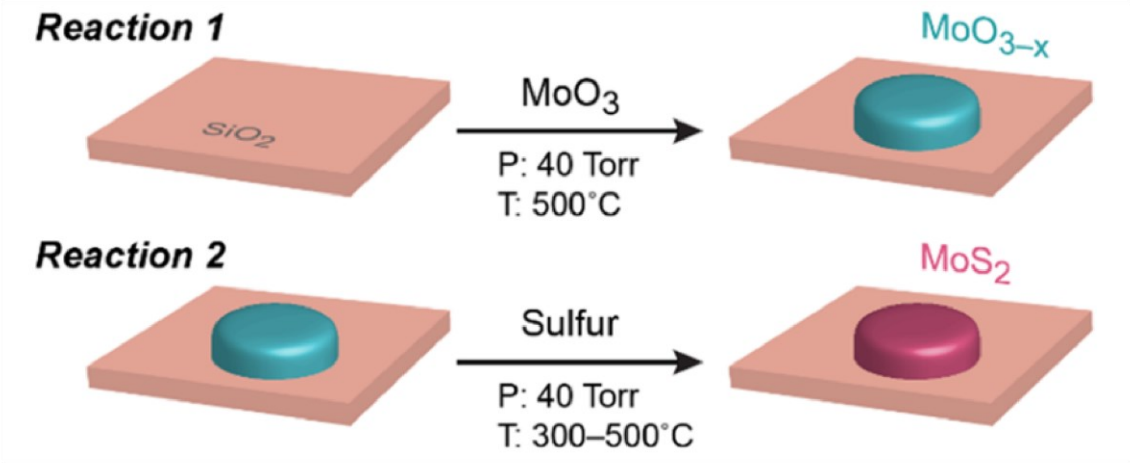

Figure 2.4. Schematic showing the two-step reaction process for synthesizing MoS_2. Depending on the parameters set in Reaction 2, either a fully sulfidated MoS_2 crystal can be achieved or a mixture between MoS_2 and the precursor, MoO_{3-x}.

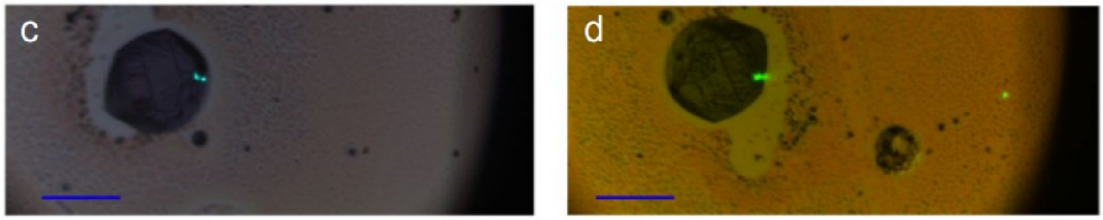

Figure 2.5. Optical micrographs taken at 50x magnification showing a single bulk crystal before (left) and after (right) sulfidation at 400 °C. This crystal was tracked through deposited Au markers. Scale bars, 20 μm.

Optical micrographs of MoO_{3-x} crystalline deposits synthesized by the scheme shown in Fig. 2.3 and then sulfidated at 400 °C are shown (Fig. 2.5). The primary single crystal tracked through the deposition and sulfidation retains its morphology and demonstrates retention in crystal quality post sulfidation (Fig. 2.5). Though clearly these are bulk crystals, we can more clearly measure trends in the chalcogenation of samples with greater accuracy due to an appreciable height in these crystals, unlike in monolayer TMDs. We also note the complete retention in morphology of before and after sulfidation of the sub-oxide crystal is critical in evaluating the chalcogen process. These crystalline deposits can be altered in their size and breadth by reactor temperature and pressure. In conditions utilized here, as outlined in section 2.2 has a relatively narrow width distribution (Fig. 2.6).

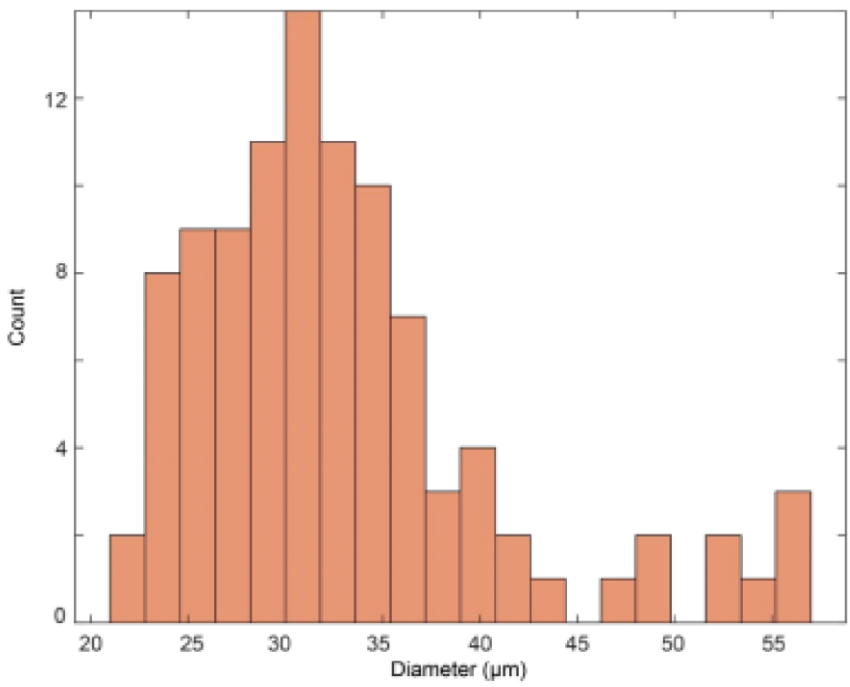

Figure 2.6. Histogram showing a width distribution for 100 MoO_{3-x} crystallites after deposition in Reaction 1 of Figure 2.4. The average crystallite diameter was 33.8 um.

Initial efforts at characterizing the change from MoO_{3-x} to a partial or fully sulfidated species was done using ex situ powder X-ray diffraction (PXRD) methods and XPS. Two PXRD diffractograms from before and after sulfidation are shown (Fig. 2.7). Though few reflections have the requisite intensity to resolve, a clear reflection at 26 degrees appears in the MoO_{3-x} crystallite sample and is reduced in intensity following sulfidation.[23,24] Further, a new reflection appearing at 29 degrees is indicative of the (004) reflection plane in MoS_2.[25] The reduced intensity, yet still present, MoO_{3-x} specific peak and the appearance of a

MoS_2 specific peak reveal that this species was a partially sulfidated MoO_{3-x}/MoS_2 hybrid. X-ray photoelectron spectroscopy (XPS) shows that the reduced Mo oxide species has clear Mo (VI) 3d peaks and create Mo (IV) 3d peaks post sulfidation (Fig. 2.7). Additionally, the post sulfidated sample has a smaller intensity, but significant S 2p XPS signal. We did not observe residual Mo (VI) peaks indicative of the precursor Mo oxide.[26] However, this is unsurprising because XPS is a surface sensitive method and even though, as discussed later in this chapter, the sulfidation is preferred at the substrate – crystal interface, there is clear sulfidation occurring throughout the crystal, including at the surface, that is consistent with MoS_2 formation.[26,27]

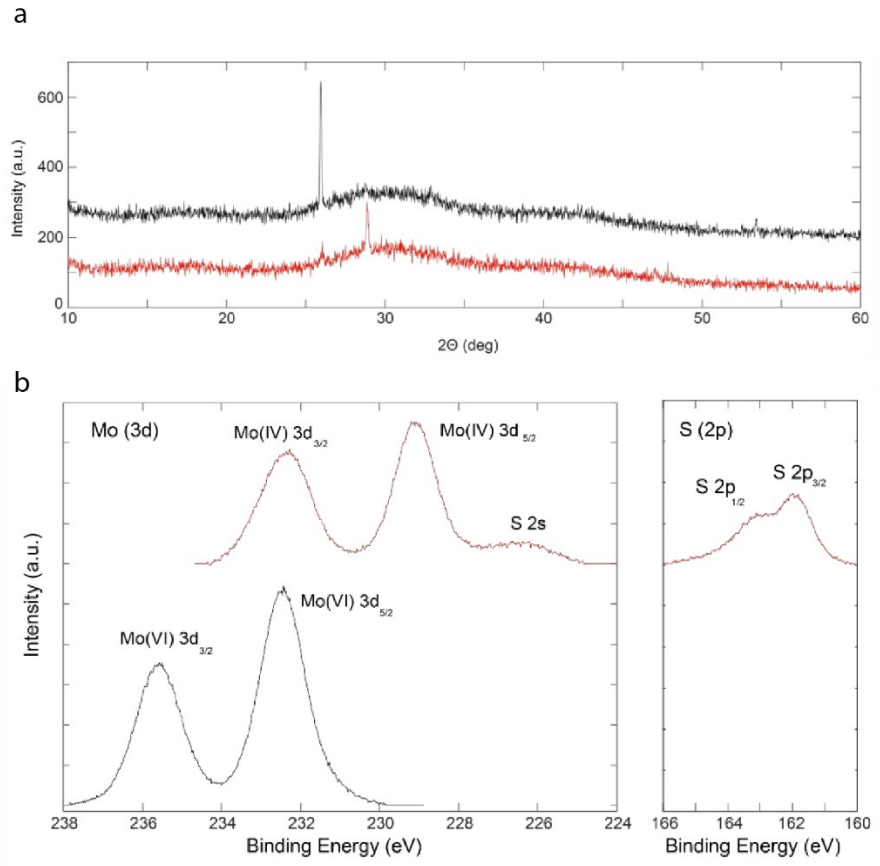

Figure 2.7. (a) Powder X-Ray diffractograms of MoO_{3-x} crystals before (black) and after (red) undergoing sulfidation. The reflection at 26 degrees is present in both samples and attenuated in the post sulfidation sample. A new reflection at 29 degrees is present indicative of MoS_2. (b) X-Ray photoelectron spectra of MoO_{3-x} crystals before (bottom) and after (top) sulfidation. The Mo (VI) 3d peaks are consistent with a Mo containing oxide and the appearance of Mo (IV) 3d peaks are consistent with the appearance of MoS_2.

Next, we turned to Raman spectroscopy to map out the partial or total conversion towards MoS_2 in single deposits of MoO_{3-x} (Fig. 2.8).

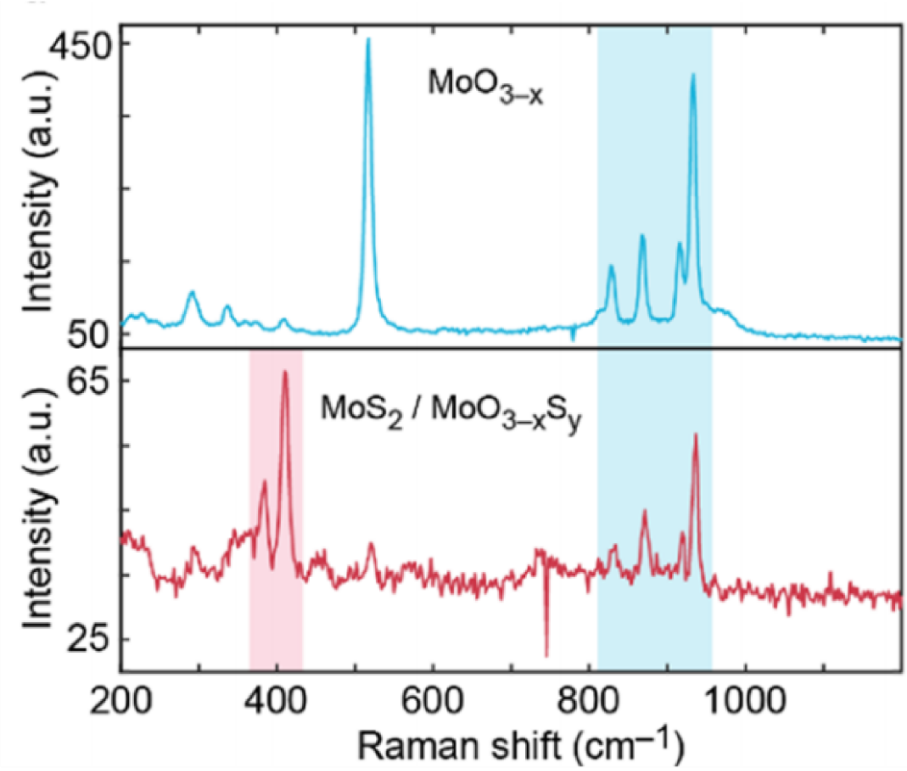

Figure 2.8. Raman spectra for both a pre sulfidated MoO_{3-x} crystals (top) and post sulfidated (bottom). Blue shading indicates Raman signatures that are indicative of MoO_{3-x} structure while the red shading indicates signatures indicative of MoS_2.

By utilizing marked substrates, we were able to track the evolution of Raman peak signatures of the same crystallite through its conversion from a partially reduced Mo oxide to a partially sulfo-oxide. Several features show that there is a partial conversion of the crystallites. First, there are three notable peaks at 831, 919, and 980 cm^{-1}, consistent with a partially reduced MoO_{3-x} moiety.[23,24,28–30] If the entire crystallite was sulfidated to form a bulk MoS_2 crystal we would expect to see the disappearance of these three peaks. However, what is notable is the reduction in intensity of these peaks and the emergence of the A_{1g} and E_{2g}

modes of MoS_2 located at 380 and 404 cm^{-1} respectively. This peak separation between these two modes is indicative of bulk MoS_2.[31–34] From this we can conclude that the sulfidation under these parameters causes some of the reduced oxide to form MoS_2 moieties, but not complete conversion of the entire crystallite towards MoS_2.

Further, we isolated the effects of both temporal and thermal effects on the overall chalcogenation of the reduced oxide, MoO_{3-x} on pathway to a MoO_{3-x}/MoS_2 hybrid.

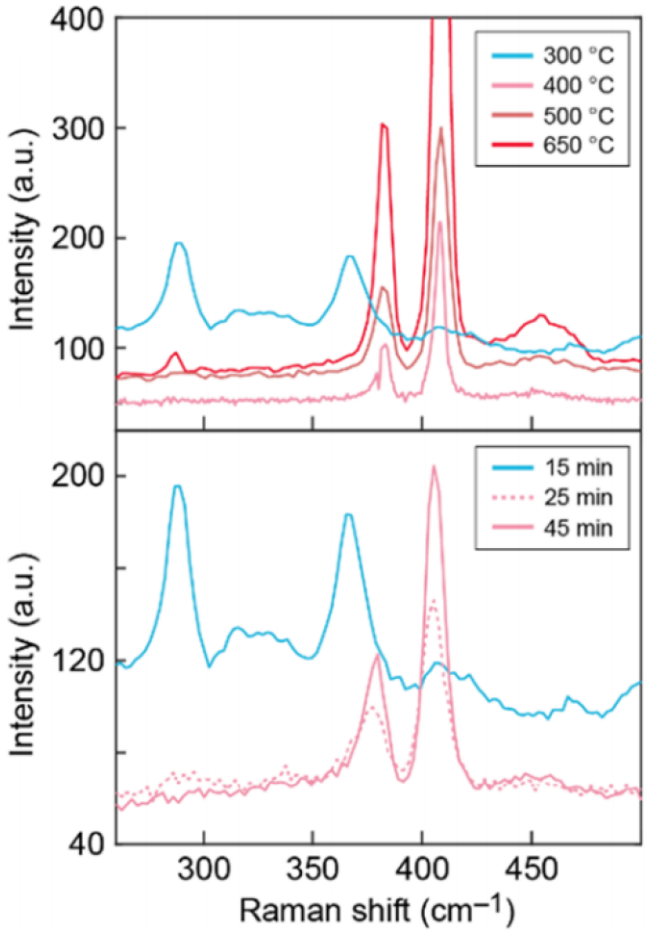

Figure 2.9. (Top) Raman spectra of MoO_{3-x} crystals following sulfidation carried out at four different temperatures over 15 minutes for each crystal. (Bottom) Raman spectra of MoO_{3-x} crystals following sulfidation carried out at the same temperature of 300 °C but utilizing different reaction times.

Raman spectra of MoO_{3-x} crystals after they have been exposed to sulfur vapor at times of 15, 25 and 45 min at a constant temperature of 300 °C and Raman spectra of MoO_{3-x} crystals after they have been exposed to sulfur vapor at a constant time of 15 min at 300, 400, 500 and 650 C° reveal several key features

about the two step synthetic process (Fig. 2.9). First, we see that under a constant temporal constraint, that at these low vacuum conditions partial conversion towards MoS_2 can commence at 400 °C. Going above 400 ° C towards conventional MoS_2 reaction temperatures of 650 °C or above starts to complete the chalcogenation process towards MoS_2.

Second, under a specific temperature of 300 °C as shown in Fig 2.9, we note that even lower temperatures are accessible to partial sulfidation of MoO_{3-x} crystals when reaction times were extended, showing that temporal considerations are considerable when dealing with the mechanism pathways of TMDs in the deconcerted pathway. Partial conversion proceeded down to ʒ00 ° C but not any lower even after 2 h duration of sulfidation at 200 °C, (Fig. 2.10).

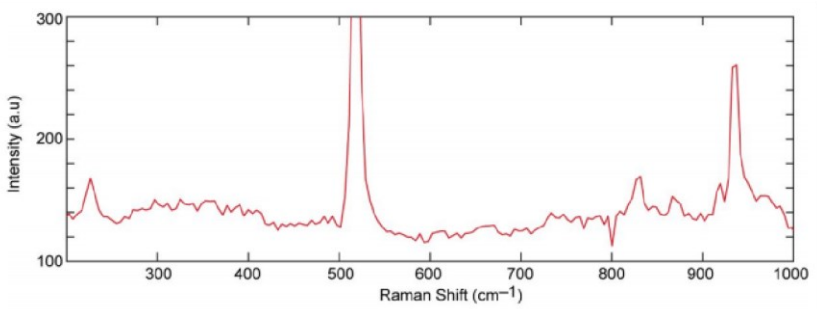

Figure 2.10. Raman spectrum of a MoO_{3-x} crystal that has been sulfidated at 200 °C for an extended time (2 h). There is no evidence of the A_{1g} or E_{2g} Raman bands expected to denote MoS_2 formation.

These data demonstrates that under these low-pressure conditions very limited chalcogenation reactions can proceed at low temperatures. As a large

number of TMD growths are done at atmospheric conditions, utilizing high vacuum conditions to couple to lower temperatures provides an avenue to isolating intermediates in the TMD synthetic process. Limited chalcogenation is a crucial ability to elucidate mechanistic insights from partially converted MoO_{3-x} as we seek to evaluate partially sulfidated moieties.

To confirm these trends, we also sought to completely convert a single crystallite of MoO_{3-x} towards a bulk MoS_2 crystal to confirm that the two-step pathway using reduced oxide precursors was both ideal and notable. A Raman spectrum of a MoO_{3-x} single crystallite that has been converted towards MoS_2 at 650 °C shows that there is little to no retention in MoO_{3-x} signal (Fig. 2.11). This temperature is a canonical temperature in the concerted synthesis of MoS_2. In this case, we notice that all high intensity, high wavenumber (800 – 1000 cm^{-1}) MoO_{3-x} Raman signatures have completely disappeared in the spectrum, indicating complete conversion towards MoS_2. These results concludes that the novel low pressure, low temperature technique employed here is a useful tool in isolating partially sulfidated intermediates to study reaction pathways in transition metal dichalcogenide materials.

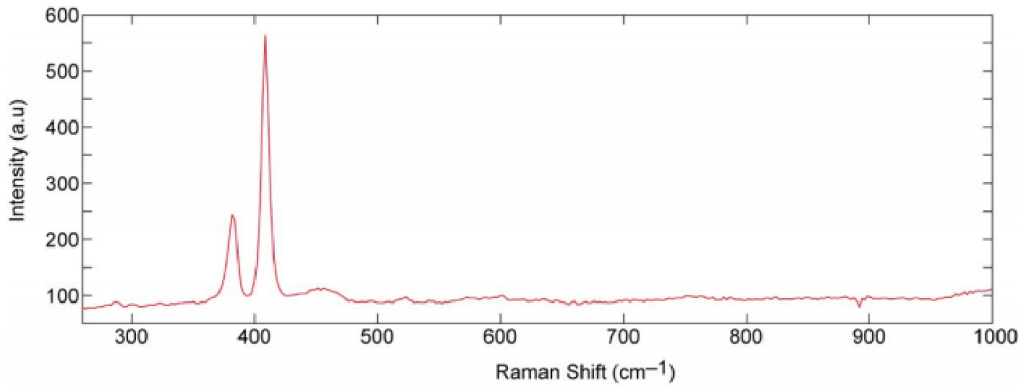

Figure 2.11. Raman spectrum of a MoO_{3-x} crystal that has been sulfidated at 650 °C for 15 min. There is no evidence of the Raman bands expected to indicate MoO_{3-x} formation. However, the A_{1g} and E_{2g} bands indicative of MoS_2 are present at high intensity indicating complete conversion to a bulk MoS_2 crystal.

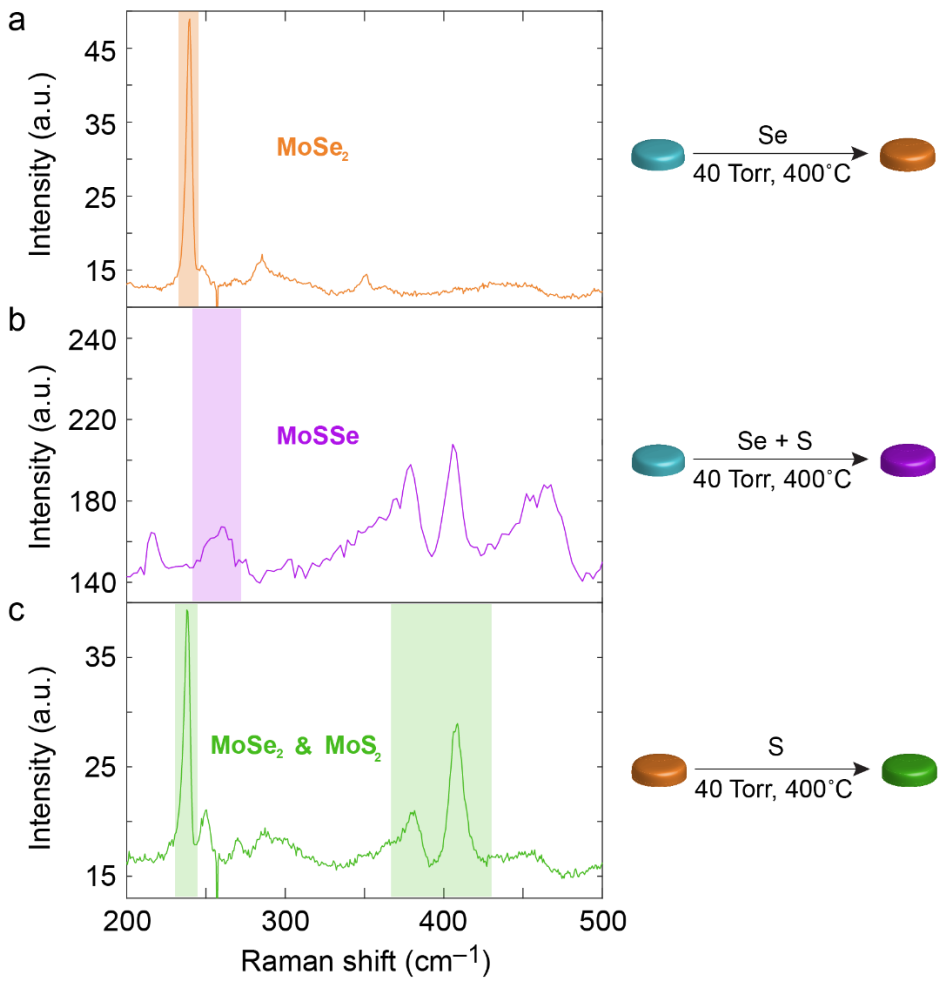

Figure 2.12. (a) Raman spectra of a MoO_{3-x} crystallite undergoing selenation in the presence of Se vapor. The indicative A_{1g} Raman band of $MoSe_2$ is present as denoted by the orange shading. (b) Raman spectrum of a MoO_{3-x} crystallite undergoing concurrent selenation and sulfidation in the presence of Se and S vapor. The A_{1g} Raman band of $MoSe_2$ is blue shifted to 262 cm^{-1} as denoted by the purple shading. (c) Raman spectrum of a MoO_{3-x} crystallite undergoing stepwise selenation then sulfidation. Indicative Raman bands for both $MoSe_2$ and MoS_2 are present as denoted by the green shading.

Further, Raman spectra for MoO_{3-x} deposits that have been both sulfidated, selenated, and a combination of the two at lower temperatures show several notable results (Fig. 2.12). As expected, the sulfidated and selenated

samples show characteristic Raman peaks of MoS_2 and $MoSe_2$ respectively. In Fig. 2.12 (a) we note the appearance of a clear $MoSe_2$ A_{1g} Raman mode. The location of those Raman mode at ~ 241 cm^{-1} is indicative of a $MoSe_2$ material as corroborated previously.[5,31,32,35–37] Interestingly, the co-chalcogenation at low temperatures and reduced pressures proceeded to form a MoSSe alloy as demonstrated by the $MoSe_2$ A_{1g} shifting from ~ 240 cm^{-1} to ~ 260 cm^{-1} and peak broadening significantly for the A_{1g} mode as demonstrated in previous MoSSe alloys.[38,39] Previous work has demonstrated numerous occasions that TMD reactions utilizing a litany of reactants can yield discrete heterostructures but reports of alloyed material are few.[40–42]

Taking these Raman data together, we determined that mild conditions (400 °C at during a 15 min hold time) would be ideal to isolate an intermediate sulfo-oxide species during a solid-vapor phase conversion. By isolating this partially sulfidated material we could investigate the extent of sulfidation. For this purpose, focused ion beam (FIB) SEM was utilized to take a cross-section of the crystallite shown and tracked in Fig. 2.5. Post sulfidation, this cross-sectioned deposit was used to measure the concentration of chalcogen species vertically throughout the crystal. Cross-sectional SEM and STEM mode micrographs of a cross-section generated from the FIB milled sample of a partially converted at 400 °C Mo_{3-x}/MoS_2 hybrid crystallite are shown (Fig. 2.13).

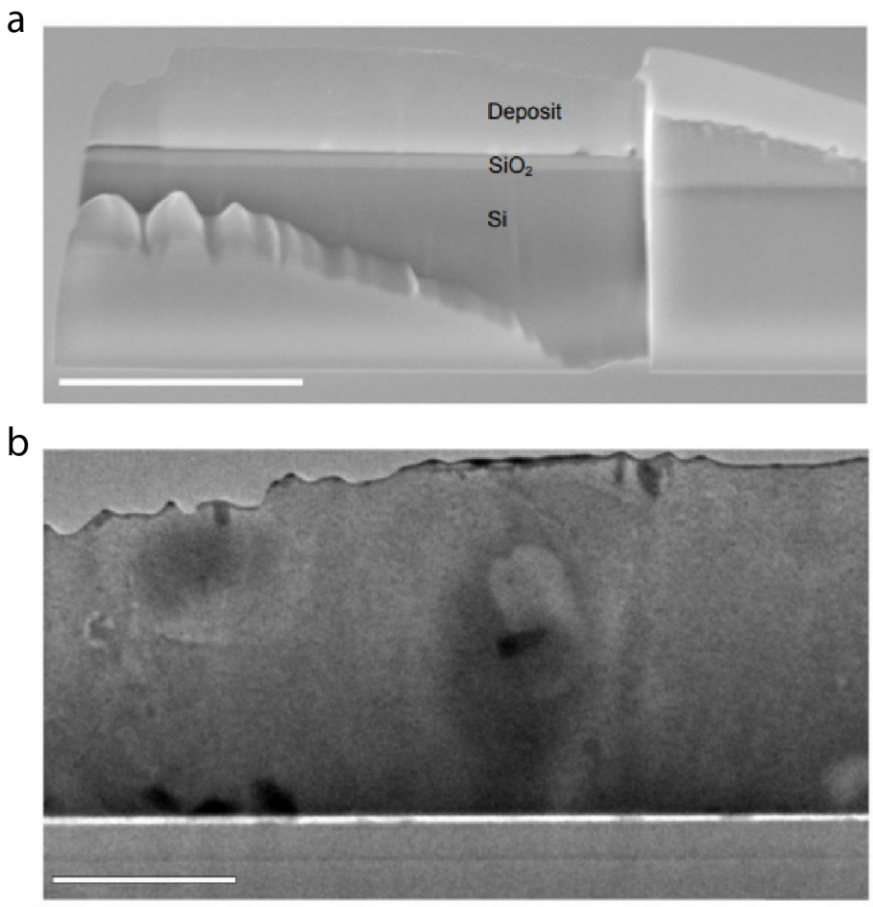

Figure 2.13. (a) Scanning electron micrograph depicting a MoO_{3-x} crystallite post sulfidation at 400 °C that has undergone focused ion beam (FIB) treatment to thin a cross section of the crystal. Scale bar 3 μm. (b) Transmission electron micrograph of the cross section of the same sulfidated MoO_{3-x} crystal. Scale bar, 1 μm.

In initial STEM measurements, we wanted to understand if the crystallinity of the partially chalcogenated crystal was retained through the reaction at these mild temperatures. To this end Fig. 2.14 shows a procession of SAED measurements taken vertically throughout the crystal showing that the crystal structure changes vertically throughout the crystal. Crucially, these data

demonstrate a crystalline species that has maintained its crystallinity during the chalcogenation reaction. Further, the diffractogram taken near the base of the crystal in Fig 2.14 shows a more hexagonal pattern. However, patterns at the middle and top of the crystal have more rectangular lattices, indicative of greater MoO_{3-x} character. We stress that the spots that any given selected area electron diffractograms are generated may have more or less MoS_2 character than its average content for a given distance through the crystal (Fig. 2.15). As can be seen in Fig. 2.14, there exist multiple occlusions that are most likely regions of unreacted oxide. These diffraction data is consistent with previous data on molybdenum oxides and MoS_2 diffraction, though we must note that the exact identity of the suboxide species is unknown at present and diffractograms may differ slightly from other MoO_{3-x} species due to different stoichiometries and further research into the nature of Mo sub-oxides and their characterization is needed.[43–51]

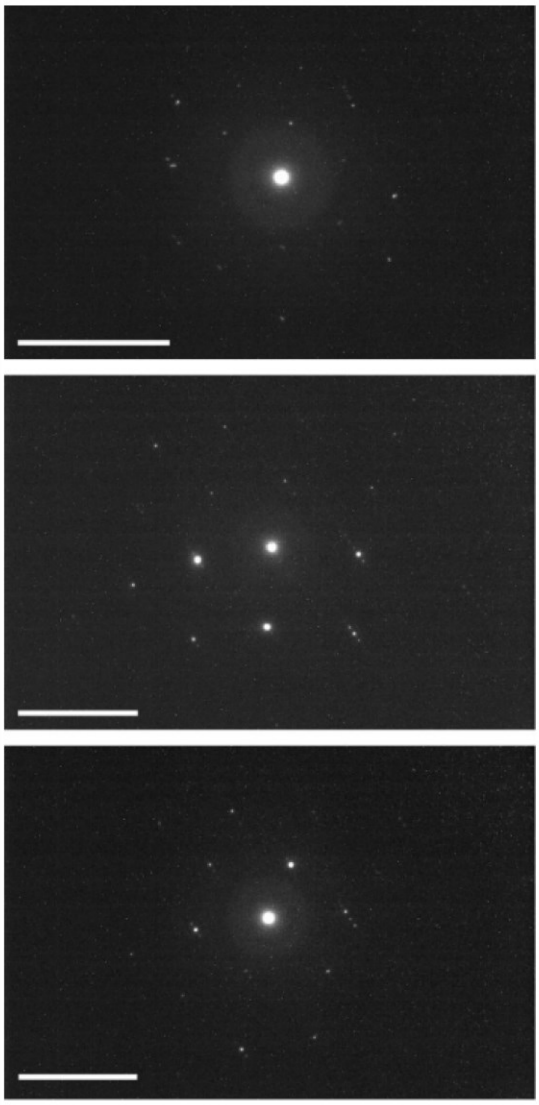

Figure 2.14. Selected area electron diffractograms (SAED) of the cross-section of the sulfidated MoO_{3-x} crystal shown in Fig. 2.13. The top diffractogram was taken at the top of the crystal near the atmosphere interface, the middle diffractogram at the middle third of the crystal and the bottom diffractogram at the base of the crystal near the substrate interface. Scale bars, 10 nm^{-1}.

Next, understanding how the sulfur atoms formed MoS_2 spatially during the reaction would be key in gaining insights into designing multi-step TMD synthesis steps that could reliably and quickly produce bottom-up grown

vertical heterostructures and interfacing with thermally sensitive materials. During the acquisition of STEM mapping micrographs such as those shown in Fig. 2.13, STEM-EDS data was taken to understand the chemical specificity as a function of distance through the crystal. These STEM EDS data demonstrates a spatial preference for chalcogenation in the crystal that had not been observed previously. (Fig. 2.15). We do note that it is clear from Fig. 2.13 that the FIB process thinned the crystal unevenly, where the top of the crystal is significantly thinner than the region closer to the substrate and data was normalized to account for this processing inconsistency.

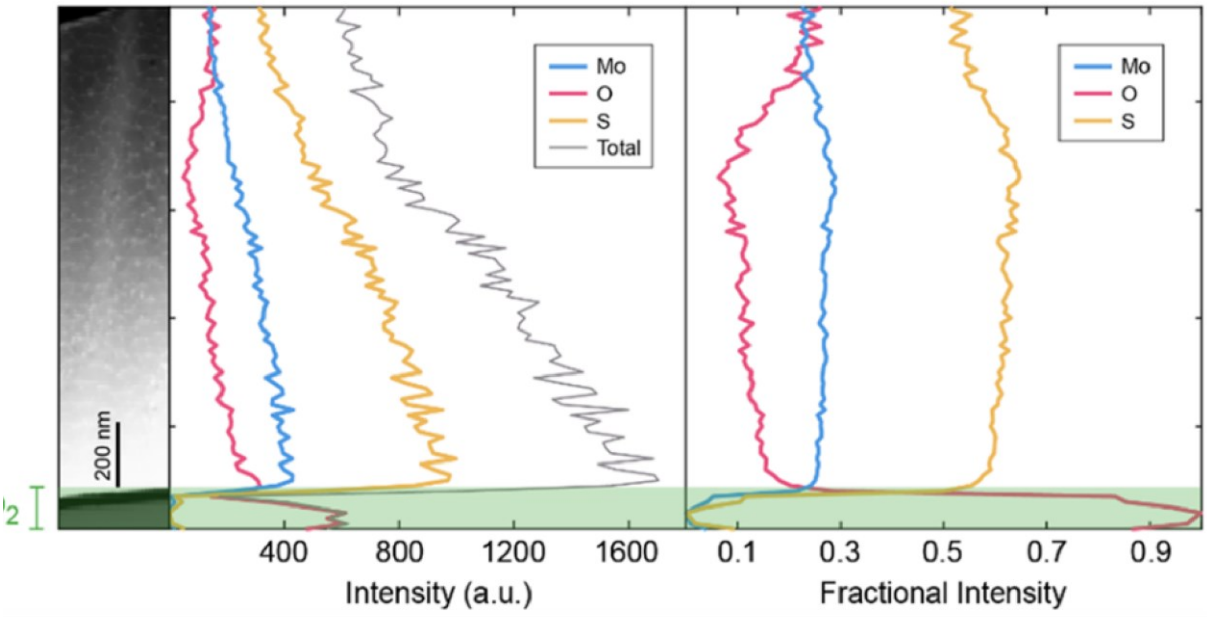

Figure 2.15. (a) STEM-HAADF image of the cross-section of the partially sulfidated MoO_{3-x} crystal shown in Fig. 2.5 and Fig. 2.13. (b) Line profiles of EDS counts for Mo, O, and S collected from the cross-section shown in (a). (c) Line profiles for Mo, O and S normalized as a function of the total intensity counts generated. The green shaded region is the approximate region of the SiO_2 substrate.

STEM-EDS measurements are shown where the y-axis is the direction vertically through the crystal where 0 is the substrate-crystal interface and the elemental trends shown in Fig. 2.15 (b and c) are correlated directly to the STEM-HAADF map adjoined to the plots in Fig. 2.15 (a). Key elements Si, O, Mo, and S were calculated by taking that element's intensity and finding its proportion of the overall intensity in the STEM-EDS map to account for any variability in

thickness throughout the crystal. We see several features that gleam clues into how sulfur interacts with a MoO_{3-x} crystal in Fig. 2.15. First, the S concentration is greater at the crystal-substrate interface than the crystal-air interface. This is surprising for several reasons. First the accessibility of gaseous S species into the crystal is lower for the crystal-substrate interface due to the diffusion required for S species to arrive at the interior of the crystal. We hypothesize that this bottom-up preference is derived from some lower energy requirement at the interface between crystal, atmosphere, and substrate located at the edge of the crystal. However, this remains an open question. Additionally, previous work on fullerene-like MoS_2 mechanism analysis shows a concentric sulfidation where the sulfur content is relatively even radially from the exterior and an oxide shell resides in the middle during a concerted MoS_2 growth that was done with fully oxidized precursors. However, this work clearly shows that there is not an even distribution of chalcogenation from bottom-up to top-down in this two-step process. By isolating a partially reduced intermediates on pathway to MoS_2 growth, this work demonstrates that in conjunction with the previously researched existence sulfo-oxide intermediates, that low-dimensional TMDs are most likely getting sulfidated from the bottom-up. Interestingly, this has great implications in the scalability and modularity of TMD crystals. For example, Janus TMDs have been the subject of much interest in recent years, but the

creation of these structures is extremely difficult. By exploiting more favorable reaction pathways on the crystal-substrate interaction it may be possible to construct complex mono- or few- layer heterostructures of TMDs. Future work probing reduced oxides as possessing amenable sites towards milder chalcogen replacement steps will be critical in advancing this synthetic approach. This work supports the need to investigate a much wider parameter space in oxide related TMD precursors that go beyond fully stoichiometric materials such as MoO_2 and MoO_3 and that these non-stoichiometric precursors may afford some advantages, namely reduced energy requirements towards TMD synthesis, that fully stoichiometric materials do not possess.

2.4 References

(1) Shi, J.; Ma, D.; Han, G.-F.; Zhang, Y.; Ji, Q.; Gao, T.; Sun, J.; Song, X.; Li, C.; Zhang, Y.; Lang, X.-Y.; Zhang, Y.; Liu, Z. Controllable Growth and Transfer of Monolayer MoS_2 on Au Foils and Its Potential Application in Hydrogen Evolution Reaction. *ACS Nano* **2014**, *8* (10), 10196–10204.

(2) Yu, Y.; Li, C.; Liu, Y.; Su, L.; Zhang, Y.; Cao, L. Controlled Scalable Synthesis of Uniform, High-Quality Monolayer and Few-Layer MoS_2 Films. *Sci. Rep.* **2013**, *3* (1), 1866.

(3) Zhang, Y.; Ji, Q.; Han, G.-F.; Ju, J.; Shi, J.; Ma, D.; Sun, J.; Zhang, Y.; Li, M.; Lang, X.-Y.; Zhang, Y.; Liu, Z. Dendritic, Transferable, Strictly Monolayer MoS_2 Flakes Synthesized on $SrTiO_3$ Single Crystals for Efficient Electrocatalytic Applications. *ACS Nano* **2014**, *8* (8), 8617–8624.

(4) Lin, Z.; Thee, M. T.; Elías, A. L.; Feng, S.; Zhou, C.; Fujisawa, K.; Perea-López, N.; Carozo, V.; Terrones, H.; Terrones, M. Facile Synthesis of MoS_2 and $Mo_xW_{1-x}S_2$ Triangular Monolayers. *APL Mater.* **2014**, *2* (9), 092514.

(5) Lu, X.; Utama, M. I. B.; Lin, J.; Gong, X.; Zhang, J.; Zhao, Y.; Pantelides, S. T.; Wang, J.; Dong, Z.; Liu, Z.; Zhou, W.; Xiong, Q. Large-Area Synthesis of Monolayer and Few-Layer $MoSe_2$ Films on SiO_2 Substrates. *Nano Lett.* **2014**, *14* (5), 2419–2425.

(6) Gong, Y.; Lin, Z.; Ye, G.; Shi, G.; Feng, S.; Lei, Y.; Elías, A. L.; Perea-Lopez, N.; Vajtai, R.; Terrones, H.; Liu, Z.; Terrones, M.; Ajayan, P. M. Tellurium-Assisted Low-Temperature Synthesis of MoS_2 and WS_2 Monolayers. *ACS Nano* **2015**, *9* (12), 11658–11666.

(7) Cun, H.; Macha, M.; Kim, H.; Liu, K.; Zhao, Y.; LaGrange, T.; Kis, A.; Radenovic, A. Wafer-Scale MOCVD Growth of Monolayer MoS_2 on Sapphire and SiO_2. *Nano Res.* **2019**, *12* (10), 2646–2652.

(8) Cwik, S.; Mitoraj, D.; Reyes, O. M.; Rogalla, D.; Peeters, D.; Kim, J.; Schütz, H. M.; Bock, C.; Beranek, R.; Devi, A. Direct Growth of MoS_2 and WS_2 Layers by Metal Organic Chemical Vapor Deposition. *Adv. Mater. Interfaces* **2018**, *5* (16), 1800140.

(9) Hofmann, W. K. Thin Films of Molybdenum and Tungsten Disulphides by Metal Organic Chemical Vapour Deposition. *J Mater Sci* **1988**, *23* (11), 3981–3986.

(10) Weber, Th.; Muijsers, J. C.; van Wolput, J. H. M. C.; Verhagen, C. P. J.; Niemantsverdriet, J. W. Basic Reaction Steps in the Sulfidation of Crystalline MoO_3 to MoS_2 , As Studied by X-Ray Photoelectron and Infrared Emission Spectroscopy. *J. Phys. Chem.* **1996**, *100* (33), 14144–14150.

(11) Endler, I.; Leonhardt, A.; König, U.; van den Berg, H.; Pitschke, W.; Sottke, V. Chemical Vapour Deposition of MoS_2 Coatings Using the Precursors $MoCl_5$ and H_2S. *Surf. Coat. Tech.* **1999**, *120–121*, 482–488.

(12) Kim, Y.; Bark, H.; Ryu, G. H.; Lee, Z.; Lee, C. Wafer-Scale Monolayer MoS_2 grown by Chemical Vapor Deposition Using a Reaction of MoO_3 and H_2S. *J. Phys.: Condens. Matter* **2016**, *28* (18), 184002.

(13) Dumcenco, D.; Ovchinnikov, D.; Sanchez, O. L.; Gillet, P.; Alexander, D. T. L.; Lazar, S.; Radenovic, A.; Kis, A. Large-Area MoS_2 Grown Using H_2S as the Sulphur Source. *2D Mater.* **2015**, *2* (4), 044005.
(14) Cain, J. D.; Shi, F.; Wu, J.; Dravid, V. P. Growth Mechanism of Transition Metal Dichalcogenide Monolayers: The Role of Self-Seeding Fullerene Nuclei. *ACS Nano* **2016**, *10* (5), 5440–5445.
(15) Zhu, D.; Shu, H.; Jiang, F.; Lv, D.; Asokan, V.; Omar, O.; Yuan, J.; Zhang, Z.; Jin, C. Capture the Growth Kinetics of CVD Growth of Two-Dimensional MoS_2. *npj 2D Mater. Appl.* **2017**, *1* (1), 1–8.
(16) Hong, S.; Krishnamoorthy, A.; Rajak, P.; Tiwari, S.; Misawa, M.; Shimojo, F.; Kalia, R. K.; Nakano, A.; Vashishta, P. Computational Synthesis of MoS_2 Layers by Reactive Molecular Dynamics Simulations: Initial Sulfidation of MoO_3 Surfaces. *Nano Lett.* **2017**, *17* (8), 4866–4872.
(17) Hong, S.; Tiwari, S.; Krishnamoorthy, A.; Nomura, K.; Sheng, C.; Kalia, R. K.; Nakano, A.; Shimojo, F.; Vashishta, P. Sulfurization of MoO_3 in the Chemical Vapor Deposition Synthesis of MoS_2 Enhanced by an H_2S/H_2 Mixture. *J. Phys. Chem. Lett.* **2021**, *12* (7), 1997–2003.
(18) Li, D.; Xiao, Z.; Mu, S.; Wang, F.; Liu, Y.; Song, J.; Huang, X.; Jiang, L.; Xiao, J.; Liu, L.; Ducharme, S.; Cui, B.; Hong, X.; Jiang, L.; Silvain, J.-F.; Lu, Y. A Facile Space-Confined Solid-Phase Sulfurization Strategy for Growth of High-Quality Ultrathin Molybdenum Disulfide Single Crystals. *Nano Lett.* **2018**, *18* (3), 2021–2032.
(19) Lin, Y.-C.; Zhang, W.; Huang, J.-K.; Liu, K.-K.; Lee, Y.-H.; Liang, C.-T.; Chu, C.-W.; Li, L.-J. Wafer-Scale MoS2 Thin Layers Prepared by MoO_3 Sulfurization. *Nanoscale* **2012**, *4* (20), 6637–6641.
(20) Taheri, P.; Wang, J.; Xing, H.; Destino, J. F.; Arik, M. M.; Zhao, C.; Kang, K.; Blizzard, B.; Zhang, L.; Zhao, P.; Huang, S.; Yang, S.; Bright, F. V.; Cerne, J.; Zeng, H. Growth Mechanism of Largescale MoS_2 monolayer by Sulfurization of MoO_3 film. *Mater. Res. Express* **2016**, *3* (7), 075009.
(21) Sajedi-Moghaddam, A.; Saievar-Iranizad, E.; Pumera, M. Two-Dimensional Transition Metal Dichalcogenide/Conducting Polymer Composites: Synthesis and Applications. *Nanoscale* **2017**, *9* (24), 8052–8065.
(22) Jeong, Y.; Park, J. H.; Ahn, J.; Lim, J. Y.; Kim, E.; Im, S. 2D $MoSe_2$ Transistor with Polymer-Brush/Channel Interface. *Adv. Mater. Interfaces* **2018**, *5* (19), 1800812.
(23) Dieterle, M.; Mestl, G. Raman Spectroscopy of Molybdenum Oxides. *Phys. Chem. Chem. Phys.* **2002**, *4* (5), 822–826.
(24) Pham, D. V.; Patil, R. A.; Lin, J.-H.; Lai, C.-C.; Liou, Y.; Ma, Y.-R. Doping-Free Bandgap Tuning in One-Dimensional Magnéli-Phase Nanorods of Mo_4O_{11}. *Nanoscale* **2016**, *8* (10), 5559–5566.
(25) Shokhen, V.; Miroshnikov, Y.; Gershinsky, G.; Gotlib, N.; Stern, C.; Naveh, D.; Zitoun, D. On the Impact of Vertical Alignment of MoS_2 for Efficient Lithium Storage. *Sci. Rep.* **2017**, *7* (1), 3280.

(26) Chen, Z.; Cummins, D.; Reinecke, B. N.; Clark, E.; Sunkara, M. K.; Jaramillo, T. F. Core–Shell MoO_3 –MoS_2 Nanowires for Hydrogen Evolution: A Functional Design for Electrocatalytic Materials. *Nano Lett.* **2011**, *11* (10), 4168–4175.
(27) Kim, I. S.; Sangwan, V. K.; Jariwala, D.; Wood, J. D.; Park, S.; Chen, K.-S.; Shi, F.; Ruiz-Zepeda, F.; Ponce, A.; Jose-Yacaman, M.; Dravid, V. P.; Marks, T. J.; Hersam, M. C.; Lauhon, L. J. Influence of Stoichiometry on the Optical and Electrical Properties of Chemical Vapor Deposition Derived MoS_2. *ACS Nano* **2014**, *8* (10), 10551–10558.
(28) Borovšak, M.; Šutar, P.; Goreshnik, E.; Mihailovic, D. Topotactic Changes on η-Mo_4O_{11} Caused by Biased Atomic Force Microscope Tip and Cw-Laser. *Appl. Surf. Sci.* **2015**, *354*, 256–259.
(29) Ou, J. Z.; Campbell, J. L.; Yao, D.; Wlodarski, W.; Kalantar-zadeh, K. In Situ Raman Spectroscopy of H_2 Gas Interaction with Layered MoO_3. *J. Phys. Chem. C* **2011**, *115* (21), 10757–10763.
(30) Seguin, L.; Figlarz, M.; Cavagnat, R.; Lassègues, J.-C. Infrared and Raman Spectra of MoO_3 Molybdenum Trioxides and $MoO_3{\cdot}XH_2O$ Molybdenum Trioxide Hydrates. *Spectrochim. Acta A* **1995**, *51* (8), 1323–1344.
(31) Chen, S.-Y.; Zheng, C.; Fuhrer, M. S.; Yan, J. Helicity-Resolved Raman Scattering of MoS_2 , $MoSe_2$, WS_2 , and WSe_2 Atomic Layers. *Nano Lett.* **2015**, *15* (4), 2526–2532.
(32) Tonndorf, P.; Schmidt, R.; Böttger, P.; Zhang, X.; Börner, J.; Liebig, A.; Albrecht, M.; Kloc, C.; Gordan, O.; Zahn, D. R. T.; Vasconcellos, S. M. de; Bratschitsch, R. Photoluminescence Emission and Raman Response of Monolayer MoS_2, $MoSe_2$, and WSe_2. *Opt. Express, OE* **2013**, *21* (4), 4908–4916.
(33) Zhang, X.; Han, W. P.; Wu, J. B.; Milana, S.; Lu, Y.; Li, Q. Q.; Ferrari, A. C.; Tan, P. H. Raman Spectroscopy of Shear and Layer Breathing Modes in Multilayer MoS_2 *Phys. Rev. B* **2013**, *87* (11), 115413.
(34) Li, H.; Zhang, Q.; Yap, C.; Tay, B.; Edwin, T.; Oliver, A.; Baillargeat, D. From Bulk to Monolayer MoS2: Evolution of Raman Scattering Adv. Funct. Mater. 2012, 22 (7), 1385-1390
(35) Nam, D.; Lee, J.-U.; Cheong, H. Excitation Energy Dependent Raman Spectrum of $MoSe_2$. *Sci. Rep.* **2015**, *5* (1), 17113.
(36) Zhang, X.; Sun, D.; Li, Y.; Lee, G.-H.; Cui, X.; Chenet, D.; You, Y.; Heinz, T. F.; Hone, J. C. Measurement of Lateral and Interfacial Thermal Conductivity of Single- and Bilayer MoS_2 and $MoSe_2$ Using Refined Optothermal Raman Technique. *ACS Appl. Mater. Interfaces* **2015**, *7* (46), 25923–25929.
(37) Late, D. J.; Shirodkar, S. N.; Waghmare, U. V.; Dravid, V. P.; Rao, C. N. R. Thermal Expansion, Anharmonicity and Temperature-Dependent Raman Spectra of Single- and Few-Layer $MoSe_2$ and WSe_2. *ChemPhysChem* **2014**, *15* (8), 1592–1598.
(38) Li, H.; Duan, X.; Wu, X.; Zhuang, X.; Zhou, H.; Zhang, Q.; Zhu, X.; Hu, W.; Ren, P.; Guo, P.; Ma, L.; Fan, X.; Wang, X.; Xu, J.; Pan, A.; Duan, X. Growth of Alloy $MoS_{2x}Se_{2(1-x)}$ Nanosheets with Fully Tunable Chemical Compositions and Optical Properties. *J. Am. Chem. Soc.* **2014**, *136* (10), 3756–3759.
(39) Zhou, H.; Yu, F.; Huang, Y.; Sun, J.; Zhu, Z.; Nielsen, R. J.; He, R.; Bao, J.; Goddard Iii, W. A.; Chen, S.; Ren, Z. Efficient Hydrogen Evolution by Ternary

Molybdenum Sulfoselenide Particles on Self-Standing Porous Nickel Diselenide Foam. *Nat. Commun.* **2016**, *7* (1), 12765.
(40) Wang, H.; Liu, F.; Fu, W.; Fang, Z.; Zhou, W.; Liu, Z. Two-Dimensional Heterostructures: Fabrication, Characterization, and Application. *Nanoscale* **2014**, *6* (21), 12250–12272.
(41) Li, M.-Y.; Chen, C.-H.; Shi, Y.; Li, L.-J. Heterostructures Based on Two-Dimensional Layered Materials and Their Potential Applications. *Mater. Today* **2016**, *19* (6), 322–335.
(42) Geim, A. K.; Grigorieva, I. V. Van der Waals heterostructures *Nature* **2013** *499*, 419-425
(43) Zhang, G.; Xiong, T.; Yan, M.; He, L.; Liao, X.; He, C.; Yin, C.; Zhang, H.; Mai, L. α-MoO_{3-x} by Plasma Etching with Improved Capacity and Stabilized Structure for Lithium Storage. *Nano Energy* **2018**, *49*, 555–563.
(44) Lee, Y.-H.; Zhang, X.-Q.; Zhang, W.; Chang, M.-T.; Lin, C.-T.; Chang, K.-D.; Yu, Y.-C.; Wang, J. T.-W.; Chang, C.-S.; Li, L.-J.; Lin, T.-W. Synthesis of Large-Area MoS_2 Atomic Layers with Chemical Vapor Deposition. *Adv. Mater.* **2012**, *24* (17), 2320–2325.
(45) Park, J.; Kim, J.-S.; Park, J.-W.; Nam, T.-H.; Kim, K.-W.; Ahn, J.-H.; Wang, G.; Ahn, H.-J. Discharge Mechanism of MoS_2 for Sodium Ion Battery: Electrochemical Measurements and Characterization. *Electrochim. Acta* **2013**, *92*, 427–432.
(46) Liu, K.-K.; Zhang, W.; Lee, Y.-H.; Lin, Y.-C.; Chang, M.-T.; Su, C.-Y.; Chang, C.-S.; Li, H.; Shi, Y.; Zhang, H.; Lai, C.-S.; Li, L.-J. Growth of Large-Area and Highly Crystalline MoS_2 Thin Layers on Insulating Substrates. *Nano Lett.* **2012**, *12* (3), 1538–1544.
(47) Desai, N.; Mali, S. Chemically Grown MoO_3 Nanorods for Antibacterial Activity Study. *J. Nanomed. Nanotechnol.* **2015**, *06*:6
mrung, A.; Thongtem, T.; Thongtem, S. Characterization of Orthorhombic α-MoO_3 Microplates Produced by a Microwave Plasma Process. *J. Nanomater.* **2012**, *2012*, e930763.
(49) Wang, S.; Zhang, Y.; Ma, X.; Wang, W.; Li, X.; Zhang, Z.; Qian, Y. Hydrothermal Route to Single Crystalline α-MoO_3 Nanobelts and Hierarchical Structures. *Solid State Commun.* **2005**, *136* (5), 283–287.
(50) Yang, J.; Xiao, X.; Chen, P.; Zhu, K.; Cheng, K.; Ye, K.; Wang, G.; Cao, D.; Yan, J. Creating oxygen-vacancies in MoO_{3-x} nanobelts toward high volumetric energy-density asymmetric supercapacitors with long lifespan *Nano Energy* **2019**, *58*, 455-465
(51) Xiao, X.; Peng, Z.; Chen, C.; Zhang, C.; Beidaghi, M.; Yang, Z.; Wu, N.; Huang, Y.; Miao, L.; Gogotsi, Y.; Zhou, J. Freestanding MoO_{3-x} nanobelt/carbon nanotube films for Li-ion intercalation pseudocapacitors *Nano Energy* **2014**, *9*, 355-363

Chapter 3: Substrate Mediated Manipulation of TMD Dimensionality

The work presented in this chapter has been published as:

T. Chowdhury, J. Kim, E. C. Sadler, C. Li, S.-W. Lee, K. Jo, W. Xu, D. H. Gracias, N. V. Drichko, D. Jariwala, T. H. Brintlinger, T. Mueller, H.-G. Park, and T. J. Kempa. "Substrate-Directed Synthesis of MoS_2 nanocrystals with Tunable Dimensionality and Optical Properties"

Nat. Nanotechnol. **15**, 29-34 (2020)

3.1 Introduction

Though the majority of attention in atomically thin low-dimensional materials, such as TMDs, has been focused on two-dimensional variants, these materials have been explored in other morphologies, notably one-dimensional (1D) counterparts, as has been explored in recent reviews.[1–3] These 1D materials exploit their confined dimensionality in an additional dimension compared to 2D materials. 1D morphologies include nanoribbons, nanotubes, and nanowires.[4–8] The reduced dimensionality in 1D materials evokes new phenomena and properties such as a completely different band structures, greater edge

dominated properties, width-dependent properties, and greater confinement effects.[9–19] For example, graphene has been widely explored in the form of carbon nanotubes (CNTs) and graphene nanoribbons (GNRs) with each possessing a wide variety of different properties from each other and their parent 2D graphene. CNTs are mechanically extremely promising, boasting exceptional tensile strengths over 60 GPa. Additionally they are metallic or semiconducting in nature, and have excellent thermal conductivity compared to 2D graphene and have been utilized for their surface functionalization modulation which imparts sensing and catalytic benefits.[20–24] GNRs exhibit exotic edge properties where edges modify the electronic, mechanical, and optical properties of GNRs and influence their applications.[18,19,25–27] The increased contribution of edges to the overall physical characteristics of GNRs compared to 2D graphene stems from the increased edge to basal plane ratios in planar 1D materials and greater confinement effects. Further understanding carbon and other compositionally based 1D materials is crucial for the development of next generation 1D morphologies and continuing work has focused on the advanced synthesis of these materials. Notably, the edge character of GNRs can be influenced readily from bottom-up synthetic methods.[18,25,28] There are currently a number of bottom-up methods for creating and modifying 1D carbon-based materials. Additionally, top-down methods such as ion beams, electron beams, and microprobes to

manually etch or carve out one-dimensional regions from two-dimensional materials have been used in the creation of 1D moieties.[29] These methods can induce large modulation in material morphology and edge states in an array of materials including carbon based low dimensional materials and TMDs, at the cost of synthetic time and scale.

Beyond carbon-based 1D materials there are several prime candidates that have seen extensive research including semiconductor nanowires. Canonical in these materials are Si nanowires grown from vapor-liquid-solid (VLS) methods.[30–32] These have been used as biological sensors and in nano-electronic applications.[33–35] Cousins of these Si based VLS materials are III-V semiconductor nanowires such as GaAs and have been used extensively in solar cell and other applications such as lasing and photodetectors.[36–38] The tunability of these semiconductor nanowires are versatile and useful. For example, radial heterostructuring can be done by utilizing vapor- solid-solid (VSS) growth to deposit material cocentrically.[39–42] The interfacial regions of the 1D nanowires then can afford new interactions. Axially, synthetic tuning of input gases in the CVD processes during VLS growth effectively changes the growth front material and can create sharp heterointerfaces along their length.[43–45]

Beyond semiconductor nanowires, transition metal dichalcogenides (TMDs) also exist in nanotube and nanoribbon morphologies. TMD nanotubes

have been synthesized through solution phase methods like their CNT carbon counterparts. TMD nanotubes have been used in electronic applications such as field effect transistors and photovoltaics.[7,8,46–49] However, the number of reports regarding TMD nanotubes pales in comparison to the wide array of reports on CNTs demonstrating that TMD nanotubes present opportunities to discover new physical phenomena.

However, the work presented in this chapter and the following two chapters do not discuss nanotube morphologies. In this work we look to TMD nanoribbons as an attractive one-dimensional platform to uncover new phenomenological properties. TMD nanoribbons have been a growing class of materials over the last several years with the general commensurate rise of new morphologies beyond 2D. TMD nanoribbons in particular have generated much interest due to their myriad useful physical properties, such as optical anisotropy, catalytic uses, high mobilities, and magnetic and electron phenomena at their edges.[11,50–55] Though these materials present extremely promising platforms to study a rich area of chemistry and physics, existing methods towards synthesizing these nanoribbons have been inadequate. Like their counterparts of graphene nanoribbons, TMD nanoribbons require a more careful synthetic procedure than nanotubes. Currently, most 1D nanoribbon TMD morphologies are synthesized from top-down probe techniques similarly to

GNRs utilizing techniques such as STM, AFM, ion beams, and electron beams (Fig. 3.1).[25,29,56–65]

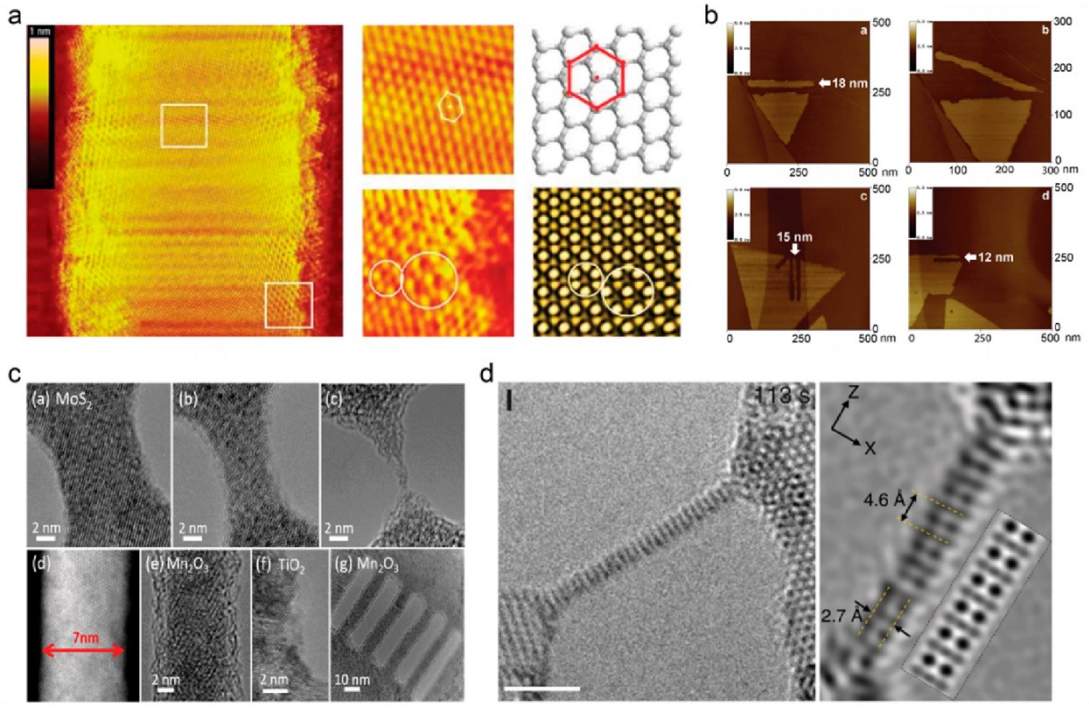

Figure 3.1. (a) Scanning tunneling micrographs (STM) of graphene nanoribbons that have been tailored through scanning probe techniques.[29] (b) STM micrographs of 1D MoS_2 regions carved out of a 2D MoS_2 flake by scanning probes.[63] (c) Transmission electron micrographs (TEM) of materials including MoS_2 thinned through He^+ ion milling.[64] (d) TEM micrographs of a MoS_2 flake thinned down to a 1D moiety through electron beam irradiation.[65]

However, the edge quality, which imparts many of the phenomenological properties of 1D materials, is quite poor when utilizing these methods and instrumentation requirements along with the serial nature of top-down patterning limit the scalability and overall effectiveness of top-down methods.

Due to this material edge breakdown and instrument limitations, there has been increasing focus on bottom-up methods that can produce high quality single crystal nanoribbons of TMDs.. Recently, a VLS method, similar to group IV and group III-IV semiconductor nanowires methods, was utilized to grow TMD nanoribbons from a chalcogen infused droplet composed of a Na and MoO_3 melt (Fig. 3.2).[66] Unfortunately, the disparity in quality between various nanoribbons and the lack of high-quality edge fidelity limits the scalability of this method. However, this was a great step towards scalable bottom up TMD nanoribbon growth. Additionally, it has been seen that by utilizing native crystal planes, such as within sapphire crystals, can influence the dimensionality of MoS_2 crystals between 2D and 1D moieties.[67,68] Again, this method using native surface interactions suffers from lack of tunability and has not shown the ability to reach critical widths that engender physical phenomena of interest. Other methods such as MBE growth of ultranarrow TMD nanoribbons have been utilized as discussed in the next chapter. These methods suffer from the need for complex instrumentation and generally serial nature of their synthesis, and long development times.

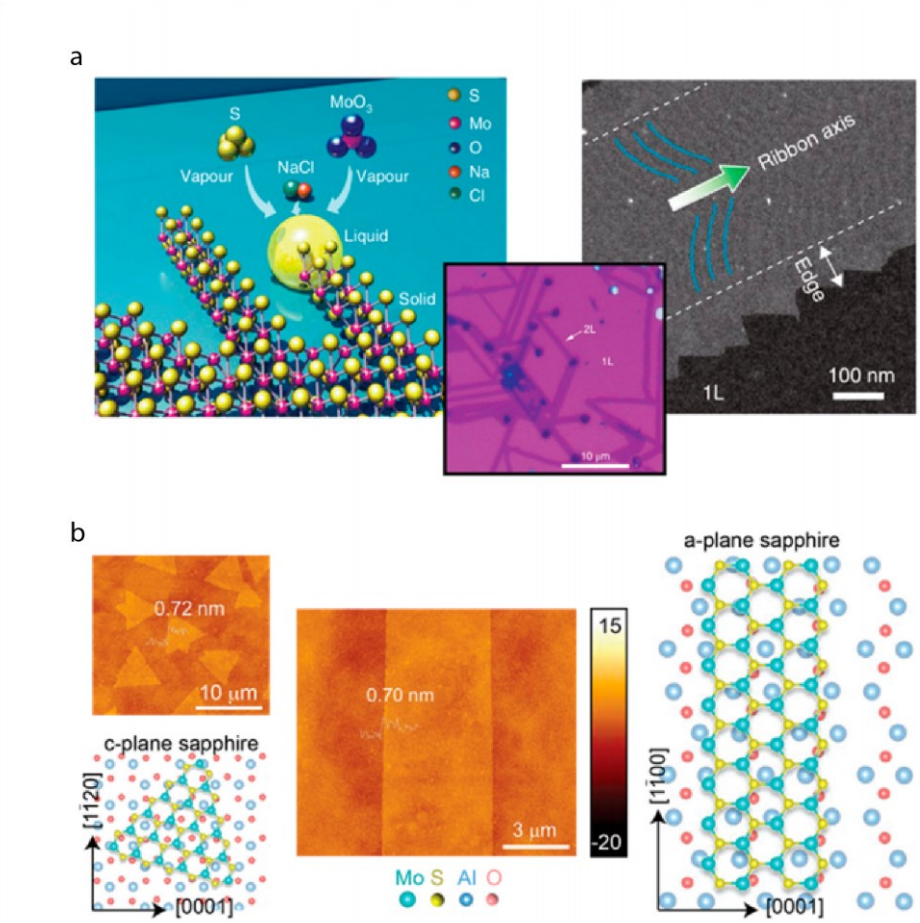

Figure 3.2. (a) Schematic of vapor-liquid-solid (VLS) process to extrude 1D MoS_2 nanoribbons. Optical micrograph and electron micrograph showing nanoribbons formed from the VLS method.[66] (b)Atomic force micrographs showing both 2D and 1D domains grown on different planes of sapphire with structures of the a- and c-planes of sapphire shown as ball and stick models.[68]

The manipulation of morphology in TMDs has been less explored than the manipulation of the composition, phase, and edges of 2D TMDs, on which subject there have been numerous reports.[62,63,69,70] All of these transformations allow 2D TMDs to be better exploited for a variety of applications including

catalysis, optoelectronics, and quantum information systems. However, the modification of the lateral dimension in 2D TMDs is a research area that requires further investigation. With the work presented here, more avenues towards reliable bottom-up synthesis of TMD nanoribbons will allow the continued expansion of modularity of composition, phase, and edge structures towards wide ranging applications in conjunction with reduced dimensionality which will aide in exploiting the desired phenomena.

The Kempa group has pioneered a novel strategy to generate prescribed surfaces that can direct the anisotropic growth of TMD crystals significantly enough to influence their physical properties. . A scheme of this process compared to the traditional 2D TMD growth process is shown (Fig. 3.3).

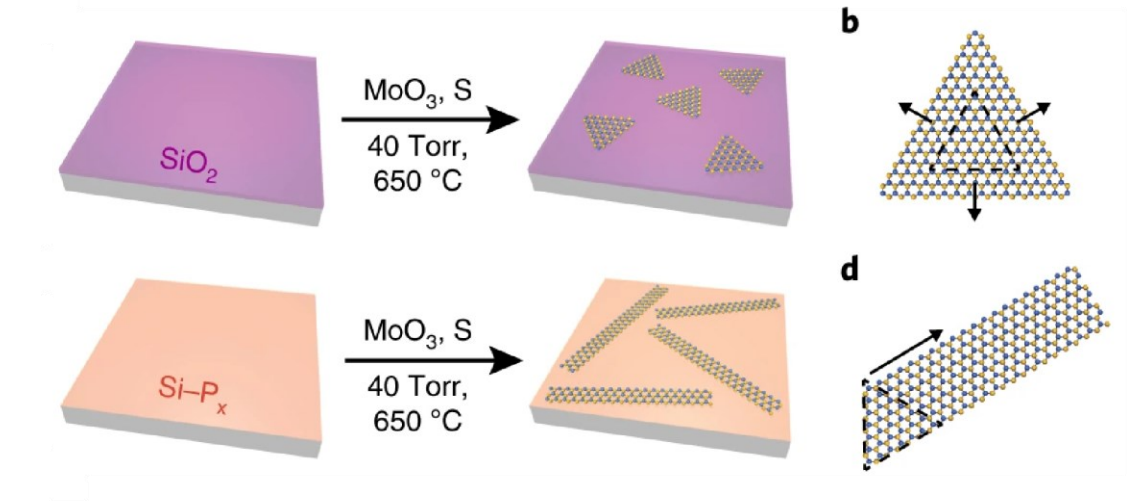

Figure 3.3. Scheme depicting two separate reactions to create both 2D and 1D TMD moieties. (a) Chemical vapor deposition reaction of MoO_3 and S powders utilizing a SiO_2 surface yielding isotropic 2D domains. (b) Chemical vapor deposition reaction of MoO_3 and S powders utilizing a novel Si-P_x surface yielding anisotropic 1D domains.

In this novel synthesis, a Si-P_x surface is generated from the reaction of PH_3 gas with a H-terminated Si(001) surface. This substrate then forms the nominal Si-P_x substrate. This Si-P_x substrate undergoes the same reaction conditions as the canonical 2D TMD growths, but due to the now prescribed surface, is directed into a one-dimensional nanoribbon morphology instead of the isotropically grown 2D TMD triangular morphological sheet as seen normally. The reduced dimensionality resulting from the directed growth has demonstrated critical changes in their physical properties which will be

discussed in chapter 5. In this chapter, we will discuss hypotheses about how the synthetic growth modes proceed and how the concentration of Si-P_x influence control over the dimensionality of the nanoribbons.

3.2 Experimental Methods

Our home-built CVD system is a versatile quartz tube hot-wall reactor design with a manifold of mass flow controllers (MKS Instruments, GM50A series MFCs) and a closed-loop pressure control system (MKS Instruments, 640B pressure controller) (Fig. 3.4).

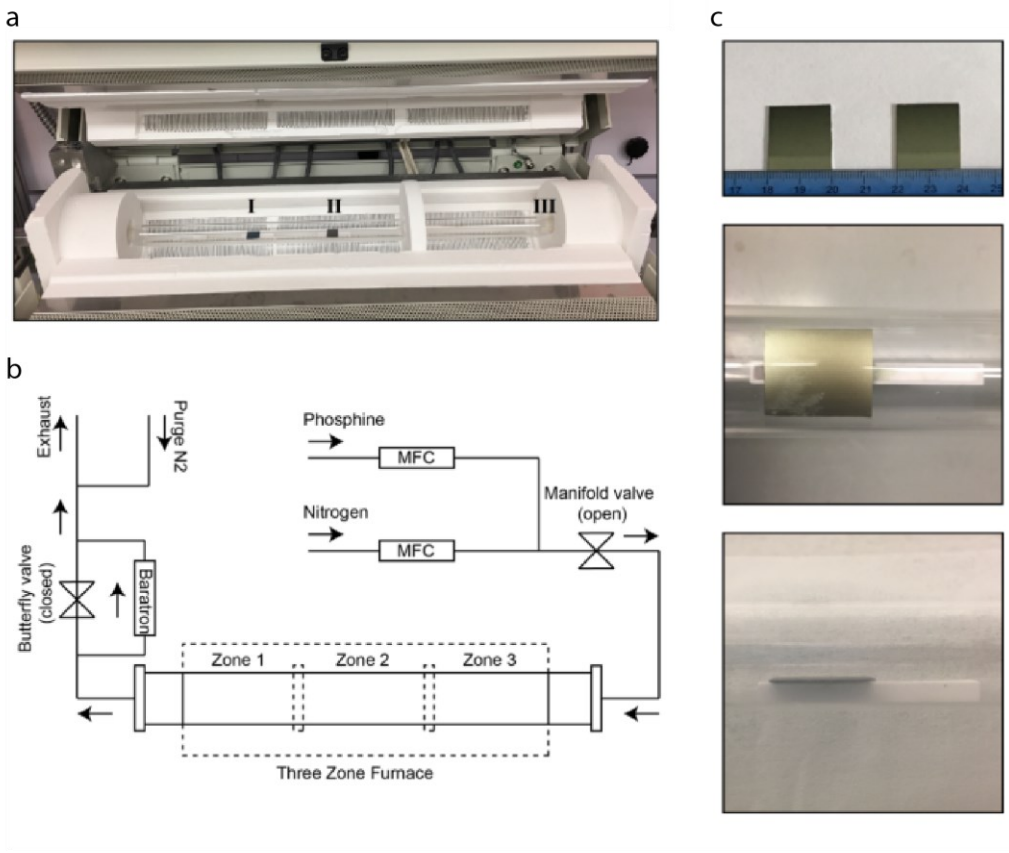

Figure 3.4. (a) Photograph of custom-built three zone chemical vapor deposition instrument housing substrates for growth of MoS_2 nanoribbons. (b) Schematic depicting the hot-wall CVD system utilizing a mass flow controller (MFC) manifold and closed-loop pressure control circuit. (c) Substrates before growth and substrates positioned face-down on ceramic boats for TMD growth.

The manifold and pressure control circuit are both operated through custom LabView scripts running on a personal computer. The furnace (Thermo Scientific, Lindberg Blue M Three-Zone) has three independently controllable zones, each of which measures 25 cm in length and can reach temperatures of

1,200 °C. A 400 °C temperature differential setpoint can be applied between adjacent zones through the use of thermal inserts (Fig. 3.4). A high-vacuum pump (Leybold, LV80 screw pump) is used to evacuate our CVD system to a base pressure of 0.01 mtorr and is able safely to manage toxic and pyrophoric effluent. The metal sealed GM50A series mass flow controllers on our CVD reactor permit highly accurate (1% setpoint accuracy) flow control and are accompanied by National Institute of Standards and Technology (NIST) traceable calibration sheets. Before all CVD reactions, we thoroughly washed and performed bake-out of quartz tubes (Quartz Plus, 22 mm inner diameter, 25.4 mm outer diameter) at 500 °C for 2 h under a N_2 flow of 50 standard cubic centimeters per minute (sccm).

Preparation of Si–P_x growth substrates by PH_3 treatment

Silicon wafers (Nova Electronic Materials, p-type 〈001〉, 0.001–0.005 Ω-cm, thickness 380 ± 25 μm SSP prime-grade Si wafers with two semi-standard flats and 2,000 Å ± 5% wet thermal oxide on both sides) were cut into individual substrates, each measuring ~ 2 × 2 cm^2. These substrates were rinsed with acetone and isopropyl alcohol and then cleaned by oxygen plasma treatment (Harrick Plasma) for 10 min at a pressure of ~650 mtorr and a radiofrequency power of 29.6 W. Substrates were then etched for 3 min in buffered hydrofluoric acid (BHF;

Transene Company, 10% Buffer HF Improved) to remove all SiO_2 (etch rate of SiO_2 in 10% BHF, ~100 nm min^{-1}).

After etching, these Si substrates were immediately loaded into the quartz tube of our CVD system and the system was evacuated to its base pressure of 0.01 mtorr within 10 min. Next, our reactor was flushed for 15 min under a constant 50-sccm flow of nitrogen (Airgas, 6 N-grade nitrogen with built-in-purifier). Next, N_2 flow was ceased, and the reactor returned to base pressure within 2 min. Phosphine gas (Air Liquide, 10% or 20% PH_3 in He) was then introduced into the reactor at a flow rate of 20 sccm for 10% PH_3 or 10 sccm for 20% PH_3. The total reactor pressure was set to, and subsequently maintained at, 80 torr for the duration of the reaction for 10% PH_3 or 40 Torr for 20% PH_3 (P_{PH3} = 8 torr). The furnace temperature in all three zones was set to rise to 150 °C at a rate of 12.5 °C min^{-1}. Once the furnace temperature reached 150 °C, the reaction was allowed to proceed for 1 h under a constant flow of PH_3. After 1 h, PH_3 flow was stopped, and the reactor was evacuated to base pressure. The reactor was then cooled to room temperature within 10 min, thereby ending the PH_3 treatment reaction.

Width Control

Si(001) substrates were treated with total PH_3 gas dosages of 26, 60 and 120 cm^3. The CVD reactor temperature was 150 °C.

Synthesis of 1D MoS_2 crystals

The PH_3-treated Si substrate mentioned above was immediately loaded into a clean quartz tube containing molybdenum (VI) oxide (Strem Chemicals, 99.999%) and sulfur (Sigma-Aldrich). The solid precursors were contained within two alumina crucibles (MTI, high-purity 50 × 5 × 5 mm3 combustion boats) in the following quantities: (1) 0.015 g and 0.104 mmol molybdenum (VI) oxide in one crucible, and (2) 0.250 g and 8 mmol sulfur in another. We controlled the position of the substrate and solid-phase precursors relative to each other, and also relative to the three heated zones of the furnace. The central furnace zone (held at 650 °C during the reaction) housed the substrate, which was placed face-down over the crucible containing molybdenum (VI) oxide. The furnace zone upstream of the central zone (held at 250 °C during the reaction) housed the crucible containing sulfur. The reactor was subjected to four purge cycles, each of which consisted of flushing the reactor for 2 min under a 200-sccm flow of N_2. This purge process and evacuation to base pressure was complete within 15 min. After reaching base pressure, the flow rate of N_2 was changed to 20 sccm and the furnace temperature was increased from room temperature to 650 °C at a rate of 14 °C min^{-1}. Once the furnace temperature had reached 650 °C, reactor total

pressure was set to 40 torr and the reaction was allowed to proceed for 15 min at 650 °C. After 15 min, the reactor was rapidly cooled to room temperature under a 200-sccm flow of N_2, thereby ending the MoS_2 reaction. For the experiments shown in Fig. 3.6, PH_3-treated SiO_2 substrates were placed downstream of the central furnace zone containing PH_3-treated Si substrates (this downstream zone was also held at 650 °C during the reaction) and were exposed to the MoS_2 reaction conditions described in this section. This positioning of substrates and reagents is depicted in Fig. 3.4.

Scanning Electron Microscopy (SEM)

High-resolution SEMs were obtained on a Tescan Mira3 GMU SEM equipped with a field emission gun and Octane Plus silicon drift detectors for energy-dispersive X-ray spectroscopy analysis. ImageJ and MATLAB were used to perform statistical analyses of the SEM images of 1D MoS_2 crystals to extract information on their yield, dimensions, aspect ratio and in-plane orientation.

Theory

Cluster Expansion

Cluster expansions are generalized using models that account for many-body interactions and are used here to predict the equilibrium structure of Si–P_x surfaces. For the slabs in this study, we assume that each site can be occupied by

either a Si/P atom or a vacancy (only in the outmost layer) based on the (1 × 2) dimer-reconstructed cell, as it is known that dimers are formed on the Si(001) surface[71]. Cluster expansion allows for the incorporation of P atoms on the Si surface, their penetration into deeper layers and the formation of surface defects. We fit the cluster expansion to a set of training structures calculated using density functional theory (DFT) using a Bayesian method that improves the predictive accuracy of the cluster expansion.[72,73] The training set contains randomly generated structures with varying P and vacancy concentrations. Ground-state structures predicted by the cluster expansion were added back to the training set to improve the quality of cluster expansion. For this cluster expansion, a total of 114 structures are in the training set and the root mean square leave-one-out cross-validation error is 5.4 meV per atom relative to DFT.

Density Functional Theory (DFT)

All DFT calculations were performed using the Vienna Ab initio Simulation Package (VASP).[74] For the Si–P-Vacancy cluster expansion, the revised Perdew–Burke–Ernzerhof exchange-correlation functional was used.[75] For calculations involving MoS_2, the PBE functional with van der Waals dispersion correction was used (denoted as PBE-D3), as it has been shown to provide more accurate energetics of MoS_2.[76–78] The Si_GW, P_GW, H_GW, O_GW, Mo_pv and S_GW PBE projector-augmented wave potentials were used,

and all VASP calculations were run with accurate precision.[79] For the Si–P-Vacancy training set structures, the Brillouin zone was sampled using grids generated by the k-point grid server with a minimum distance of 20 Å between real-space lattice points.[80] Because of the size of the slabs used for MoS_2 adsorption calculations, only a single k-point at the center of the Brillouin zone was used. Gaussian smearing with a width of 0.05 eV was used, and total energies were subsequently extrapolated to T = 0. The convergence criteria for the electronic self-consistent iteration and ionic relaxation loop were set to 10^{-4} and 10^{-3} eV, respectively.

3.3 Discussion

The synthesis of TMD nanoribbons utilizing a novel synthetic design is of significant interest to the TMD community. Understanding the results and rationales belying this method is critical to spreading its use as a mainstream technique in the TMD community. A scanning electron micrograph showing a single MoS_2 nanoribbon is presented here (Fig. 3.5).

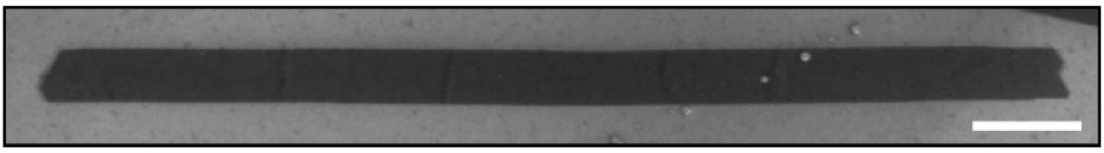

Figure 3.5. High resolution scanning electron micrograph of a single 1D MoS_2 crystal. The edges of the nanoribbon appear smooth and without significant variation. Scale bar, 500 nm.

This material has several features that require understanding how the synthetic process unfolds to then understand how to best deterministically modulate those characteristics. First, we note that in this micrograph the edges are exceptionally smooth along its length. Second, the width of this nanoribbon (~ 200 nm) approaches technologically relevant widths, which are considered widths below 50 nm. Nanoribbons of widths significantly lower than exhibited here will exhibit quantum confinement effects and may undergo phase change to a metallic state motivating us to further understand how this growth process functioned.

To first confirm that the Si-P_x substrate was uniquely directing the growth of anisotropic nanoribbons, we also examined the canonical MoS_2 reaction not only on phosphinated (PH_3) Si (001) surface, but a phosphinated SiO_2 surface. This was to ensure that the PH_3 conditions could not interact with the inert SiO_2 surface as it could with the Si (001) surface. A micrograph showing similar 2D characteristics to canonical 2D TMD growths is shown (Fig. 3.6). In this reaction the SiO_2 likely did not react with the PH_3 gas at the relatively mild temperatures employed here. Therefore, the TMD growth proceeded on SiO_2 as normal.

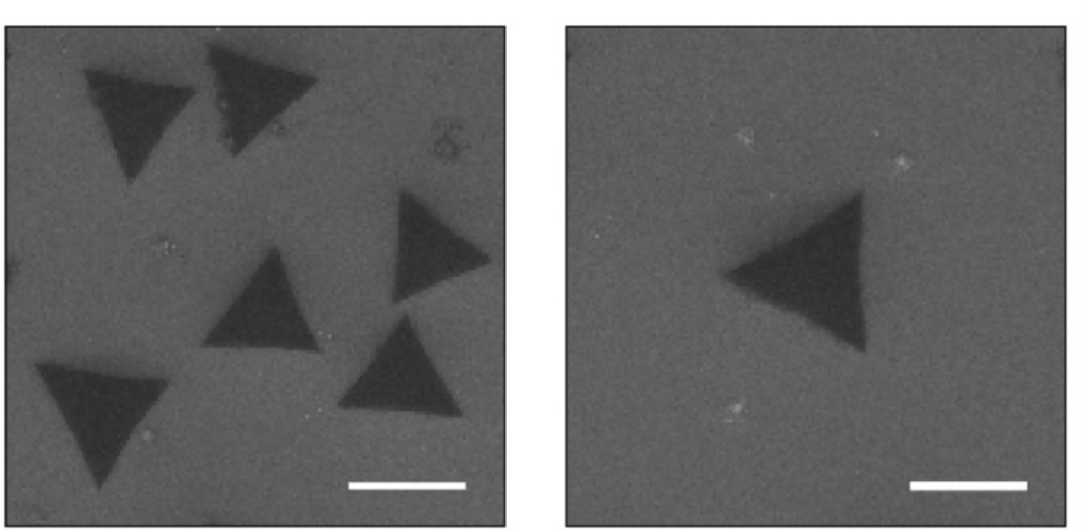

Figure 3.6. Scanning electron micrographs of 2D MoS_2 grown on SiO_2 substrates that have had PH_3 flown over the substrates. No deviation from using SiO_2 substrates was observed. Scale bars, 10 μm.

Now that the deterministic role of PH_3 dosage on a Si(001) substrate was established, we investigated the evolution of the one-dimensional moieties on the surface. Increasing the overall dosage from 0.01 to 8 Torr yielded significant changes in morphology. PH_3 flow and reaction pressure during surface functionalization were modified to many different values while the MoS_2 growth procedure was kept constant. An extremely low PH_3 dosage at 0.01 Torr was found to induce serration and disruption along the triangular 2D material edges (Fig. 3.7) whereas growths at 8 Torr yielded moieties exhibited in Fig. 3.5. This result corroborated the idea that PH_3 surface concentration significantly influences crystal morphology.

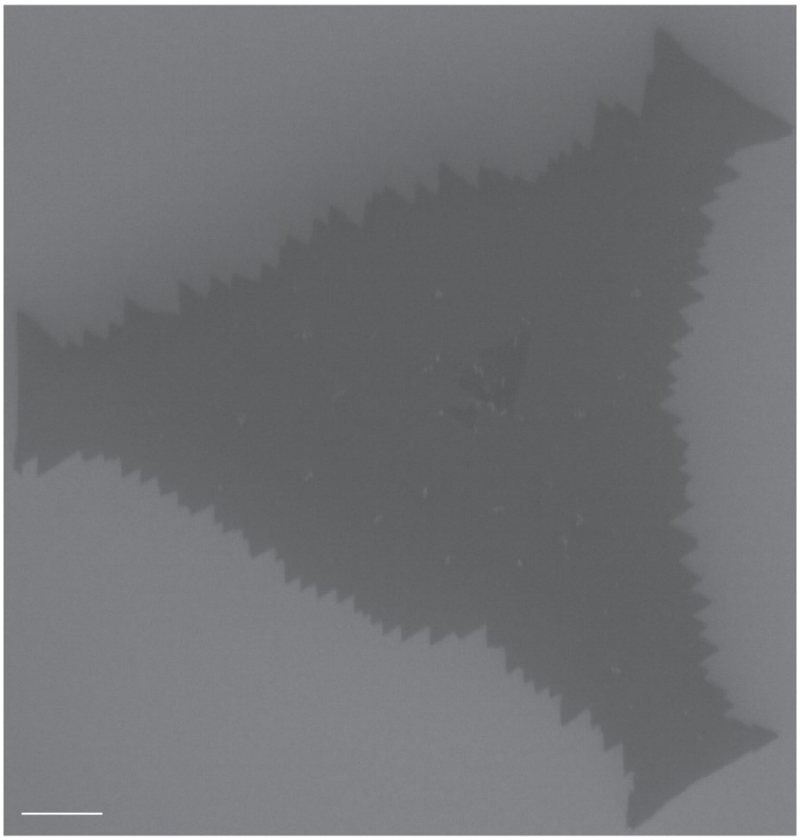

Figure 3.7. Scanning electron micrograph of a TMD crystal on a Si-P_x surface that has been functionalized with a low dose of PH_3 at 0.01 Torr. Disruption of edge fidelity is apparent, but anisotropic growth does not commence at this low dose.

This designer substrate method is novel in the TMD community and presents an exciting approach to utilizing prescribed material-substrate interactions to coax out new material properties. Previous efforts in materials science have utilized surface functionalization for various materials, such as self-assembled monolayers (SAMs) that have been both used as a material themselves and as a building block for a variety of materials.[81,82] However, no

such prescribed method has significantly altered the morphology and properties of TMD crystals to this degree.

Next, we wanted to investigate the genesis of the anisotropic growth mode. Normally, during the concerted growth of 2D TMDs on conventional substrates like SiO_2, there is a seed nucleus which diffuses out laterally to form the 2D material as mentioned in Chapter 2 (Fig. 3.8).

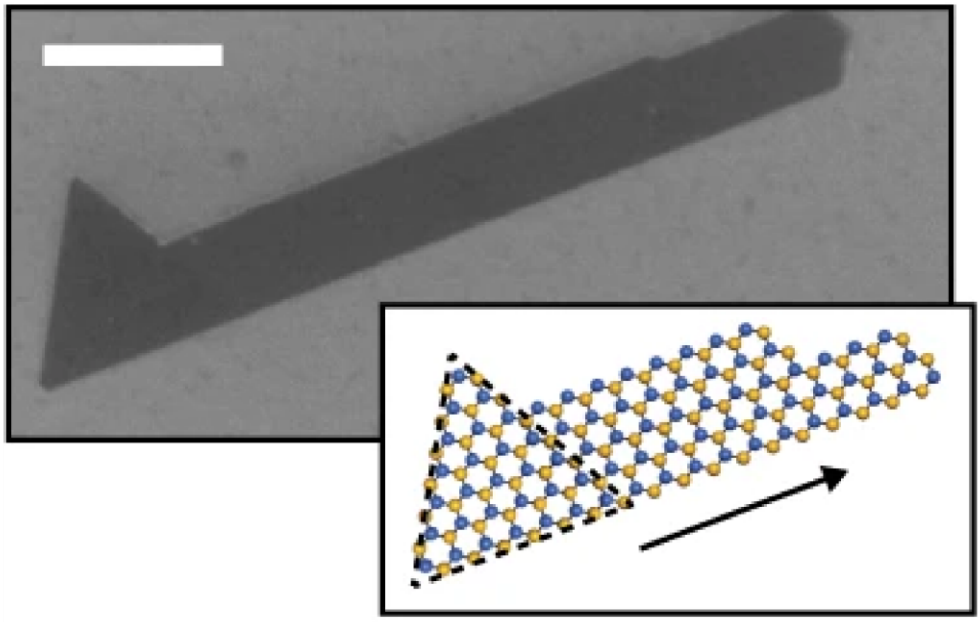

Figure 3.8. High resolution scanning electron micrograph visualizing the extrusion of a one-dimensional moiety from a two-dimensional seed crystal. Scale bar, 500 nm. Inset: schematic depicting the proposed direction of growth of the 1D crystal.

As mentioned in Chapter 2, there has been some effort in tracking the evolution of an initial nucleosome towards a 2D sheet morphology. However, analogously arresting growth of these nanoribbons early in the process does not yield 2D seeds with a shorter nanoribbon extrusion as might be expected by Fig. 3.8. This implies the near instantaneous effective transition from a 2D "seed" into a 1D nanoribbon and a rapid directed growth rate. This is reinforced by not currently observing a significant relationship between reaction time and nanoribbon length. Further, it is clear that the size of the 2D "seed" is of paramount importance when considering the width of the nanoribbon in question, as can be seen in Fig. 3.8. The nanoribbons in many cases possess widths on the order of one half an edge length of a 2D seed. It is unknown currently which parameters promote larger or smaller 2D crystal domains on a Si-P_x substrate, though chapter 4 discusses a strategy to influence this parameter during growth. In previous work on primarily SiO_2, the size of 2D MoS_2 and other TMDs has primarily focused on increasing lateral size of 2D TMD domains for use in practical technologies.[83–85] However, in this use case it would behoove the community to discern routes towards smaller 2D seeds and therefore narrower nanoribbons towards interesting phenomenological effects.

Though the synthesis of smaller 2D domains will be an advantageous route in the synthesis of narrower nanoribbons, we turned to modulation of the

surface directing moieties to alter the growth of these materials. In this work it has been determined that there is an inverse in the relationship between PH_3 dose and nanoribbon width (Fig. 3.9). Many different parameters, including varying PH_3 flow, pressure and duration of exposure, were modulated to uncover specific conditions amenable to nanoribbon growth. Small deviations in hold time and therefore total dosage can create a large deviation in nanoribbon results. This suggests that the width is a very sensitive function of PH_3 dosage as Small variations (<10%) in the PH_3 dosage volume exhibited greatly different results. The specificity of the volume of gas delivered over the surfaces is extremely high due to the precise delivery of gaseous reactants from mass flow controllers as shown in Fig. 3.4. For example, a sample with 26 mL of PH_3 gas during functionalization achieved an average nanoribbon width of 50, however, a sample with 30 mL of PH_3 achieved an average nanoribbon width of ~ 70 nm. Similarly, small variations in growth conditions during 2D TMDs do not yield similar magnitude differences in quality or quantity of materials. These observations cement the precarious nature of the designer surface and reinforce the robust nature of the synthesis of 2D TMDs.

The culmination of this work was uncovering the relationship between PH_3 dosage and nanoribbon width, an important quantity. Width distributions for nanoribbons derived at three different PH_3 dosages show the ability to tune

the morphology of MoS_2 nanoribbons through surface functionalization (Fig. 3.9).

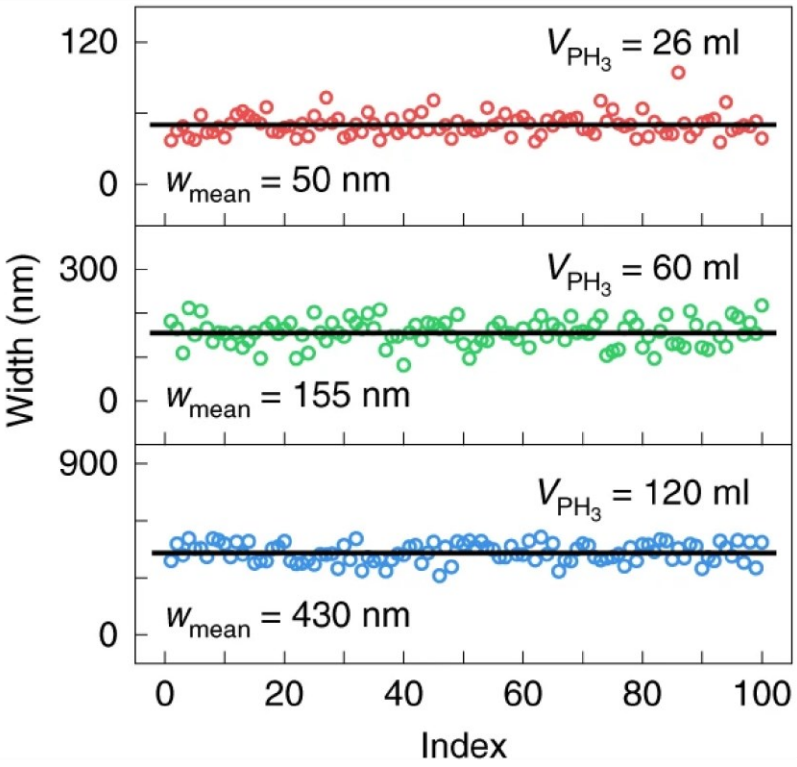

Figure 3.9. Width distributions for 100 randomly sampled 1D MoS_2 crystals grown on Si (001) surfaces treated with PH_3 dosages of 26, 60, and 120 mL from top to bottom respectively. The average width of the three conditions was 50, 155, and 430 nm from lowest PH_3 dose to highest.

We note that the overall nanoribbon width control ranges from nanoribbons below 50 nm width (~ 35 nm) nanoribbons to ~ 550 nm width nanoribbons. This control utilizing a simple functionalization concentration change is a useful method in using designer substrates methods towards scalable

growth of 1D TMD moieties. Representative micrographs of nanoribbons from each condition are shown (Fig. 3.10).

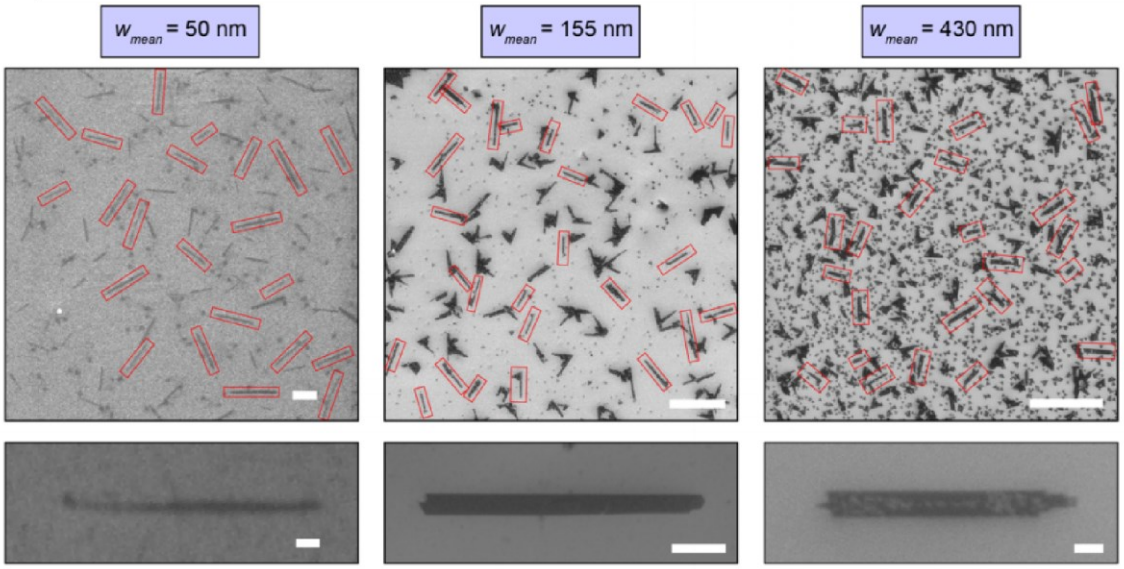

Figure 3.10. Representative scanning electron micrograph images taken at low (top) and high (bottom) magnifications of 3 different 1D MoS_2 nanoribbon samples synthesized on Si (001) substrates that were treated with 26 (left), 60 (middle), and 120 (right) mL. Width data was taken from micrographs such as these and for the distributions shown in Fig. 3.9. Red boxes denote clear single MoS_2 nanoribbons. Scale bars for the 50 nm average sample: 1 μm (top) and 100 nm (bottom). Scale bars for 155 nm average sample: 5 μm (top), 500 nm (bottom). Scale bars for 430 nm average sample: 10 μm (top), 1 μm (bottom).

Following this intriguing result, we sought to understand further how the surface interacted with the incipient crystals and what possible mechanisms might explain this PH_3 dependance and the oft-occurring extrusion originating from a 2D seed. First, theoretical DFT calculations were taken to discern the

surface energies of several surface configurations and their interfacial energetic relationship to a small MoS_2 test crystal (Fig. 3.11).

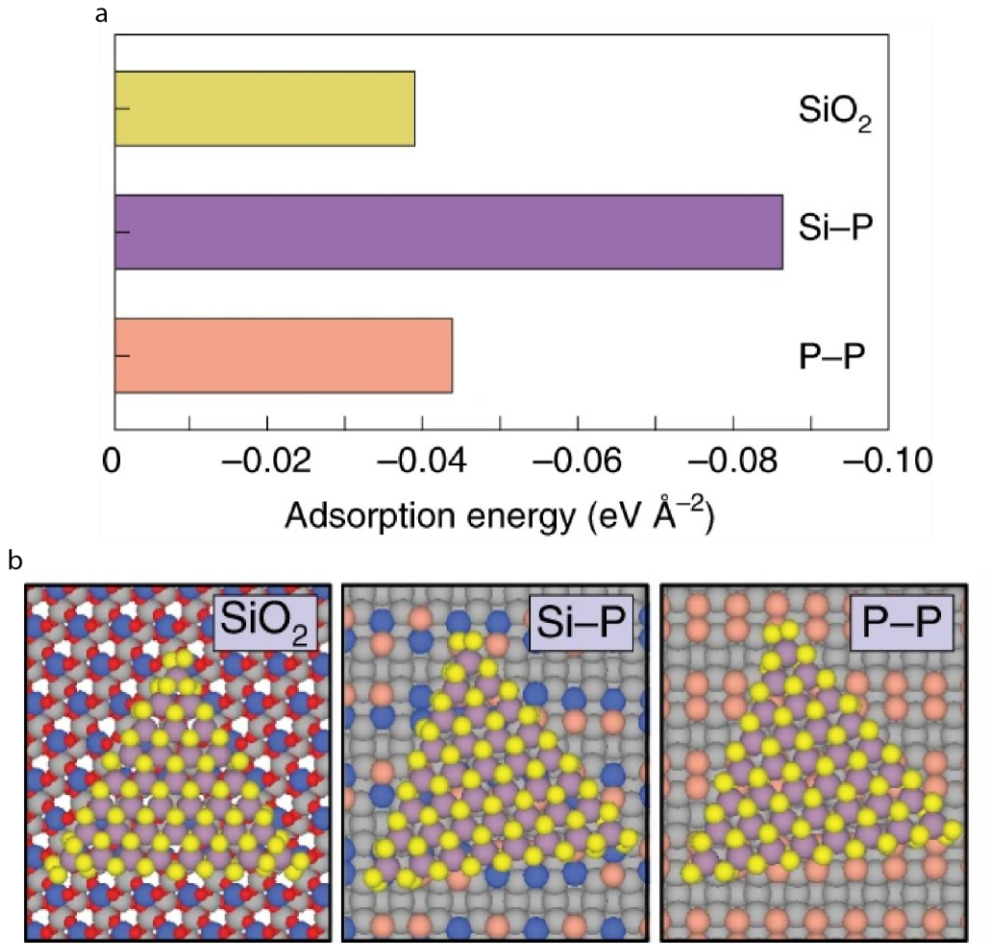

Figure 3.11. (a) DFT calculation results showing adsorption energy between an incipient MoS_2 crystal modeled as a 126-atom test particle and a P-P dimer covered surface (salmon), a Si-P dimer covered surface (purple) and a α-quartz (001) surface modelling SiO_2 (yellow). (b) 126 atom MoS_2 test particles adsbored on SiO_2, Si-P, and P-P surfaces.

Second, cluster expansion calculations were performed to generate a theoretical snapshot of the surface before any disruption from the growth of the MoS_2 nanoribbons (Fig. 3.12).

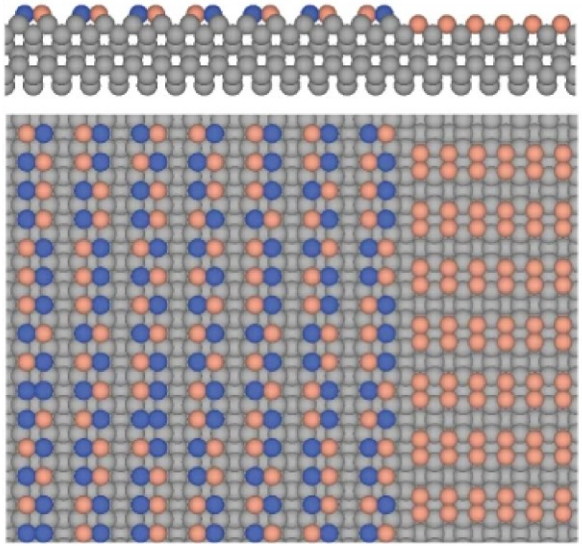

Figure 3.12. Side and top views of a representative Monte Carlo snapshot of the Si-P_x surface in equilibrium at 150 °C (the functionalization temperature) and PH_3 partial pressure of 8 Torr. Blue and salmon spheres correspond to Si and P atoms in the surface dimers respectively. Si atoms not in the top monolayer are depicted as gray spheres.

Several conclusions from these results can be made. First, the Si-P surface energy is the lowest with a MoS_2 crystal when compared to SiO_2 or P-P dimer rows. When examining the Monte Carlo snapshot of the Si-P_x surface shown in Fig. 3.12, we see that the two dominant species on the surface are P_2 and Si-P dimers. When combined with the DFT calculations, it is likely that the 2D seed

hypothesized to be the initial nucleosome for these nanoribbons, as exhibited in Fig. 3.8, deposits on the Si-P dimer domains and not P_2 domains. Understanding the effect of changing growth conditions, in contrast to the changing surface functionalization conditions as done here, is critical to understanding the whole picture of designer surface mediated nanoribbon growth. Growth modulation and subsequent consequences on the idea of this mechanism is explored chapter 4.

The development of utilizing prescribed designer substrates to modulate the dimensionality of MoS_2 nanoribbons is an important step in the advancement of one-dimensional TMD materials. Importantly, we observe that the morphology of the nanoribbons is further tunable through simple tuning of the PH_3 dosage. However, we note that the designer surfaces are sensitive to reaction environments and require more investigation to fully understand the underlying mechanisms regarding these anisotropic growth modes.

3.4 References

(1) Chowdhury, T.; Sadler, E. C.; Kempa, T. J. Progress and Prospects in Transition-Metal Dichalcogenide Research Beyond 2D. *Chem. Rev.* **2020**, *120* (22), 12563–12591.

(2) Munkhbat, B.; Yankovich, A. B.; Baranov, D. G.; Verre, R.; Olsson, E.; Shegai, T. O. Transition Metal Dichalcogenide Metamaterials with Atomic Precision. *Nat. Commun.* **2020**, *11* (1), 4604.

(3) Yagmurcukardes, M.; Peeters, F. M.; Senger, R. T.; Sahin, H. Nanoribbons: From Fundamentals to State-of-the-Art Applications. *Appl. Phys. Rev.* **2016**, *3* (4), 041302.

(4) Chen, R.; Zhao, T.; Wu, W.; Wu, F.; Li, L.; Qian, J.; Xu, R.; Wu, H.; Albishri, H. M.; Al-Bogami, A. S.; El-Hady, D. A.; Lu, J.; Amine, K. Free-Standing Hierarchically Sandwich-Type Tungsten Disulfide Nanotubes/Graphene Anode for Lithium-Ion Batteries. *Nano Lett.* **2014**, *14* (10), 5899–5904.

(5) Chen, Z.; Cummins, D.; Reinecke, B. N.; Clark, E.; Sunkara, M. K.; Jaramillo, T. F. Core–Shell MoO_3 –MoS_2 Nanowires for Hydrogen Evolution: A Functional Design for Electrocatalytic Materials. *Nano Lett.* **2011**, *11* (10), 4168–4175.

(6) Empante, T. A.; Martinez, A.; Wurch, M.; Zhu, Y.; Geremew, A. K.; Yamaguchi, K.; Isarraraz, M.; Rumyantsev, S.; Reed, E. J.; Balandin, A. A.; Bartels, L. Low Resistivity and High Breakdown Current Density of 10 nm Diameter van Der Waals $TaSe_3$ Nanowires by Chemical Vapor Deposition. *Nano Lett.* **2019**, *19* (7), 4355–4361.

(7) Jariwala, D.; Sangwan, V. K.; Wu, C.-C.; Prabhumirashi, P. L.; Geier, M. L.; Marks, T. J.; Lauhon, L. J.; Hersam, M. C. Gate-Tunable Carbon Nanotube–MoS_2 Heterojunction p-n Diode. *PNAS* **2013**, *110* (45), 18076–18080.

(8) Fathipour, S.; Remskar, M.; Varlec, A.; Ajoy, A.; Yan, R.; Vishwanath, S.; Rouvimov, S.; Hwang, W. S.; Xing, H. G.; Jena, D.; Seabaugh, A. Synthesized Multiwall MoS_2 Nanotube and Nanoribbon Field-Effect Transistors. *Appl. Phys. Lett.* **2015**, *106* (2), 022114.

(9) Gilbert, S. J.; Yi, H.; Chen, J.-S.; Yost, A. J.; Dhingra, A.; Abourahma, J.; Lipatov, A.; Avila, J.; Komesu, T.; Sinitskii, A.; Asensio, M. C.; Dowben, P. A. Effect of Band Symmetry on Photocurrent Production in Quasi-One-Dimensional Transition-Metal Trichalcogenides. *ACS Appl. Mater. Interfaces* **2020**, *12* (36), 40525–40531.

(10) Cui, P.; Choi, J.-H.; Chen, W.; Zeng, J.; Shih, C.-K.; Li, Z.; Zhang, Z. Contrasting Structural Reconstructions, Electronic Properties, and Magnetic Orderings along Different Edges of Zigzag Transition Metal Dichalcogenide Nanoribbons. *Nano Lett.* **2017**, *17* (2), 1097–1101.

(11) Zhang, H.; Li, X.-B.; Liu, L.-M. Tunable Electronic and Magnetic Properties of WS2 Nanoribbons. *J. Appl. Phys.* **2013**, *114* (9), 093710.

(12) Colomés, E.; Franz, M. Antichiral Edge States in a Modified Haldane Nanoribbon. *Phys. Rev. Lett.* **2018**, *120* (8), 086603.

(13) Dias, A. C.; Qu, F.; Azevedo, D. L.; Fu, J. Band Structure of Monolayer Transition-Metal Dichalcogenides and Topological Properties of Their Nanoribbons: Next-Nearest-Neighbor Hopping. *Phys. Rev. B* **2018**, *98* (7), 075202.

(14) Barone, V.; Hod, O.; Scuseria, G. E. Electronic Structure and Stability of Semiconducting Graphene Nanoribbons. *Nano Lett.* **2006**, *6* (12), 2748–2754.
(15) Yang, L.; Park, C.-H.; Son, Y.-W.; Cohen, M. L.; Louie, S. G. Quasiparticle Energies and Band Gaps in Graphene Nanoribbons. *Phys. Rev. Lett.* **2007**, *99* (18), 186801.
(16) Brey, L.; Fertig, H. A. Electronic States of Graphene Nanoribbons Studied with the Dirac Equation. *Phys. Rev. B* **2006**, *73* (23), 235411.
(17) Son, Y.-W.; Cohen, M. L.; Louie, S. G. Energy Gaps in Graphene Nanoribbons. *Phys. Rev. Lett.* **2006**, *97* (21), 216803.
(18) Wang, Z. F.; Li, Q.; Zheng, H.; Ren, H.; Su, H.; Shi, Q. W.; Chen, J. Tuning the Electronic Structure of Graphene Nanoribbons through Chemical Edge Modification: A Theoretical Study. *Phys. Rev. B* **2007**, *75* (11), 113406.
(19) Han, M. Y.; Özyilmaz, B.; Zhang, Y.; Kim, P. Energy Band-Gap Engineering of Graphene Nanoribbons. *Phys. Rev. Lett.* **2007**, *98* (20), 206805.
(20) Yang, D. J.; Zhang, Q.; Chen, G.; Yoon, S. F.; Ahn, J.; Wang, S. G.; Zhou, Q.; Wang, Q.; Li, J. Q. Thermal Conductivity of Multiwalled Carbon Nanotubes. *Phys. Rev. B* **2002**, *66* (16), 165440.
(21) Fujii, M.; Zhang, X.; Xie, H.; Ago, H.; Takahashi, K.; Ikuta, T.; Abe, H.; Shimizu, T. Measuring the Thermal Conductivity of a Single Carbon Nanotube. *Phys. Rev. Lett.* **2005**, *95* (6), 065502.
(22) Demczyk, B. G.; Wang, Y. M.; Cumings, J.; Hetman, M.; Han, W.; Zettl, A.; Ritchie, R. O. Direct Mechanical Measurement of the Tensile Strength and Elastic Modulus of Multiwalled Carbon Nanotubes. *Materials Science and Engineering: A* **2002**, *334* (1), 173–178.
(23) Li, F.; Cheng, H. M.; Bai, S.; Su, G.; Dresselhaus, M. S. Tensile Strength of Single-Walled Carbon Nanotubes Directly Measured from Their Macroscopic Ropes. *Appl. Phys. Lett.* **2000**, *77* (20), 3161–3163.
(24) Bai, Y.; Zhang, R.; Ye, X.; Zhu, Z.; Xie, H.; Shen, B.; Cai, D.; Liu, B.; Zhang, C.; Jia, Z.; Zhang, S.; Li, X.; Wei, F. Carbon Nanotube Bundles with Tensile Strength over 80 GPa. *Nat. Nanotechnol.* **2018**, *13* (7), 589–595.
(25) Abbas, A. N.; Liu, G.; Liu, B.; Zhang, L.; Liu, H.; Ohlberg, D.; Wu, W.; Zhou, C. Patterning, Characterization, and Chemical Sensing Applications of Graphene Nanoribbon Arrays Down to 5 nm Using Helium Ion Beam Lithography. *ACS Nano* **2014**, *8* (2), 1538–1546.
(26) Denk, R.; Hohage, M.; Zeppenfeld, P.; Cai, J.; Pignedoli, C. A.; Söde, H.; Fasel, R.; Feng, X.; Müllen, K.; Wang, S.; Prezzi, D.; Ferretti, A.; Ruini, A.; Molinari, E.; Ruffieux, P. Exciton-Dominated Optical Response of Ultra-Narrow Graphene Nanoribbons. *Nat. Commun.* **2014**, *5* (1), 4253.
(27) Rizzo, D. J.; Veber, G.; Cao, T.; Bronner, C.; Chen, T.; Zhao, F.; Rodriguez, H.; Louie, S. G.; Crommie, M. F.; Fischer, F. R. Topological Band Engineering of Graphene Nanoribbons. *Nature* **2018**, *560* (7717), 204–208.
(28) Durr, R. A.; Haberer, D.; Lee, Y.-L.; Blackwell, R.; Kalayjian, A. M.; Marangoni, T.; Ihm, J.; Louie, S. G.; Fischer, F. R. Orbitally Matched Edge-Doping in Graphene Nanoribbons. *J. Am. Chem. Soc.* **2018**, *140* (2), 807–813.

(29) Tapasztó, L.; Dobrik, G.; Lambin, P.; Biró, L. P. Tailoring the Atomic Structure of Graphene Nanoribbons by Scanning Tunnelling Microscope Lithography. *Nat. Nanotechnol.* **2008**, *3* (7), 397–401.
(30) Tian, B.; Zheng, X.; Kempa, T. J.; Fang, Y.; Yu, N.; Yu, G.; Huang, J.; Lieber, C. M. Coaxial Silicon Nanowires as Solar Cells and Nanoelectronic Power Sources. *Nature* **2007**, *449* (7164), 885–889.
(31) Schmidt, V.; Wittemann, J. V.; Senz, S.; Gösele, U. Silicon Nanowires: A Review on Aspects of Their Growth and Their Electrical Properties. *Adv. Mater.* **2009**, *21* (25–26), 2681–2702.
(32) Wu, Y.; Cui, Y.; Huynh, L.; Barrelet, C. J.; Bell, D. C.; Lieber, C. M. Controlled Growth and Structures of Molecular-Scale Silicon Nanowires. *Nano Lett.* **2004**, *4* (3), 433–436.
(33) Deng, J.; Su, Y.; Liu, D.; Yang, P.; Liu, B.; Liu, C. Nanowire Photoelectrochemistry. *Chem. Rev.* **2019**, *119* (15), 9221–9259.
(34) Jia, C.; Lin, Z.; Huang, Y.; Duan, X. Nanowire Electronics: From Nanoscale to Macroscale. *Chem. Rev.* **2019**, *119* (15), 9074–9135.
(35) Quan, L. N.; Kang, J.; Ning, C.-Z.; Yang, P. Nanowires for Photonics. *Chem. Rev.* **2019**, *119* (15), 9153–9169.
(36) Spirkoska, D.; Arbiol, J.; Gustafsson, A.; Conesa-Boj, S.; Glas, F.; Zardo, I.; Heigoldt, M.; Gass, M. H.; Bleloch, A. L.; Estrade, S.; Kaniber, M.; Rossler, J.; Peiro, F.; Morante, J. R.; Abstreiter, G.; Samuelson, L.; Fontcuberta i Morral, A. Structural and Optical Properties of High Quality Zinc-Blende/Wurtzite GaAs Nanowire Heterostructures. *Phys. Rev. B* **2009**, *80* (24), 245325.
(37) Saxena, D.; Mokkapati, S.; Parkinson, P.; Jiang, N.; Gao, Q.; Tan, H. H.; Jagadish, C. Optically Pumped Room-Temperature GaAs Nanowire Lasers. *Nat. Photon.* **2013**, *7* (12), 963–968.
(38) Persson, A. I.; Larsson, M. W.; Stenström, S.; Ohlsson, B. J.; Samuelson, L.; Wallenberg, L. R. Solid-Phase Diffusion Mechanism for GaAs Nanowire Growth. *Nat. Mater.* **2004**, *3* (10), 677–681.
(39) Shen, G.; Chen, D.; Chen, P.-C.; Zhou, C. Vapor−Solid Growth of One-Dimensional Layer-Structured Gallium Sulfide Nanostructures. *ACS Nano* **2009**, *3* (5), 1115–1120.
(40) Wen, C.-Y.; Reuter, M. C.; Tersoff, J.; Stach, E. A.; Ross, F. M. Structure, Growth Kinetics, and Ledge Flow during Vapor−Solid−Solid Growth of Copper-Catalyzed Silicon Nanowires. *Nano Lett.* **2010**, *10* (2), 514–519.
(41) Lee, J. S.; Brittman, S.; Yu, D.; Park, H. Vapor–Liquid–Solid and Vapor–Solid Growth of Phase-Change Sb_2Te_3 Nanowires and Sb_2Te_3/GeTe Nanowire Heterostructures. *J. Am. Chem. Soc.* **2008**, *130* (19), 6252–6258.
(42) Lauhon, L. J.; Gudiksen, M. S.; Wang, D.; Lieber, C. M. Epitaxial Core–Shell and Core–Multishell Nanowire Heterostructures. *Nature* **2002**, *420* (6911), 57–61.
(43) Dick, K. A.; Kodambaka, S.; Reuter, M. C.; Deppert, K.; Samuelson, L.; Seifert, W.; Wallenberg, L. R.; Ross, F. M. The Morphology of Axial and Branched Nanowire Heterostructures. *Nano Lett.* **2007**, *7* (6), 1817–1822.

(44) Wen, C.-Y.; Reuter, M. C.; Bruley, J.; Tersoff, J.; Kodambaka, S.; Stach, E. A.; Ross, F. M. Formation of Compositionally Abrupt Axial Heterojunctions in Silicon-Germanium Nanowires. *Science* **2009**, *326* (5957), 1247–1250.
(45) Duan, X.; Lieber, C. M. General Synthesis of Compound Semiconductor Nanowires. *Advanced Materials* **2000**, *12* (4), 298–302.
(46) Strojnik, M.; Kovic, A.; Mrzel, A.; Buh, J.; Strle, J.; Mihailovic, D. MoS_2 Nanotube Field Effect Transistors. *AIP Adv.* **2014**, *4* (9), 097114.
(47) Nethravathi, C.; Jeffery, A. A.; Rajamathi, M.; Kawamoto, N.; Tenne, R.; Golberg, D.; Bando, Y. Chemical Unzipping of WS_2 Nanotubes. *ACS Nano* **2013**, *7* (8), 7311–7317.
(48) Zhang, Y. J.; Ideue, T.; Onga, M.; Qin, F.; Suzuki, R.; Zak, A.; Tenne, R.; Smet, J. H.; Iwasa, Y. Enhanced Intrinsic Photovoltaic Effect in Tungsten Disulfide Nanotubes. *Nature* **2019**, *570* (7761), 349–353.
(49) Ghorbani-Asl, M.; Zibouche, N.; Wahiduzzaman, M.; Oliveira, A. F.; Kuc, A.; Heine, T. Electromechanics in MoS_2 and WS_2 : Nanotubes vs. Monolayers. *Sci. Rep.* **2013**, *3* (1), 2961.
(50) Wu, J.-B.; Zhao, H.; Li, Y.; Ohlberg, D.; Shi, W.; Wu, W.; Wang, H.; Tan, P.-H. Monolayer Molybdenum Disulfide Nanoribbons with High Optical Anisotropy. *Adv. Opt. Mater.* **2016**, *4* (5), 756–762.
(51) Botello-Méndez, A. R.; López-Urías, F.; Terrones, M.; Terrones, H. Metallic and Ferromagnetic Edges in Molybdenum Disulfide Nanoribbons. *Nanotechnology* **2009**, *20* (32), 325703.
(52) Cai, Y.; Zhang, G.; Zhang, Y.-W. Polarity-Reversed Robust Carrier Mobility in Monolayer MoS_2 Nanoribbons. *J. Am. Chem. Soc.* **2014**, *136* (17), 6269–6275.
(53) Deng, S.; Li, L.; Guy, O. J.; Zhang, Y. Enhanced Thermoelectric Performance of Monolayer MoSSe, Bilayer MoSSe and Graphene/MoSSe Heterogeneous Nanoribbons. *Phys. Chem. Chem. Phys.* **2019**, *21* (33), 18161–18169.
(54) Li, Y.; Zhou, Z.; Zhang, S.; Chen, Z. MoS_2 Nanoribbons: High Stability and Unusual Electronic and Magnetic Properties. *J. Am. Chem. Soc.* **2008**, *130* (49), 16739–16744.
(55) Kotekar-Patil, D.; Deng, J.; Wong, S. L.; Lau, C. S.; Goh, K. E. J. Single Layer MoS_2 Nanoribbon Field Effect Transistor. *Appl. Phys. Lett.* **2019**, *114* (1), 013508.
(56) Chen, S.; Kim, S.; Chen, W.; Yuan, J.; Bashir, R.; Lou, J.; van der Zande, A. M.; King, W. P. Monolayer MoS_2 Nanoribbon Transistors Fabricated by Scanning Probe Lithography. *Nano Lett.* **2019**, *19* (3), 2092–2098.
(57) Dago, A. I.; Ryu, Y. K.; Palomares, F. J.; Garcia, R. Direct Patterning of P-Type-Doped Few-Layer WSe_2 Nanoelectronic Devices by Oxidation Scanning Probe Lithography. *ACS Appl. Mater. Interfaces* **2018**, *10* (46), 40054–40061.
(58) Jadwiszczak, J.; Keane, D.; Maguire, P.; Cullen, C. P.; Zhou, Y.; Song, H.; Downing, C.; Fox, D.; McEvoy, N.; Zhu, R.; Xu, J.; Duesberg, G. S.; Liao, Z.-M.; Boland, J. J.; Zhang, H. MoS_2 Memtransistors Fabricated by Localized Helium Ion Beam Irradiation. *ACS Nano* **2019**, *13* (12), 14262–14273.
(59) Stanford, M. G.; Pudasaini, P. R.; Cross, N.; Mahady, K.; Hoffman, A. N.; Mandrus, D. G.; Duscher, G.; Chisholm, M. F.; Rack, P. D. Tungsten Diselenide

Patterning and Nanoribbon Formation by Gas-Assisted Focused-Helium-Ion-Beam-Induced Etching. *Small Methods* **2017**, *1* (4), 1600060.
(60) Chen, J.; Ryu, G. H.; Zhang, Q.; Wen, Y.; Tai, K.-L.; Lu, Y.; Warner, J. H. Spatially Controlled Fabrication and Mechanisms of Atomically Thin Nanowell Patterns in Bilayer WS_2 Using *in Situ* High Temperature Electron Microscopy. *ACS Nano* **2019**, *13* (12), 14486–14499.
(61) Huang, W.; Wang, X.; Ji, X.; Zhang, Z.; Jin, C. In-Situ Fabrication of Mo_6S_6-Nanowire-Terminated Edges in Monolayer Molybdenum Disulfide. *Nano Res.* **2018**, *11* (11), 5849–5857.
(62) Sang, X.; Li, X.; Zhao, W.; Dong, J.; Rouleau, C. M.; Geohegan, D. B.; Ding, F.; Xiao, K.; Unocic, R. R. In Situ Edge Engineering in Two-Dimensional Transition Metal Dichalcogenides. *Nat. Commun.* **2018**, *9* (1), 2051.
(63) Koós, A. A.; Vancsó, P.; Magda, G. Z.; Osváth, Z.; Kertész, K.; Dobrik, G.; Hwang, C.; Tapasztó, L.; Biró, L. P. STM Study of the MoS_2 Flakes Grown on Graphite: A Model System for Atomically Clean 2D Heterostructure Interfaces. *Carbon* **2016**, *105*, 408–415.
(64) Fox, D. S.; Zhou, Y.; Maguire, P.; O'Neill, A.; Ó'Coileáin, C.; Gatensby, R.; Glushenkov, A. M.; Tao, T.; Duesberg, G. S.; Shvets, I. V.; Abid, M.; Abid, M.; Wu, H.-C.; Chen, Y.; Coleman, J. N.; Donegan, J. F.; Zhang, H. Nanopatterning and Electrical Tuning of MoS $_2$ Layers with a Subnanometer Helium Ion Beam. *Nano Lett.* **2015**, *15* (8), 5307–5313.
(65) Liu, X.; Xu, T.; Wu, X.; Zhang, Z.; Yu, J.; Qiu, H.; Hong, J.-H.; Jin, C.-H.; Li, J.-X.; Wang, X.-R.; Sun, L.-T.; Guo, W. Top–down Fabrication of Sub-Nanometre Semiconducting Nanoribbons Derived from Molybdenum Disulfide Sheets. *Nat. Commun.* **2013**, *4* (1), 1776.
(66) Li, S.; Lin, Y.-C.; Zhao, W.; Wu, J.; Wang, Z.; Hu, Z.; Shen, Y.; Tang, D.-M.; Wang, J.; Zhang, Q.; Zhu, H.; Chu, L.; Zhao, W.; Liu, C.; Sun, Z.; Taniguchi, T.; Osada, M.; Chen, W.; Xu, Q.-H.; Wee, A. T. S.; Suenaga, K.; Ding, F.; Eda, G. Vapour–Liquid–Solid Growth of Monolayer MoS_2 Nanoribbons. *Nat. Mater.* **2018**, *17* (6), 535–542.
(67) Aljarb, A.; Fu, J.-H.; Hsu, C.-C.; Chuu, C.-P.; Wan, Y.; Hakami, M.; Naphade, D. R.; Yengel, E.; Lee, C.-J.; Brems, S.; Chen, T.-A.; Li, M.-Y.; Bae, S.-H.; Hsu, W.-T.; Cao, Z.; Albaridy, R.; Lopatin, S.; Chang, W.-H.; Anthopoulos, T. D.; Kim, J.; Li, L.-J.; Tung, V. Ledge-Directed Epitaxy of Continuously Self-Aligned Single-Crystalline Nanoribbons of Transition Metal Dichalcogenides. *Nat. Mater.* **2020**, 1–7.
(68) Ma, Z.; Wang, S.; Deng, Q.; Hou, Z.; Zhou, X.; Li, X.; Cui, F.; Si, H.; Zhai, T.; Xu, H. Epitaxial Growth of Rectangle Shape MoS_2 with Highly Aligned Orientation on Twofold Symmetry A-Plane Sapphire. *Small* **2020**, *16* (16), 2000596.
(69) Huh, W.; Jang, S.; Lee, J. Y.; Lee, D.; Lee, D.; Lee, J. M.; Park, H.-G.; Kim, J. C.; Jeong, H. Y.; Wang, G.; Lee, C.-H. Synaptic Barristor Based on Phase-Engineered 2D Heterostructures. *Adv. Mater.* **2018**, *30* (35), 1801447.
(70) Voiry, D.; Mohite, A.; Chhowalla, M. Phase Engineering of Transition Metal Dichalcogenides. *Chem. Soc. Rev.* **2015**, *44* (9), 2702–2712.

(71) Wang, Y.; Chen, X.; Hamers, R. J. Atomic-Resolution Study of Overlayer Formation and Interfacial Mixing in the Interaction of Phosphorus with Si(001). *Phys. Rev. B* **1994**, *50* (7), 4534–4547.
(72) Kohn, W.; Sham, L. J. Self-Consistent Equations Including Exchange and Correlation Effects. *Phys. Rev.* **1965**, *140* (4A), A1133–A1138.
(73) Mueller, T.; Ceder, G. Bayesian Approach to Cluster Expansions. *Phys. Rev. B* **2009**, *80* (2), 024103.
(74) Kresse, G.; Hafner, J. Ab Initio Molecular Dynamics for Liquid Metals. *Phys. Rev. B* **1993**, *47* (1), 558–561.
(75) Hammer, B.; Hansen, L. B.; Nørskov, J. K. Improved Adsorption Energetics within Density-Functional Theory Using Revised Perdew-Burke-Ernzerhof Functionals. *Phys. Rev. B* **1999**, *59* (11), 7413–7421.
(76) Perdew, J. P.; Burke, K.; Ernzerhof, M. Generalized Gradient Approximation Made Simple. *Phys. Rev. Lett.* **1996**, *77* (18), 3865–3868.
(77) Grimme, S.; Antony, J.; Ehrlich, S.; Krieg, H. A Consistent and Accurate Ab Initio Parametrization of Density Functional Dispersion Correction (DFT-D) for the 94 Elements H-Pu. *J. Chem. Phys.* **2010**, *132* (15), 154104.
(78) Reckien, W.; Janetzko, F.; Peintinger, M. F.; Bredow, T. Implementation of Empirical Dispersion Corrections to Density Functional Theory for Periodic Systems. *J. Comput. Chem.* **2012**, *33* (25), 2023–2031.
(79) Blöchl, P. E. Projector Augmented-Wave Method. *Phys. Rev. B* **1994**, *50* (24), 17953–17979.
(80) Wisesa, P.; McGill, K. A.; Mueller, T. Efficient Generation of Generalized Monkhorst-Pack Grids through the Use of Informatics. *Phys. Rev. B* **2016**, *93* (15), 155109.
(81) Zhou, C.; Deshpande, M. R.; Reed, M. A.; Jones, L.; Tour, J. M. Nanoscale Metal/Self-Assembled Monolayer/Metal Heterostructures. *Appl. Phys. Lett.* **1997**, *71* (5), 611–613.
(82) Schwartz, D. K. Mechanisms and Kinetics of Self-Assembled Monolayer Formation. *Annu. Rev. Phys. Chem.* **2001**, *52* (1), 107–137.
(83) Chen, J.; Zhao, X.; Tan, S. J. R.; Xu, H.; Wu, B.; Liu, B.; Fu, D.; Fu, W.; Geng, D.; Liu, Y.; Liu, W.; Tang, W.; Li, L.; Zhou, W.; Sum, T. C.; Loh, K. P. Chemical Vapor Deposition of Large-Size Monolayer $MoSe_2$ Crystals on Molten Glass. *J. Am. Chem. Soc.* **2017**, *139* (3), 1073–1076.
(84) Dumcenco, D.; Ovchinnikov, D.; Sanchez, O. L.; Gillet, P.; Alexander, D. T. L.; Lazar, S.; Radenovic, A.; Kis, A. Large-Area MoS_2 Grown Using H_2S as the Sulphur Source. *2D Mater.* **2015**, *2* (4), 044005.
(85) Lee, Y.-H.; Zhang, X.-Q.; Zhang, W.; Chang, M.-T.; Lin, C.-T.; Chang, K.-D.; Yu, Y.-C.; Wang, J. T.-W.; Chang, C.-S.; Li, L.-J.; Lin, T.-W. Synthesis of Large-Area MoS_2 Atomic Layers with Chemical Vapor Deposition. *Adv. Mater.* **2012**, *24* (17), 2320–2325.

Chapter 4: Modulation of Growth Modes in $MoSe_2$ Nanoribbons Through Designer Surface Disruption

The work in this chapter has been submitted as:

E. C. Sadler, T. Chowdhury, R. Dziobek-Garrett, Li, C. T. Mueller, T. J. Kempa "Substrate Templated Synthesis of $MoSe_2$ Nanoribbons"

Submitted to ACS Applied Materials and Interfaces

4.1 Introduction

Nanoribbons of MoS_2 have been synthesized previously, however, in developing our novel designer substrate technique we realized the need for bottom-up TMD nanoribbon growth needed to expand to other compositions.[1–3] 2D MoS_2 requires the lowest reaction temperature out of the Mo and W containing TMD family due to the lower vaporization temperature of Mo compared to W and S compared to Se. These less intense conditions have proved useful for a variety of bottom-up syntheses, including previous work discussed in chapter 3 to create bottom-up grown nanoribbons, making MoS_2 an attractive option to explore new chemical interactions such as in the designer substrates.

However, much research has been carried out on the fabrication of low-dimensional $MoSe_2$ mono- and few-layer materials due to their attractive

properties that MoS_2 does not possess. The selenide family of TMDs presents entirely new capabilities compared to the sulfide family. For instance, when comparing $MoSe_2$ to MoS_2, the selenide optical emission range lies at a lower energy than its counterpart.[4–6] The selenide family ($MoSe_2$, WSe_2) have also shown promise in single photon emission due to its intrinsically narrower line profile in optical emission which is not seen in the sulfide family.[7–9] $MoSe_2$ has also exhibited higher field effect mobilities than that of MoS_2 as shown in several studies and $MoSe_2$ has exhibited superior photodetection capabilities due to its weaker bound exciton behavior.[4,10–14] Finally, the selenide family of TMDs have shown promise in spin and valley applications for quantum computing that the sulfide family has not, which may be the most important application of low-dimensional materials. (Fig. 4.1).[15–22] MoS_2, however, is superior in many catalytic applications, such as the hydrogen evolution reaction, due to its more chemical reactive sulfur atoms compared to selenium atoms in $MoSe_2$.[23–27]

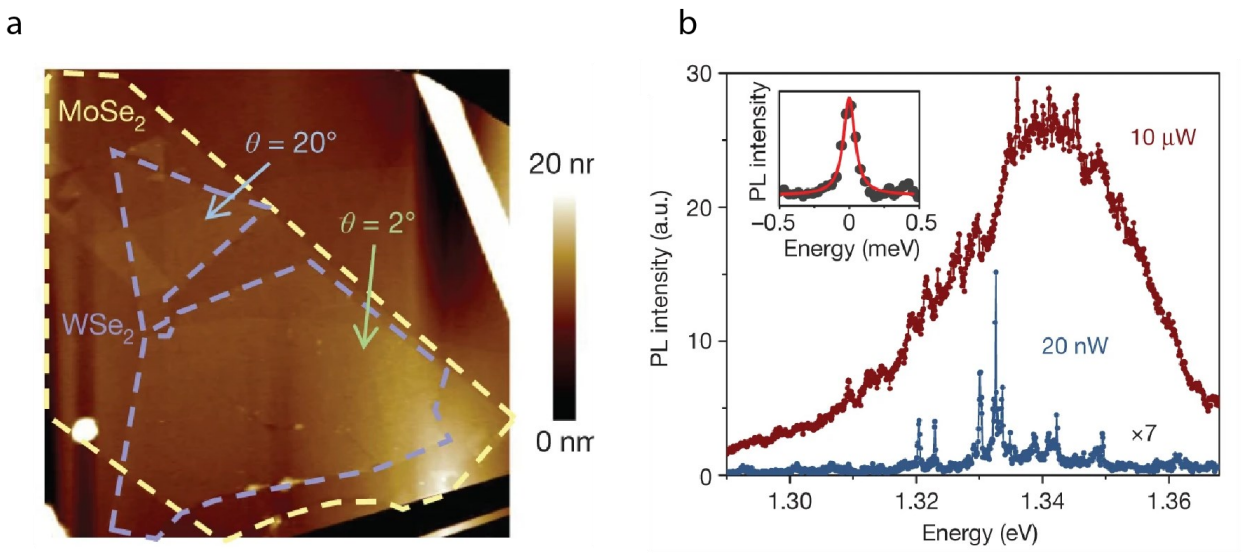

Figure 4.1.[15] (a) Optical micrograph showing a $MoSe_2/WSe_2$ heterostructure rotated at different angles for different grains. (b) Photoluminescence spectra for the heterostructure domain rotated 20° (blue) and 2° (red). There is an almost 2 orders of magnitude increase in the spectral intensity for the 2° rotated sample.

In their two-dimensional variety, MoS_2 and $MoSe_2$ share many similarities. Their crystal structures are both hexagonal varieties that occur in multiple polymorphs with the lowest energy being a '2H' phase, which is the most common allotrope created in gas-phase growths. Further, they both have shifts in their Raman spectra from the decreased dielectric screening in the monolayer variant that are useful identification signatures, possess indirect-to-direct bandgap transitions with decreasing layer number and intense photoluminescence spectral features that make for ready identification.[5,28–30] Both 2D materials, $MoSe_2$ and MoS_2, grow morphologically as triangles during

bottom-up gas phase synthesis. Generally, the same sort of reactions parameters, materials components, such as oxides and chalcogens, are used in CVD techniques for MoS_2 and $MoSe_2$.

However, the syntheses for MoS_2 and for $MoSe_2$ 2D monolayers exhibit several key differences. First, as mentioned earlier, harsher reaction conditions are needed to complete the synthesis of $MoSe_2$ compared to MoS_2 . This comes in the form of significantly higher temperatures (650 vs. 800 °C) and the presence of H_2 gas during the growth of $MoSe_2$ monolayers where no such requirement exists in the synthesis of 2D MoS_2.[4,6,31–33] This H_2 requirement is due to the lower reactivity of the Se reactants versus the S reactant. Additionally, most $MoSe_2$ syntheses are done over a much briefer time period than their MoS_2 counterparts. Additionally, in the fabrication of devices and measurement, $MoSe_2$ is an overall more robust material, able to withstand transfer, etching, and other processes more readily than its MoS_2 counterpart. Additionally, the robustness manifests in characterization techniques and post-synthetic modification, particular electron microscopy where beam irradiation and other concerns are lessened with $MoSe_2$.[34] Early efforts at $MoSe_2$ monolayer synthesis have generated large domain $MoSe_2$ crystals that exhibit characteristic optical properties (Fig. 4.2).[33] These early steps in creating low-dimensional $MoSe_2$ has been of great importance and acts

as the building block of guiding our designer growth technique towards other compositions, such as $MoSe_2$, as exhibited for MoS_2 in chapter 3.

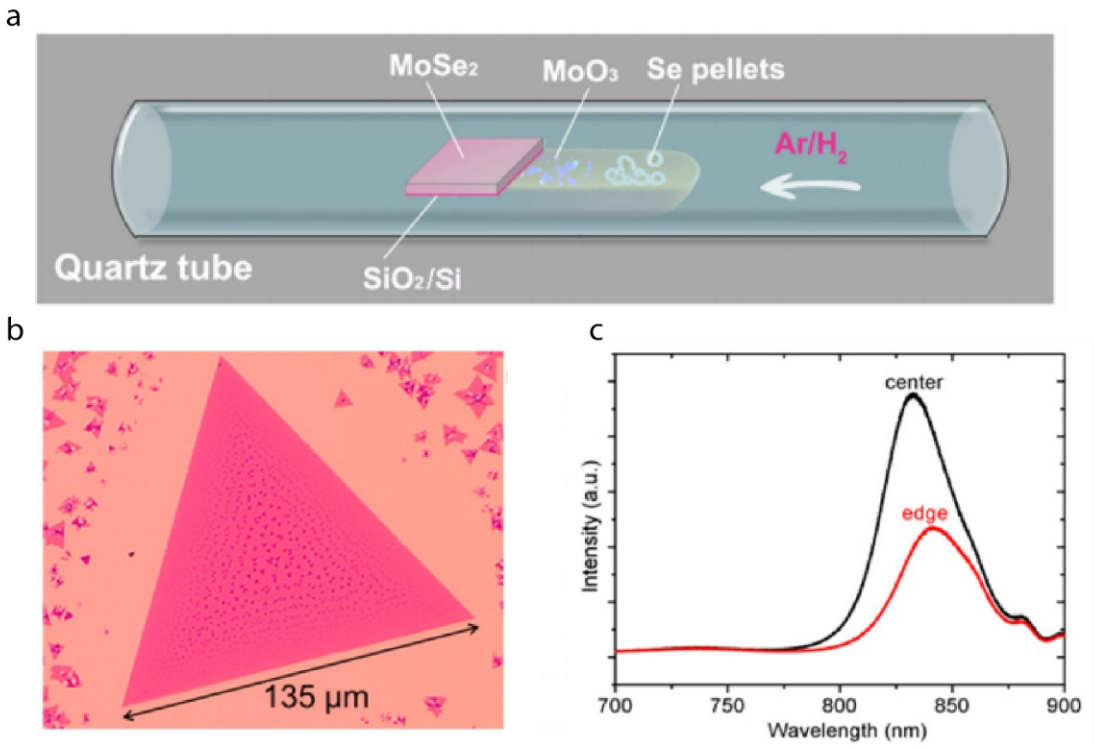

Figure 4.2.[33] (a) Schematic depicting a traditional setup of a two-dimensional $MoSe_2$ synthesis. (b) Optical micrograph of a large 2D $MoSe_2$ domain. (c) Photoluminescence spectra of a $MoSe_2$ flake taken at both the edge and center regions showing slight energy differences between edge and interior regions.

Top-down methods can be readily used in the pursuit of one-dimensional $MoSe_2$ and are only limited by the difficulty of the previous 2D synthetic procedures. However, the same problems for creating 1D materials from top-down methods such as scanning probes and electron beams, as discussed in chapter 3, are present. Namely, the lower quality edge structure, the

impossibility of bottom-up grown 1D heterostructures, and the serial nature of the top-down techniques all lead to an inadequate method towards the wide scale adoption of 1D nanoribbon moieties in the selenide family of TMDs.[35–37]

To fully exploit the full functionality TMD nanoribbon materials for applied technologies, there exists a need to translate scalable bottom-up methods to multiple TMD compositions, beyond MoS_2. Beyond their different intrinsic properties across the Mo and W family of TMDs, TMDs that are heterostructures of different monolayers of material have proved extremely powerful for a variety of applications as discussed in Chapter 1. These heterostructures motivated us to explore further compositions utilizing our designer surface method. Importantly, the expansion of this designer technique strategy and the evolution of planar nanoribbon van der Waals heterostructures will allow the utilization of dimensional confinement for directed tuning of excitonic properties. When combined with other methods of excitonic control, such as Moire interference patterns, excitonic phenomena will be able to be manipulated even further and have with the combination of dimensional confinement and Moire heterostructure effects in either the selenide or mixed sulfide-selenide family[15,38–42] Further, the designer surface method, while promising in being able to create bottom-up grown narrow nanoribbons, needed to be scaled to other material compositions to prove its utility in the TMD community.

We note that the few attempts before now at scalable bottom-up growth have centered on MoS_2, being the canonical TMD material, with methods discussed in the last chapter. We do note the existence of techniques to fabricate $MoSe_2$ nanoribbons through other techniques, notably using MBE with pre-patterned Au surfaces and unique phase transitions at low areal coverages.[43–45] For example, Chen et al. demonstrated the use of MBE towards synthesis of TMD nanoribbons (Fig. 4.3).[44] This was done through a morphological phase transition from 0D to 1D materials. However, this suffers from the usual MBE shortcomings, such as its serial nature, which limits its scalability and applicability. However, the materials generated are exceptional monodisperse in thickness, width, and aspect ratio compared to other bottom-up growth methods discussed in Chapter 3. MBE methods afford high control over all of these parameters. Another method, utilizing similar fine control over materials effusion, was employed on an Au(100) surface, exploiting its advantageous, highly ordered surface.[45] When the ratios of Se and Mo atoms were tuned precisely, ultra-narrow nanoribbons (< 5 nm) were synthesized successfully (Fig. 4.3).

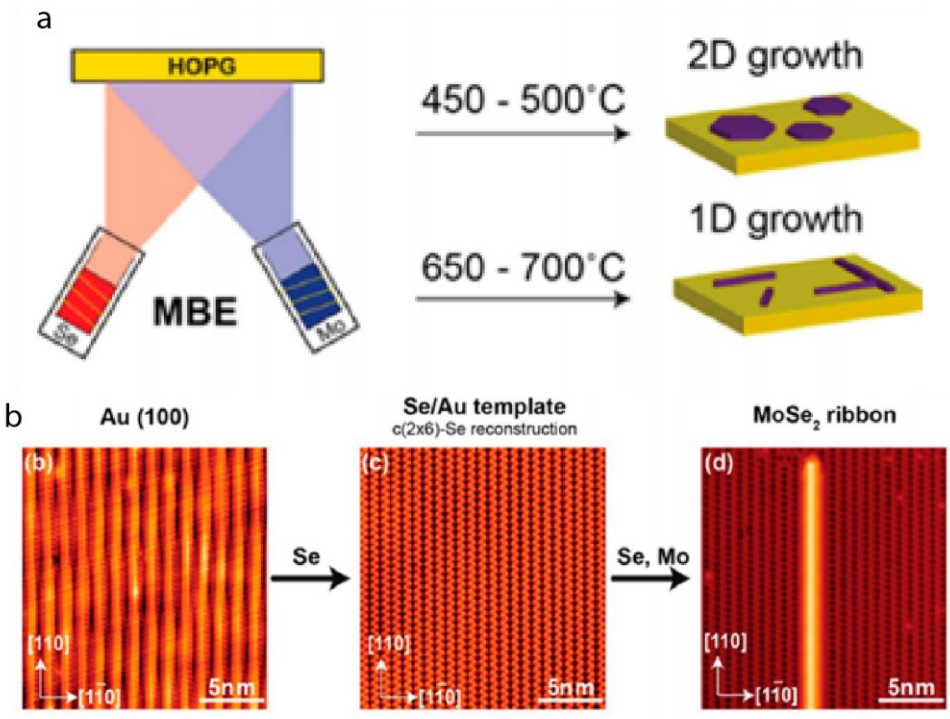

Figure 4.3. (a) Schematic illustrating the use of MBE techniques to evaporate Mo and Se atoms onto a substrate. Temperature control of the substrate induces either 2D or 1D growth.[44] (b) Scanning tunneling micrographs demonstrating the process of creating ultranarrow MoSe2 nanoribbons grown on Au (100) by evaporating Mo and Se atoms on to the surface.[45]

While those bottom-up methods were scalable but yielded lower quality material, these two methods yield exceptional materials with little to no avenues towards widespread adoption of the technique due to its instrumentation requirements. Though these methods allow probing of properties of $MoSe_2$ nanoribbon materials, the method used imparts characteristics onto the material as seen previously, such as edge structure, fidelity, width, aspect ratio, and surface orientation. To this end, more generalizable bottom-up methods towards

the selenide family of TMD nanoribbons is required. This work presents an important step in expanding the methods available to create selenide based one-dimensional TMDs. A generalized scheme showing the modulation of $MoSe_2$ nanoribbon morphology with varying growth conditions is shown (Fig. 4.4).

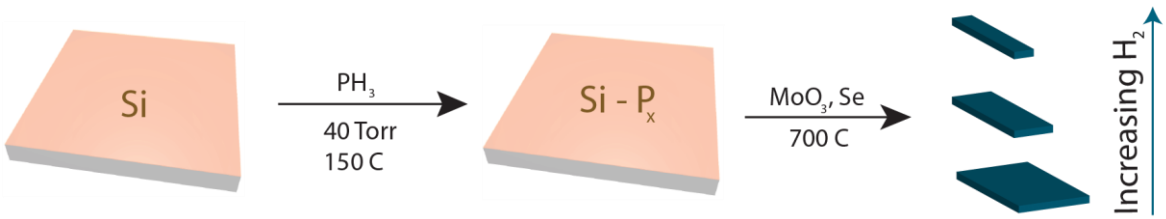

Figure 4.4. Generalized scheme showing the process of PH_3 functionalization at low temperatures to create a Si-P_x designer substrate as discussed in chapter 3. Second step shows the use of oxide and selenium powder at 700 °C to form $MoSe_2$ nanoribbon moieties that have decreasing widths with increasing H_2 during the growth.

The expansion of our novel designer growth techniques towards new chemical compositions not only will confirm the scalability and utility of this method, but potentially allow for planar 1D heterostructures that have not been synthesized through bottom-up methods previously. Lateral confinement of these nanoribbons alter the physical characteristics as discussed in the next chapter and undoubtedly will manifest in interesting ways in vertical heterostructures. However, the effect of extensive lateral confinement of inter layer excitons between two different material compositions have not been

explored. This synthetic breakthrough, coupled to the previous chapter's work, will allow the modulation of physical material morphology to study the effect of changing dimension on interlayer effects.

4.2 Experimental Methods

Preparation of Si–P_x Growth Substrates by PH_3 Treatment

Silicon wafers (Nova Electronic Materials, p-type 〈001〉, 0.001–0.005 Ω-cm, thickness 380 ± 25 μm SSP prime-grade Si wafers with two semi-standard flats and 2,000 Å ± 5% wet thermal oxide on both sides) were cut into individual substrates, each measuring ~ 2 × 2 cm^2. Substrates were then etched for 3 min in buffered hydrofluoric acid (BHF; Transene Company, 10% Buffer HF Improved) to remove all SiO_2 (etch rate of SiO_2 in 10% BHF, ~100 nm min^{-1}).

After etching, these Si substrates were immediately loaded into the quartz tube of our CVD system and the system was evacuated to its base pressure of 0.01 mtorr within 10 min. Next, our reactor was flushed for 15 min under a constant 50-sccm flow of nitrogen (Airgas, 6 N-grade nitrogen with built-in-purifier). Next, N_2 flow was ceased, and the reactor returned to base pressure within 2 min. Phosphine gas (Air Liquide, 20% PH_3 in He) was then introduced into the reactor at a flow rate of 20 sccm. The total reactor pressure was set to, and subsequently maintained at, 40 torr for the duration of the reaction

(P_{PH3} = 8 torr). The furnace temperature in all three zones was set to rise to 150 °C at a rate of 12.5 °C min^{-1}. Once the furnace temperature reached 150 °C, the reaction was allowed to proceed for 1 h under a constant flow of PH_3. After 1 h, PH_3 flow was stopped and the reactor was evacuated to base pressure. The reactor was then cooled to room temperature within 10 min, thereby ending the PH_3 treatment reaction.

Width Control

Si(001) substrates were treated with a total PH_3 gas dosage of 120 cm^3 for all widths. The CVD reactor temperature was 150 °C. The carrier gases introduced were N_2 and H_2. N_2 was held constant at 8 sccm while the flow of H_2 was increased from 2 sccm to 5 sccm and finally 8 sccm. The reactor pressure was held at 40 Torr for all reactions.

Synthesis of 1D $MoSe_2$ Crystals

The PH_3-treated Si substrate mentioned above was immediately loaded into a clean quartz tube containing molybdenum (VI) oxide (Strem Chemicals, 99.999%) and sulfur (Sigma-Aldrich). The solid precursors were contained within two alumina crucibles (MTI, high-purity 50 × 5 × 5 mm3 combustion boats) in the following quantities: (1) 0.010 g molybdenum (VI) oxide in one crucible, and (2) 0.140 g selenium in another. We controlled the position of the substrate and

solid-phase precursors relative to each other, and also relative to the three heated zones of the furnace. The central furnace zone (held at 700 °C during the reaction) housed the substrate, which was placed face-down over the crucible containing molybdenum (VI) oxide. The furnace zone upstream of the central zone (held at 700 °C during the reaction) housed the crucible containing selenium. The reactor was subjected to purging with N_2 prior to starting any reaction. This purge process and evacuation to base pressure was complete within 15 min. After reaching base pressure, the flow rate of N_2 was changed to 8 sccm and the furnace temperature was increased from room temperature to 700 °C at a rate of 84.4 °C min^{-1}, while pressure was maintained at 40 Torr. Once the furnace temperature had reached 700 °C, reactor total pressure was maintained at 40 torr and the reaction was allowed to proceed for 10 min at 700 °C. After 15 min, the reactor was rapidly cooled to room temperature under a 200-sccm flow of N_2, thereby ending the $MoSe_2$ reaction.

Scanning Electron Microscopy (SEM)

High-resolution SEMs were obtained on a Tescan Mira3 GMU SEM equipped with a field emission gun and Octane Plus silicon drift detectors for energy-dispersive X-ray spectroscopy analysis. ImageJ and MATLAB were used to perform statistical analyses of the SEM images of 1D $MoSe_2$ crystals to extract information on their yield and dimensions.

Theory

Cluster Expansion

Cluster expansions are generalized Ising models that account for many-body interactions[46]and are used here to predict the equilibrium structure of Si–P_x surfaces. For the slabs in this study, we assume that each site can be occupied by either a Si/P atom or a vacancy (only in the outmost layer) based on the (1 × 2) dimer-reconstructed cell, as it is known that dimers are formed on the Si(001) surface.[47] Cluster expansion allows for the incorporation of P atoms on the Si surface, their penetration into deeper layers and the formation of surface defects. We fit the cluster expansion to a set of training structures calculated using density functional theory (DFT)[48] using a Bayesian method that improves the predictive accuracy of the cluster expansion.[49] The training set contains randomly generated structures with varying P and vacancy concentrations. Ground-state structures predicted by the cluster expansion were added back to the training set to improve the quality of cluster expansion. For this cluster expansion, a total of 114 structures are in the training set and the root mean square leave-one-out cross-validation error is 5.4 meV per atom relative to DFT.

DFT

All DFT calculations were performed using the Vienna Ab initio Simulation Package (VASP).[50] For the Si–P-Vacancy cluster expansion, the revised Perdew–Burke–Ernzerhof[51] exchange-correlation functional was used. The Si_GW, P_GW and H_GW PBE projector-augmented wave potentials were used[52], and all VASP calculations were run with accurate precision. For the Si–P-Vacancy training set structures, the Brillouin zone was sampled using grids generated by the k-point grid server[53] with a mini-mum distance of 20 Å between real-space lattice points. Gaussian smearing with a width of 0.05 eV was used, and total energies were subsequently extrapolated to T = 0. The convergence criteria for the electronic self-consistent iteration and ionic relaxation loop were set to 10^{-4} and 10^{-3} eV, respectively.

Monte Carlo Simulations

Simulated annealing was performed to find the equilibrium structures of the Si-P_x surfaces. For each PH_3 partial pressure, Monte Carlo simulation[54] was run from a high temperature (1300 °C) and then decreased in steps by a factor of 40.05 until 150 °C. At each temperature, the number of Monte Carlo iteration was 1,440,000 on a 24x12 supercell. The chemical potential of P was adjusted by $kBT\ln(p / p^0)$, where T is the temperature, p is the PH3 partial pressure, and p^o is

the reference pressure. The thermodynamically averaged P coverage was recorded during the Monte Carlo sampling at 150 °C.

4.3 Discussion

As mentioned previously, there are both similarities and differences between MoS_2 and $MoSe_2$ 2D material synthesis. These differences also applies to the bottom-up gas phase synthesis of one-dimensional moieties of these TMDs. Both syntheses generally involve the heating of a Mo containing oxide and, at a lower temperature, the volatilization of the chalcogen in question. The ratio of Mo containing oxide and the chalcogen has been shown to be critical to formation of these materials, albeit different ratios are ideal for each material.[32] It is currently not known how the chalcogen and metal source ratio impacts the growth of one-dimensional moieties utilizing the designer substrate method and remains an open question.

However, there are several key differences in the synthesis of MoS_2 and $MoSe_2$ that greatly affect the ability to synthesize one-dimensional $MoSe_2$ compared to MoS_2. The chemical reactivity of Se is lower than that of S as a periodic trend. This necessitates the use of a reducing agent, in this case H_2, to facilitate the reduction of the parent MoO_3 material into $MoSe_2$.[4,31,33] In 2D synthesis of $MoSe_2$, H_2 gas is a common additive to the carrier gas. In 2D $MoSe_2$

growth, there is no issue with the addition of H_2 gas. However, the reduction environment likely has a negative impact on the designer surface (Si-P_x) environment. The P moieties on the surface, as discussed in Chapter 3, are likely very labile species that are extremely sensitive to their environment.[55] Though heating during the reaction undoubtedly damages the designer surface, as seen in temperature programmed desorption data, the addition of a strong reducing species further limits the effectiveness of the surface.[55] The original Si surface (after HF etching and before PH_3 introduction) is H-terminated Si.[56–60] When PH_3 is introduced into the chamber, some fraction of the H-terminated surface sites are chemical reacted to form a mixture P terminated Si sites and P-P bridging dimers. It should be noted that 2D MoS_2 has also been made within a H_2 or H_2S environments in many previous studies and understanding the role of H_2 may be advantageous not solely for the selenide family of TMDs.[61–64].

The rapid synthesis time of $MoSe_2$ compared to MoS_2 nanoribbon synthesis from chapter 3 (18 vs. 60 min) likely plays a crucial role in preserving the designer surface at our relevant temperatures (700 °C). Reaction trials using the same temperature ramp and hold times as the MoS_2 nanoribbons resulted in only bulk $MoSe_2$ material being formed. This result was consistent with long reaction times during the deposition of 2D $MoSe_2$ on SiO_2 as well where primarily bulk $MoSe_2$ crystals are observed. It is likely that long temperature

ramp times adversely impact the Si-P_x substrate and with the addition of H_2 degrades the surface towards H-terminated Si(001) beyond usability for substrate directed growth. Due to these observations we turned to shorter reaction times to preserve the Si-P_x surface.

By utilizing these conditions as outlined in section 4.2, we successfully synthesized $MoSe_2$ nanoribbons (Fig. 4.5). We note that the $MoSe_2$ nanoribbons share many similarities to MoS_2 nanoribbons from chapter 3. For instance, we see a high quality edge structure along the length of the nanoribbon and a leading edge termination that is consistent with one-dimensional MoS_2. However, when modulating the proportion of H_2 gas in our reactor during the growth of $MoSe_2$ we noticed that the morphology of these one-dimensional moieties was changed.

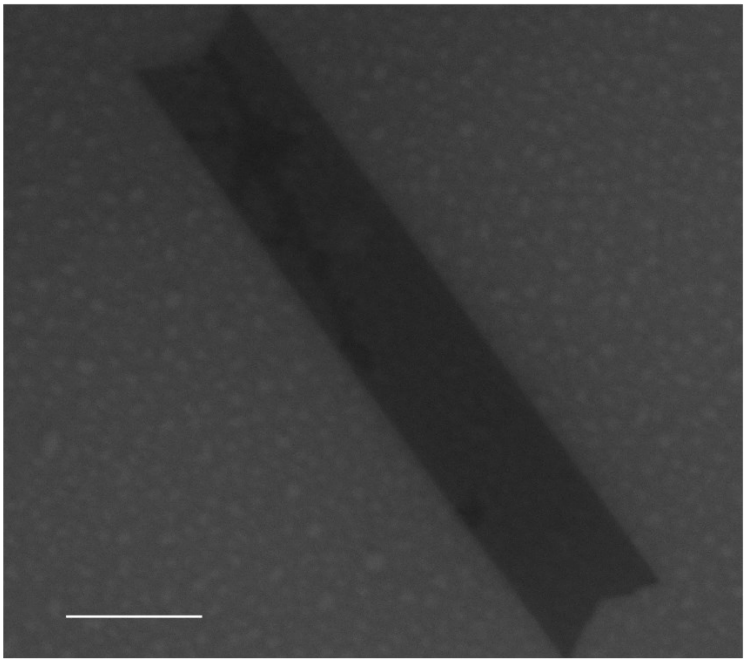

Figure 4.5. Scanning electron micrograph of a single $MoSe_2$ nanoribbon grown with 5 sccm of H_2 and 8 sccm of N_2 as the carrier gas. The edge structure appears similar to that of the MoS_2 nanoribbons from chapter 3. Scale bar, 500 nm.

To understand the overall effect that addition of H_2 gas in the carrier gas had on the product on the synthesis, we utilized three different N_2 to H_2 ratios for carrier gases while maintaining the same PH_3 dosage in the substrate treatment step. Fig. 4.6 shows low magnification SEM images of samples generated from the three different N_2 to H_2 ratios of 4:1, 8:5, and 1:1.

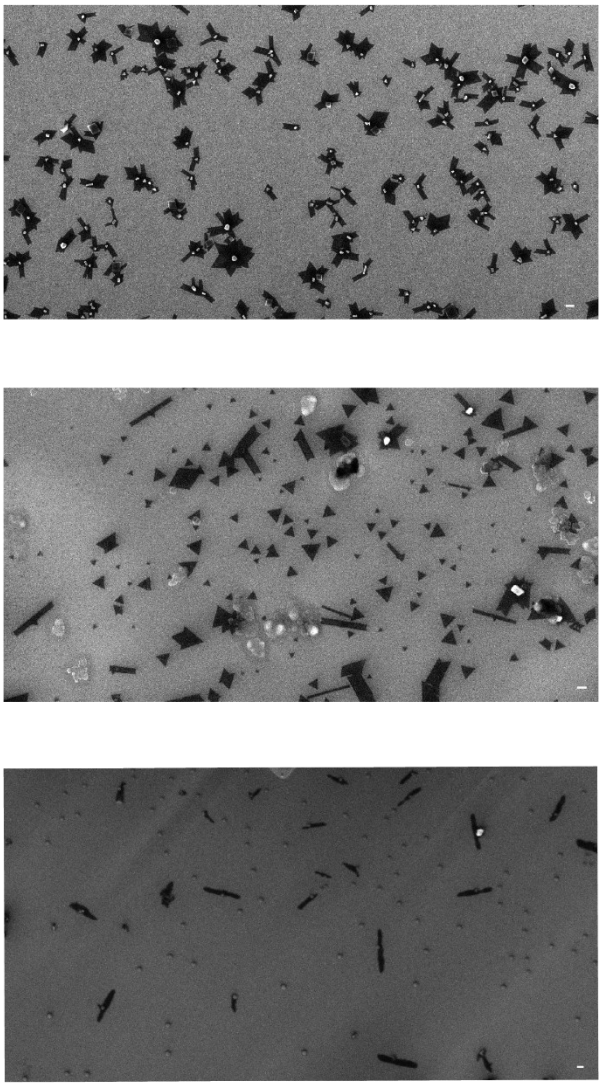

Figure 4.6. Representative low-magnification scanning electron micrographs of 1D $MoSe_2$ nanoribbons generated through chemical vapor deposition growth with different carrier gas ratios while maintaining the same PH_3 dose for the Si-P_x substrate. The carrier gas ratios were 1:4, 5:8, and 1:1 of H_2:N_2 from top to bottom respectively. Scale bars are 1 μm, 500 nm, 200 nm from top to bottom respectively.

We notice several features in these micrographs. First, these nanoribbons exhibit varying widths, lengths, and therefore, aspect ratios, which are discussed

later. Second, we notice the first indication that the concentration of H_2 will play an important role in the synthesis of these nanoribbons. In the 1:4 H_2 to N_2 gas ratio sample, many of the nanoribbon moieties have bulk $MoSe_2$ moieties on their seed regions. This is consistent with the reducing H_2 environment and earlier assertions regarding the limited reduction ability of Se. At lower H_2 concentrations, some of the MoO_3 material does not get reduced fast enough and vertical growth accompanies the lateral and directed growth observed. We notice some, but fewer, of these species in the 5:8 gas ratio sample in Fig. 4.5, and observe almost none in the 1:1 gas ratio consistent with this hypothesis. Lastly, the highest H_2 concentration synthesis yields a majority of nanoribbons that taper along their length, similarly to some of the randomly generated tapered samples from MoS_2 nanoribbon synthesis in the previous chapter. Notably this tapering effect appears to be more controllable by modulating the H_2 concentration in the reaction.

To probe the effect of H_2 concentration on the morphology of the nanoribbons, the widths, lengths, and aspect ratios were assayed using a high number of individual nanoribbons (N = 200). The first key quantity, width, is shown for the three conditions in Fig 4.7.

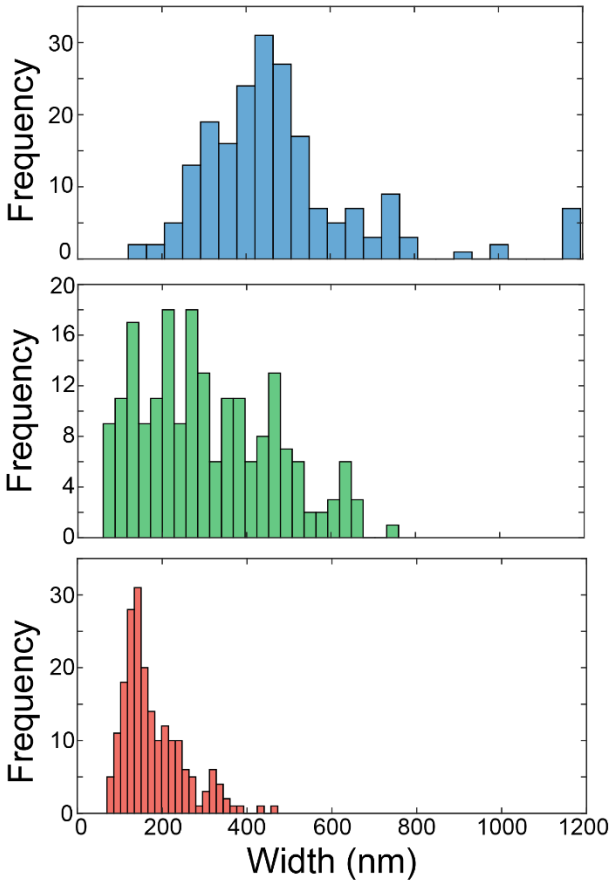

Figure 4.7. Width distributions for $MoSe_2$ nanoribbons synthesized using three discrete H_2:N_2 carrier gas ratios. N = 200. The average nanoribbon width from these distributions is 483 nm, 307 nm, and 174 nm from least to greatest H_2 content respectively.

We see a clear shift in the average width across these samples from 485 nm to 174 nm at the narrowest (highest H_2) sample. The distribution dispersion is fairly centered around the mean for both the highest and lowest H_2 content. The intermediate H_2 concentration does contain a significant dispersion with samples exhibiting extremely narrow and wider nanoribbons, but the majority of samples generated from this method are near the average of 307 nm. The narrowest

widths generated here are not as narrow as the limit achieved thus far in the synthesis of MoS_2 nanoribbons (50 nm average). However, we stress that the PH_3 dosage used in the narrowest condition in the previous chapter was 26 mL of PH_3 and this set of reactions utilized 60 mL of PH_3 which was the dosage that yielded, on average, 155 nm width MoS_2 nanoribbons. Controlling for PH_3 dosage, the $MoSe_2$ nanoribbons achieved remarkable similar nanoribbon widths compared to the MoS_2 synthesis. Additionally, the aspect ratios are greater at higher H_2 concentrations (Fig. 4.8). Though this phenomenon is not as well significantly correlated as width, further research into aspect ratio control will positively affect these quasi 1D materials for applied research for ease of integration with existing fabrication techniques. However, we note that the lowest H_2 concentration has by far the lowest average aspect ratio. This reinforces the earlier hypothesis that the lack of reduction due to limited H_2 caused vertical growth into bulk moieties and less Mo and Se atoms were directed along their nanoribbon growth front.

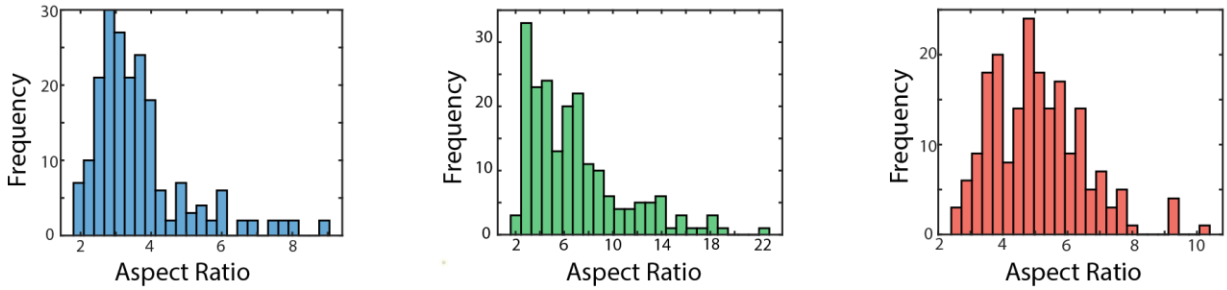

Figure 4.8. Aspect ratio distributions for $MoSe_2$ nanoribbons synthesized using three discrete H_2:N_2 carrier gas ratios. N = 200. The average nanoribbon width from these distributions is 3.7, 6.9, and 5.1 from least to greatest H_2 content respectively.

The inverse relationship between H_2 concentration and nanoribbon width is both intriguing and possibly technologically relevant. Obviously ultranarrow nanoribbons are ideal for technologies that seek to exploit strained edges and quantum confinement effects in a one dimensional moiety. In this work we sought to examine the extent to which this designer substrate method could be used in the generation of TMD nanoribbons. As H_2 gas is a necessary component to the selenide family of TMDs, it is imperative to understand the effect of H_2 on nanoribbon quality. Further, by understanding the effect H_2 exerts on this system, we will gain insights into how to adapt our designer substrate growths to varied low-dimensional material growth conditions.

The appearance of tapering is widely apparent in the highest H_2 concentration and required further investigation. We assayed several nanoribbons from each H_2 partial pressure synthesis and plotted the percent

change in their edge-to-edge width at a fixed distance along their length for each nanoribbon when starting at their midpoint as demonstrated in the scatterplots shown (Fig. 4.9).

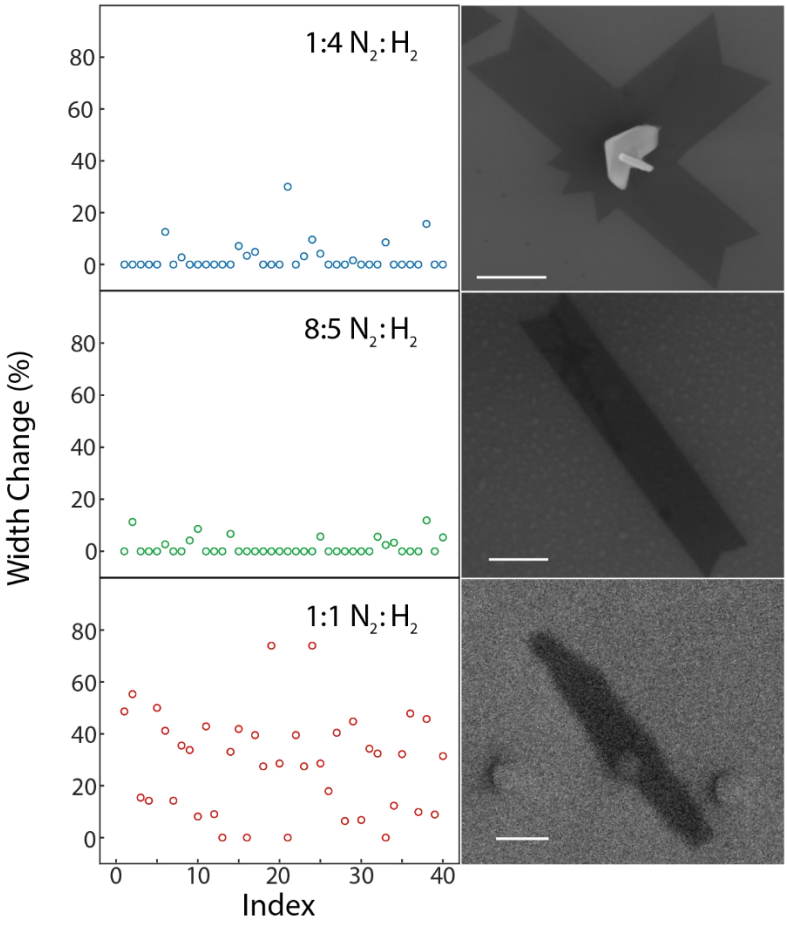

Figure 4.9. Scatterplots showing the percent change in the width from the central point of $MoSe_2$ nanoribbons to 350 nm longitudinally down the nanoribbon. N = 40. The three scatterplots correspond to the three different H_2:N_2 carrier gas ratios utilized to create significantly different width nanoribbons. Representative high magnification scanning electron micrographs of each condition accompany the scatterplots. Scale bars are 1 μm, 500 nm, 200 nm for the lowest H_2 to highest H_2 content in the carrier gas respectively.

In these scatter plots we note that the lowest and intermediate concentrations of H_2 in the carrier gas display little to no deviation of width in the aggregate. This is reinforced from Fig. 4.6 displaying low magnification micrographs of representative nanoribbons for each condition. However, when examining the highest H_2 concentration we note that the nanoribbons decidedly have much more tapering and width changing along their length. Further, we wanted to investigate whether this tapering effect was gradual or terraced. To this end, we recorded the retention of width as a function of length along the nanoribbon at four points along the nanoribbon (Fig. 4.10).

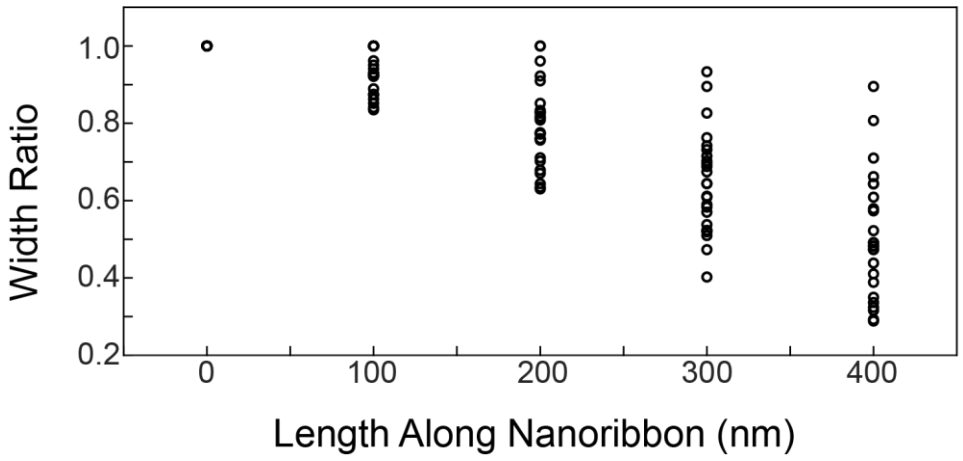

Figure 4.10. Scatterplot showing how the width of $MoSe_2$ nanoribbons changes from the central point of a nanoribbon up to 400 nm longitudinally along the nanoribbon for $MoSe_2$ nanoribbons synthesized at 1:1 H_2:N_2 conditions. On average, a generally gradual decline in the width along its length is observed. All nanoribbon widths at each point are normalized to their own width at their mid-point.

These data demonstrate that the tapering process is gradual on average. When compared to Fig. 5.3, we note that while the tapering on those MoS_2 nanoribbons were gradual, they were gradual in a different way. The process exhibited in those nanoribbons shows several terraced decreases in width where the edge structure at any given point is unchanging. These $MoSe_2$ nanoribbons shown in both Fig. 4.9 and Fig. 4.6 appear to have a smooth tapering over much of the length of the $MoSe_2$ nanoribbon moieties.

In the previous chapter we asserted a possible mechanism for the positive relationship between PH_3 dosage and nanoribbon width. In those conditions without H_2 gas we saw that less PH_3 directly lead to significantly narrower nanoribbons. Additionally, as discussed previously, the P-containing moieties on the Si surface are likely very labile and susceptible to abstraction by a reducing species. As hydrogen gas is a reducing agent, we can combine the previous assertion and this data to surmise that increasing H_2 concentration leads to less surface sites occupied by a P-containing moiety, whether that be Si-P dimers or P_2 dimers or P ad-atoms.

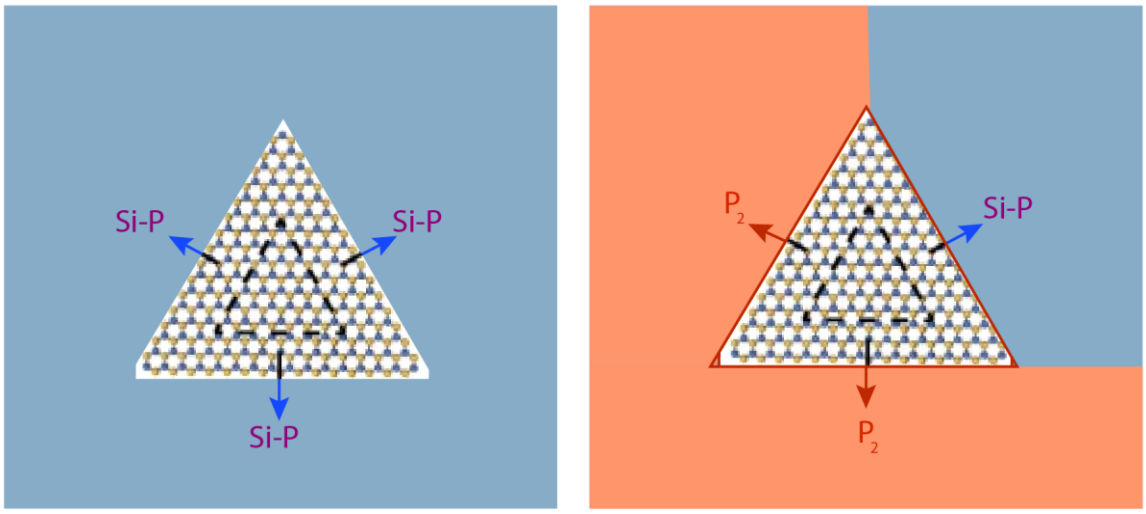

Figure 4.11. Schematic illustrating the proposed mechanism of growth of anisotropic TMD nanoribbons. In the left image the 2D seed is on a continuous domain of Si-P dimers and continues to grow isotropically. In the right image, two edges are interrupted in their growth by unfavorable P_2 dimer domains and growth only continues along one edge.

Fig. 4.11. illustrates a possible growth mechanism for when these P moieties are stripped by a reducing H_2 environment. Previous TPD studies confirm that P_2 dimers are the first species to be stripped thermally from the surface.[55] However, H_2 as a reductant is a complication in the mechanism of desorption that no prior work has examined in this context. We anticipate that H_2 reduction will affect P atoms incorporated in P_2 dimers, Si-P dimers, and singlet adsorbed P atoms. If this hypothesis is correct, then the domain sizes of all P containing moieties on the surface, such as Si-P dimers, are decreasing substantially. In this case, the size of the P_2 dimers are not as relevant as the diminishing size of the 2D $MoSe_2$ seed on a Si-P seed is relevant. As Fig. 4.11

illustrates, the hypothesis contests that as the 2D seed encounters an unfavorable surface, such as P_2, along any given edge of the 2D seed, that the seed will stop growing isotropically. When growth is either arrested or significantly hampered in those directions, any remaining surface of satisfactory crystal-substrate interaction energies, most likely Si-P dimers, will initiate an anisotropic directed growth that yields a TMD nanoribbon moiety.

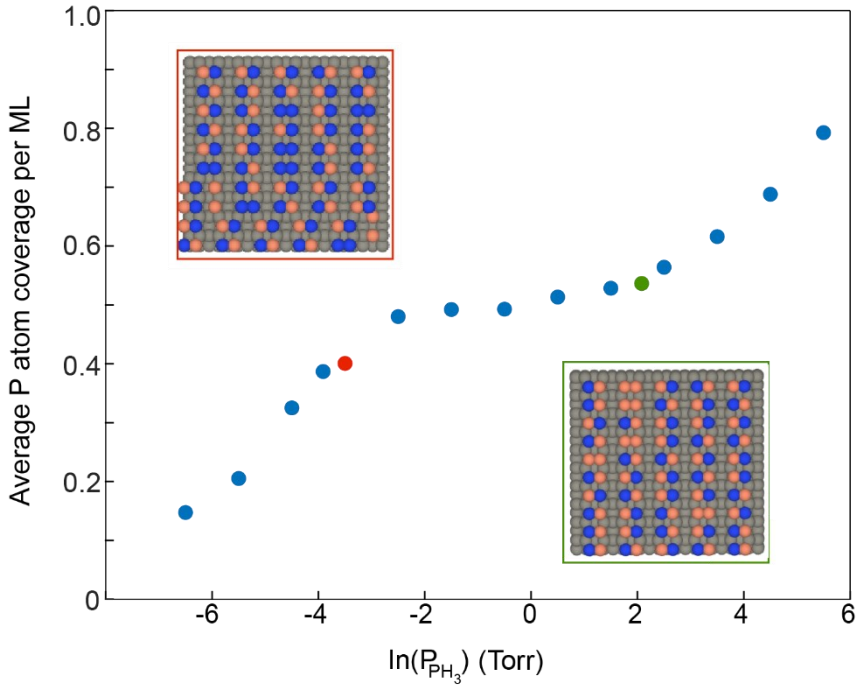

Figure 4.12. Scatterplot showing the average P atom coverage on a monolayer of Si (001) versus the PH_3 dose initiated on the surface at 150 °C determined from Monte Carlo calculations. Insets: Snapshots of the surface at two relevant PH_3 dosages conditions where their PH_3 dosage and overall P atom coverage is color coded with the surrounding box to its point in the scatterplot.

Calculations were employed to understand if this hypothesis was consistent with theoretical surface configurations. Cluster expansion calculations were used to determine the overall coverage of a monolayer of Si (001) that would be covered by P-containing moieties with the relevant conditions used here (Fig. 4.12). We note several features in this plot that are relevant at our reaction parameters. First, the relevant partial pressures of PH_3 in this reaction (8 Torr), lies at one of the two inflection points in the diagram. Second, when looking at relevant PH_3 dosages (0.01 – 8 Torr), the overall P atom coverage remains relatively unchanged for this segment of PH_3 dosages. This steady P percentage indicates a shift from Si-P formation towards P_2 dimer formation. In this case, it is likely that critical PH_3 dosages must be met to generate a sufficient number of P_2 dimer regions. However, we do note that it is currently unknown how different times of PH_3 dosages impact overall P coverage. At present, we do not know the exact interaction energies of $MoSe_2$ with different Si-P_x surface moieties like in MoS_2, but it can be assumed to be relatively the same between the three surface types discussed in Fig. 3.11. To a rough approximation, the green boxed simulation of P dispersion on the surface shown in Fig. 4.12 lies at the PH_3 dosage that was used in these reactions. The red boxed simulation of P dispersion on the surface is located at a significantly lowered PH_3 dose. Comparing these two simulations we notice that the lower dose PH_3 possess a

low concentration of native Si dimers that disappear when the moderately higher P atom coverage is accounted for. Additionally, the lower PH_3 dosage exhibits small amounts of singly adsorbed P atoms on the surface without dimerization. When examining the higher PH_3 dose, the simulation yields no Si dimers, no singly adsorbed P atoms. However, the simulation does introduce a significant fraction of P_2 dimers which were discussed in Chapter 3. Based on the hypothesis given in Fig. 4.11 and the density functional theory interaction energies in Fig. 3.11, we believe that the presence of P_2 dimers may be needed to create a heterogenous surface that is capable of significant nanoribbon growth. We note that in the case of MoS_2, at extremely low dosages, we noted disruption of the crystal growth but only insofar as it yielded serrated edges. More research is required to fully understand the surface dynamics at work in this system, but the proposed mechanism is consistent with observed results thus far.

This work lays the foundation for the designer substrate method of nanoribbon growth to become a ubiquitous method in one-dimensional TMD growth. By demonstrating the utility of this method to create multiple compositions of TMDs we have shown the applicability to many of the interesting heterostructure systems currently studied in 2D vertical heterostructures. Additionally, the control over nanoribbon morphology by H_2 concentration is a key finding that, when coupled to controlling the PH_3 dosages

in chapter 3, open up opportunities to combine methods for significant control over TMD nanoribbon moieties. With the expansion of this method and the ability to carefully tune nanoribbon widths, future work may assemble bottom-up grown nanoribbon vertical heterostructures utilizing many different TMD compositions.

4.4 References

(1) Li, S.; Lin, Y.-C.; Zhao, W.; Wu, J.; Wang, Z.; Hu, Z.; Shen, Y.; Tang, D.-M.; Wang, J.; Zhang, Q.; Zhu, H.; Chu, L.; Zhao, W.; Liu, C.; Sun, Z.; Taniguchi, T.; Osada, M.; Chen, W.; Xu, Q.-H.; Wee, A. T. S.; Suenaga, K.; Ding, F.; Eda, G. Vapour–Liquid–Solid Growth of Monolayer MoS_2 Nanoribbons. *Nat. Mater.* **2018**, *17* (6), 535–542.

(2) Fathipour, S.; Remskar, M.; Varlec, A.; Ajoy, A.; Yan, R.; Vishwanath, S.; Rouvimov, S.; Hwang, W. S.; Xing, H. G.; Jena, D.; Seabaugh, A. Synthesized Multiwall MoS_2 Nanotube and Nanoribbon Field-Effect Transistors. *Appl. Phys. Lett.* **2015**, *106* (2), 022114.

(3) Kotekar-Patil, D.; Deng, J.; Wong, S. L.; Lau, C. S.; Goh, K. E. J. Single Layer MoS_2 Nanoribbon Field Effect Transistor. *Appl. Phys. Lett.* **2019**, *114* (1), 013508.

(4) Chang, Y.-H.; Zhang, W.; Zhu, Y.; Han, Y.; Pu, J.; Chang, J.-K.; Hsu, W.-T.; Huang, J.-K.; Hsu, C.-L.; Chiu, M.-H.; Takenobu, T.; Li, H.; Wu, C.-I.; Chang, W.-H.; Wee, A. T. S.; Li, L.-J. Monolayer $MoSe_2$ Grown by Chemical Vapor Deposition for Fast Photodetection. *ACS Nano* **2014**, *8* (8), 8582–8590.

(5) Chen, S.-Y.; Zheng, C.; Fuhrer, M. S.; Yan, J. Helicity-Resolved Raman Scattering of MoS_2, $MoSe_2$, WS_2, and WSe_2 Atomic Layers. *Nano Lett.* **2015**, *15* (4), 2526–2532.

(6) Chen, J.; Zhao, X.; Tan, S. J. R.; Xu, H.; Wu, B.; Liu, B.; Fu, D.; Fu, W.; Geng, D.; Liu, Y.; Liu, W.; Tang, W.; Li, L.; Zhou, W.; Sum, T. C.; Loh, K. P. Chemical Vapor Deposition of Large-Size Monolayer $MoSe_2$ Crystals on Molten Glass. *J. Am. Chem. Soc.* **2017**, *139* (3), 1073–1076.

(7) Koperski, M.; Nogajewski, K.; Arora, A.; Cherkez, V.; Mallet, P.; Veuillen, J.-Y.; Marcus, J.; Kossacki, P.; Potemski, M. Single Photon Emitters in Exfoliated WSe_2 Structures. *Nat. Nanotechnol.* **2015**, *10* (6), 503–506.

(8) He, Y.-M.; Clark, G.; Schaibley, J. R.; He, Y.; Chen, M.-C.; Wei, Y.-J.; Ding, X.; Zhang, Q.; Yao, W.; Xu, X.; Lu, C.-Y.; Pan, J.-W. Single Quantum Emitters in Monolayer Semiconductors. *Nat. Nanotechnol.* **2015**, *10* (6), 497–502.

(9) Scheuschner, N.; Ochedowski, O.; Kaulitz, A.-M.; Gillen, R.; Schleberger, M.; Maultzsch, J. Photoluminescence of Freestanding Single- and Few-Layer MoS_2. *Phys. Rev. B* **2014**, *89* (12), 125406.

(10) Pradhan, N. R.; Rhodes, D.; Xin, Y.; Memaran, S.; Bhaskaran, L.; Siddiq, M.; Hill, S.; Ajayan, P. M.; Balicas, L. Ambipolar Molybdenum Diselenide Field-Effect Transistors: Field-Effect and Hall Mobilities. *ACS Nano* **2014**, *8* (8), 7923–7929.

(11) Abderrahmane, A.; Ko, P. J.; Thu, T. V.; Ishizawa, S.; Takamura, T.; Sandhu, A. High Photosensitivity Few-Layered $MoSe_2$ Back-Gated Field-Effect Phototransistors. *Nanotechnology* **2014**, *25* (36), 365202.

(12) Chamlagain, B.; Li, Q.; Ghimire, N. J.; Chuang, H.-J.; Perera, M. M.; Tu, H.; Xu, Y.; Pan, M.; Xaio, D.; Yan, J.; Mandrus, D.; Zhou, Z. Mobility Improvement and

Temperature Dependence in $MoSe_2$ Field-Effect Transistors on Parylene-C Substrate. *ACS Nano* **2014**, *8* (5), 5079–5088.
(13) Das, S. R.; Kwon, J.; Prakash, A.; Delker, C. J.; Das, S.; Janes, D. B. Low-Frequency Noise in $MoSe_2$ Field Effect Transistors. *Appl. Phys. Lett.* **2015**, *106* (8), 083507.
(14) Larentis, S.; Fallahazad, B.; Tutuc, E. Field-Effect Transistors and Intrinsic Mobility in Ultra-Thin $MoSe_2$ Layers. *Appl. Phys. Lett.* **2012**, *101* (22), 223104.
(15) Seyler, K. L.; Rivera, P.; Yu, H.; Wilson, N. P.; Ray, E. L.; Mandrus, D. G.; Yan, J.; Yao, W.; Xu, X. Signatures of Moiré-Trapped Valley Excitons in $MoSe_2/WSe_2$ Heterobilayers. *Nature* **2019**, *567* (7746), 66–70.
(16) Mak, K. F.; Shan, J. Photonics and Optoelectronics of 2D Semiconductor Transition Metal Dichalcogenides. *Nat. Photon.* **2016**, *10* (4), 216–226.
(17) Mak, K. F.; Xiao, D.; Shan, J. Light–Valley Interactions in 2D Semiconductors. *Nat. Photon.* **2018**, *12* (8), 451–460.
(18) Hanbicki, A. T.; Chuang, H.-J.; Rosenberger, M. R.; Hellberg, C. S.; Sivaram, S. V.; McCreary, K. M.; Mazin, I. I.; Jonker, B. T. Double Indirect Interlayer Exciton in a $MoSe_2/WSe_2$ van Der Waals Heterostructure. *ACS Nano* **2018**, *12* (5), 4719–4726.
(19) Wang, T.; Miao, S.; Li, Z.; Meng, Y.; Lu, Z.; Lian, Z.; Blei, M.; Taniguchi, T.; Watanabe, K.; Tongay, S.; Smirnov, D.; Shi, S.-F. Giant Valley-Zeeman Splitting from Spin-Singlet and Spin-Triplet Interlayer Excitons in $WSe_2/MoSe_2$ Heterostructure. *Nano Lett.* **2020**, *20* (1), 694–700.
(20) Norden, T.; Zhao, C.; Zhang, P.; Sabirianov, R.; Petrou, A.; Zeng, H. Giant Valley Splitting in Monolayer WS_2 by Magnetic Proximity Effect. *Nat. Commun.* **2019**, *10* (1), 4163.
(21) Kioseoglou, G.; Hanbicki, A. T.; Currie, M.; Friedman, A. L.; Jonker, B. T. Optical Polarization and Intervalley Scattering in Single Layers of MoS_2 and $MoSe_2$. *Sci. Rep.* **2016**, *6* (1), 25041.
(22) Lorchat, E.; Azzini, S.; Chervy, T.; Taniguchi, T.; Watanabe, K.; Ebbesen, T. W.; Genet, C.; Berciaud, S. Room-Temperature Valley Polarization and Coherence in Transition Metal Dichalcogenide–Graphene van Der Waals Heterostructures. *ACS Photon.* **2018**, *5* (12), 5047–5054.
(23) Kibsgaard, J.; Chen, Z.; Reinecke, B. N.; Jaramillo, T. F. Engineering the Surface Structure of MoS_2 to Preferentially Expose Active Edge Sites for Electrocatalysis. *Nat. Mater.* **2012**, *11* (11), 963–969.
(24) Jaramillo, T. F.; Jørgensen, K. P.; Bonde, J.; Nielsen, J. H.; Horch, S.; Chorkendorff, I. Identification of Active Edge Sites for Electrochemical H_2 Evolution from MoS_2 Nanocatalysts. *Science* **2007**, *317* (5834), 100–102.
(25) Chen, Z.; Cummins, D.; Reinecke, B. N.; Clark, E.; Sunkara, M. K.; Jaramillo, T. F. Core–Shell MoO_3–MoS_2 Nanowires for Hydrogen Evolution: A Functional Design for Electrocatalytic Materials. *Nano Lett.* **2011**, *11* (10), 4168–4175.
(26) Le, D.; Rawal, T. B.; Rahman, T. S. Single-Layer MoS_2 with Sulfur Vacancies: Structure and Catalytic Application. *J. Phys. Chem. C* **2014**, *118* (10), 5346–5351.

(27) Voiry, D.; Yang, J.; Chhowalla, M. Recent Strategies for Improving the Catalytic Activity of 2D TMD Nanosheets Toward the Hydrogen Evolution Reaction. *Adv. Mater.* **2016**, *28* (29), 6197–6206.
(28) Tonndorf, P.; Schmidt, R.; Böttger, P.; Zhang, X.; Börner, J.; Liebig, A.; Albrecht, M.; Kloc, C.; Gordan, O.; Zahn, D. R. T.; Vasconcellos, S. M. de; Bratschitsch, R. Photoluminescence Emission and Raman Response of Monolayer MoS_2, $MoSe_2$, and WSe_2. *Opt. Express, OE* **2013**, *21* (4), 4908–4916.
(29) Han, H.-V.; Lu, A.-Y.; Lu, L.-S.; Huang, J.-K.; Li, H.; Hsu, C.-L.; Lin, Y.-C.; Chiu, M.-H.; Suenaga, K.; Chu, C.-W.; Kuo, H.-C.; Chang, W.-H.; Li, L.-J.; Shi, Y. Photoluminescence Enhancement and Structure Repairing of Monolayer $MoSe_2$ by Hydrohalic Acid Treatment. *ACS Nano* **2016**, *10* (1), 1454–1461.
(30) Zhang, Y.; Chang, T.-R.; Zhou, B.; Cui, Y.-T.; Yan, H.; Liu, Z.; Schmitt, F.; Lee, J.; Moore, R.; Chen, Y.; Lin, H.; Jeng, H.-T.; Mo, S.-K.; Hussain, Z.; Bansil, A.; Shen, Z.-X. Direct Observation of the Transition from Indirect to Direct Bandgap in Atomically Thin Epitaxial $MoSe_2$. *Nat. Nanotechnol.* **2014**, *9* (2), 111–115.
(31) Shaw, J. C.; Zhou, H.; Chen, Y.; Weiss, N. O.; Liu, Y.; Huang, Y.; Duan, X. Chemical Vapor Deposition Growth of Monolayer $MoSe_2$ Nanosheets. *Nano Res.* **2014**, *7* (4), 511–517.
(32) Wang, S.; Rong, Y.; Fan, Y.; Pacios, M.; Bhaskaran, H.; He, K.; Warner, J. H. Shape Evolution of Monolayer MoS_2 Crystals Grown by Chemical Vapor Deposition. *Chem. Mater.* **2014**, *26* (22), 6371–6379.
(33) Wang, X.; Gong, Y.; Shi, G.; Chow, W. L.; Keyshar, K.; Ye, G.; Vajtai, R.; Lou, J.; Liu, Z.; Ringe, E.; Tay, B. K.; Ajayan, P. M. Chemical Vapor Deposition Growth of Crystalline Monolayer $MoSe_2$. *ACS Nano* **2014**, *8* (5), 5125–5131.
(34) Coelho, P. M.; Komsa, H.-P.; Coy Diaz, H.; Ma, Y.; Krasheninnikov, A. V.; Batzill, M. Post-Synthesis Modifications of Two-Dimensional $MoSe_2$ or $MoTe_2$ by Incorporation of Excess Metal Atoms into the Crystal Structure. *ACS Nano* **2018**, *12* (4), 3975–3984.
(35) Abbas, A. N.; Liu, G.; Liu, B.; Zhang, L.; Liu, H.; Ohlberg, D.; Wu, W.; Zhou, C. Patterning, Characterization, and Chemical Sensing Applications of Graphene Nanoribbon Arrays Down to 5 nm Using Helium Ion Beam Lithography. *ACS Nano* **2014**, *8* (2), 1538–1546.
(36) Tapasztó, L.; Dobrik, G.; Lambin, P.; Biró, L. P. Tailoring the Atomic Structure of Graphene Nanoribbons by Scanning Tunnelling Microscope Lithography. *Nat. Nanotechnol.* **2008**, *3* (7), 397–401.
(37) Huang, W.; Wang, X.; Ji, X.; Zhang, Z.; Jin, C. In-Situ Fabrication of Mo_6S_6-Nanowire-Terminated Edges in Monolayer Molybdenum Disulfide. *Nano Res.* **2018**, *11* (11), 5849–5857.
(38) Bai, Y.; Zhou, L.; Wang, J.; Wu, W.; McGilly, L. J.; Halbertal, D.; Lo, C. F. B.; Liu, F.; Ardelean, J.; Rivera, P.; Finney, N. R.; Yang, X.-C.; Basov, D. N.; Yao, W.; Xu, X.; Hone, J.; Pasupathy, A. N.; Zhu, X.-Y. Excitons in Strain-Induced One-Dimensional Moiré Potentials at Transition Metal Dichalcogenide Heterojunctions. *Nat. Mater.* **2020**, 1–6.

(39) Choi, J.; Hsu, W.-T.; Lu, L.-S.; Sun, L.; Cheng, H.-Y.; Lee, M.-H.; Quan, J.; Tran, K.; Wang, C.-Y.; Staab, M.; Jones, K.; Taniguchi, T.; Watanabe, K.; Chu, M.-W.; Gwo, S.; Kim, S.; Shih, C.-K.; Li, X.; Chang, W.-H. Moiré Potential Impedes Interlayer Exciton Diffusion in van Der Waals Heterostructures. *Sci. Adv.* **2020**, *6* (39), eaba8866.
(40) Tran, K.; Moody, G.; Wu, F.; Lu, X.; Choi, J.; Kim, K.; Rai, A.; Sanchez, D. A.; Quan, J.; Singh, A.; Embley, J.; Zepeda, A.; Campbell, M.; Autry, T.; Taniguchi, T.; Watanabe, K.; Lu, N.; Banerjee, S. K.; Silverman, K. L.; Kim, S.; Tutuc, E.; Yang, L.; MacDonald, A. H.; Li, X. Evidence for Moiré Excitons in van Der Waals Heterostructures. *Nature* **2019**, *567* (7746), 71–75.
(41) Xu, Y.; Horn, C.; Zhu, J.; Tang, Y.; Ma, L.; Li, L.; Liu, S.; Watanabe, K.; Taniguchi, T.; Hone, J. C.; Shan, J.; Mak, K. F. Creation of Moiré Bands in a Monolayer Semiconductor by Spatially Periodic Dielectric Screening. *Nat. Mater.* **2021**, 1–5.
(42) Yu, H.; Liu, G.-B.; Tang, J.; Xu, X.; Yao, W. Moiré Excitons: From Programmable Quantum Emitter Arrays to Spin-Orbit–Coupled Artificial Lattices. *Sci. Adv.* **2017**, *3* (11), e1701696.
(43) Wei, Y.; Hu, C.; Li, Y.; Hu, X.; Yu, K.; Sun, L.; Hohage, M.; Sun, L. Initial Stage of MBE Growth of $MoSe_2$ Monolayer. *Nanotechnology* **2020**, *31* (31), 315710.
(44) Chen, Y.; Cui, P.; Ren, X.; Zhang, C.; Jin, C.; Zhang, Z.; Shih, C.-K. Fabrication of $MoSe_2$ Nanoribbons via an Unusual Morphological Phase Transition. *Nat. Commun.* **2017**, *8* (1), 15135.
(45) Cheng, F.; Xu, H.; Xu, W.; Zhou, P.; Martin, J.; Loh, K. P. Controlled Growth of 1D $MoSe_2$ Nanoribbons with Spatially Modulated Edge States. *Nano Lett.* **2017**, *17* (2), 1116–1120.
(46) Sanchez, J. M.; Ducastelle, F.; Gratias, D. Generalized Cluster Description of Multicomponent Systems. *Physica A* **1984**, *128* (1), 334–350.
(47) Wang, Y.; Chen, X.; Hamers, R. J. Atomic-Resolution Study of Overlayer Formation and Interfacial Mixing in the Interaction of Phosphorus with Si(001). *Phys. Rev. B* **1994**, *50* (7), 4534–4547.
(48) Kohn, W.; Sham, L. J. Self-Consistent Equations Including Exchange and Correlation Effects. *Phys. Rev.* **1965**, *140* (4A), A1133–A1138.
(49) Mueller, T.; Ceder, G. Bayesian Approach to Cluster Expansions. *Phys. Rev. B* **2009**, *80* (2), 024103.
(50) Kresse, G.; Hafner, J. Ab Initio Molecular Dynamics for Liquid Metals. *Phys. Rev. B* **1993**, *47* (1), 558–561.
(51) Hammer, B.; Hansen, L. B.; Nørskov, J. K. Improved Adsorption Energetics within Density-Functional Theory Using Revised Perdew-Burke-Ernzerhof Functionals. *Phys. Rev. B* **1999**, *59* (11), 7413–7421.
(52) Blöchl, P. E. Projector Augmented-Wave Method. *Phys. Rev. B* **1994**, *50* (24), 17953–17979.
(53) Wisesa, P.; McGill, K. A.; Mueller, T. Efficient Generation of Generalized Monkhorst-Pack Grids through the Use of Informatics. *Phys. Rev. B* **2016**, *93* (15), 155109.

(54) Metropolis, N.; Rosenbluth, A. W.; Rosenbluth, M. N.; Teller, A. H.; Teller, E. Equation of State Calculations by Fast Computing Machines. *J. Chem. Phys.* **1953**, *21* (6), 1087–1092.
(55) Cho, B.; Bareño, J.; Foo, Y. L.; Hong, S.; Spila, T.; Petrov, I.; Greene, J. E. Phosphorus Incorporation during Si(001):P Gas-Source Molecular Beam Epitaxy: Effects on Growth Kinetics and Surface Morphology. *J. Appl. Phys.* **2008**, *103* (12), 123530.
(56) Dai, M.; Wang, Y.; Kwon, J.; Halls, M. D.; Chabal, Y. J. Nitrogen Interaction with Hydrogen-Terminated Silicon Surfaces at the Atomic Scale. *Nat. Mater.* **2009**, *8* (10), 825–830.
(57) Fenner, D. B.; Biegelsen, D. K.; Bringans, R. D. Silicon Surface Passivation by Hydrogen Termination: A Comparative Study of Preparation Methods. *J. Appl. Phys.* **1989**, *66* (1), 419–424.
(58) M'saad, H.; Michel, J.; Reddy, A.; Kimerling, L. C. Monitoring and Optimization of Silicon Surface Quality. *J. Electrochem. Soc.* **1995**, *142* (8), 2833.
(59) Dumas, P.; Chabal, Y. J.; Jakob, P. Morphology of Hydrogen-Terminated Si(111) and Si(100) Surfaces upon Etching in HF and Buffered-HF Solutions. *Surf. Sci.* **1992**, *269–270*, 867–878.
(60) Watanabe, S.; Nakayama, N.; Ito, T. Homogeneous Hydrogen-terminated Si(111) Surface Formed Using Aqueous HF Solution and Water. *Appl. Phys. Lett.* **1991**, *59* (12), 1458–1460.
(61) Endler, I.; Leonhardt, A.; König, U.; van den Berg, H.; Pitschke, W.; Sottke, V. Chemical Vapour Deposition of MoS_2 Coatings Using the Precursors $MoCl_5$ and H_2S. *Surf. Coat. Tech.* **1999**, *120–121*, 482–488.
(62) Kim, Y.; Bark, H.; Ryu, G. H.; Lee, Z.; Lee, C. Wafer-Scale Monolayer MoS_2 grown by Chemical Vapor Deposition Using a Reaction of MoO_3 and H_2S. *J. Phys.: Condens. Matter* **2016**, *28* (18), 184002.
(63) Li, Q.; Newberg, J. T.; Walter, E. C.; Hemminger, J. C.; Penner, R. M. Polycrystalline Molybdenum Disulfide (2H−MoS_2) Nano- and Microribbons by Electrochemical/Chemical Synthesis. *Nano Lett.* **2004**, *4* (2), 277–281.
(64) Dumcenco, D.; Ovchinnikov, D.; Sanchez, O. L.; Gillet, P.; Alexander, D. T. L.; Lazar, S.; Radenovic, A.; Kis, A. Large-Area MoS_2 Grown Using H_2S as the Sulphur Source. *2D Mater.* **2015**, *2* (4), 044005.

Chapter 5: Properties of Dimensionally Restricted Transition Metal Dichalcogenide Materials

The work presented in this chapter has been published as:

T. Chowdhury, J. Kim, E. C. Sadler, C. Li, S.-W. Lee, K. Jo, W. Xu, D. H. Gracias, N. V. Drichko, D. Jariwala, T. H. Brintlinger, T. Mueller, H.-G. Park, and T. J. Kempa. "Substrate-Directed Synthesis of MoS_2 nanocrystals with Tunable Dimensionality and Optical Properties"

Nat. Nanotechnol. **15**, 29-34 (2020)

And

E. C. Sadler, T. Chowdhury, R. Dziobek-Garrett, Li, C. T. Mueller, T. J. Kempa "Substrate Templated Synthesis of $MoSe_2$ Nanoribbons"

Submitted to ACS Applied Materials and Interfaces

5.1 Introduction

One dimensional TMDs present unique physical properties not encountered in their two-dimensional cousins. The two primary forms of 1D TMDs, nanotubes and nanoribbons each present unique properties and

opportunities. For example, 1D TMD nanotubes exhibit chirality and radius of curvature dependent properties due to their cylindrical nature that are not present in nanoribbons.[1–5] Nanotubes have seen applications in a variety of fields including catalysis, photodetection, electronics and other applications that take advantage of the useful and unique properties in nanotube morphologies. [4,6–8]

However, this work focuses on one-dimensional nanoribbons which do not host phenomena based on their curvature but do present unique properties due to their increased lateral confinement and prominent edge states that host a litany of attractive features. These edges can assume zigzag or armchair configurations that impart unique electrical or magnetic properties than compared to the other edge configuration.[9–11] For example, theory has suggested that ultranarrow TMD nanoribbons are of metallic character, compared to the semiconducting and much larger domains of 2D TMD crystals, high thermoelectric performance, and more.[9,12–16] Experimental work agrees that TMD nanoribbons possess features which are unique and useful to nanoribbon morphologies. One such phenomena is the observed crossover point due to changing width can be observed for metallic to semiconducting transition in TMD nanoribbons.[17]

Not just confined to electrical modification, magnetic properties may be influenced by the width of TMD nanoribbons. Previous calculations have

predicted rising ferromagnetism in 1T' phase MoS_2 nanoribbons due to edge reconstructions, with the magnitude of the magnetic moment dependent upon the width.[9,13,15,18–23] Further, TMD nanoribbons may hold topological excitonic phenomena. More research into how defects, edges, and confinement affect physical phenomena is needed.

As mentioned in the last two chapters, the goal of producing scalable TMD nanoribbons of high edge quality with tunability was and is a goal of the TMD community, especially to better understand the nascent work done recently to uncover particularly intriguing aspects of one-dimensional TMDs. As reported in the previous chapters, the Kempa group has designed a novel method to tackle the challenge in the search for 1D MoS_2 and $MoSe_2$ nanoribbons. However, the properties of these nanoribbons due to their restricted dimensionality needs to be examined. Nominally, 1D materials owe much of their differing physical characteristics compared to 2D cousins from their greater edge to basal plane ratio, narrow widths, and edge configurations. Understanding how our method influenced these parameters is key in understanding the applicability of this method towards technologically viable TMD nanoribbons.

Previous work on 1D TMDs have utilized TMDs in the morphologies such as nanotubes and nanoribbons, with each imparting different physical properties. These properties include optical anisotropy due to their

morphological anisotropy, different electronic responses, and generation of high catalytic currents (Fig. 5.1).[3,24,25] These applications have used both nanotubes and nanoribbon morphologies. Due to these myriad advantageous physical properties in one-dimensional TMDs, it behooves us to understand how bottom-up grown planar MoS_2 nanoribbon crystals behave. In this chapter, we explore physical characterization of nanoribbons created through the novel designer substrate method discussed in chapters 3 and 4. We investigate structure, phase, optical emission, electrical properties and edge structure.

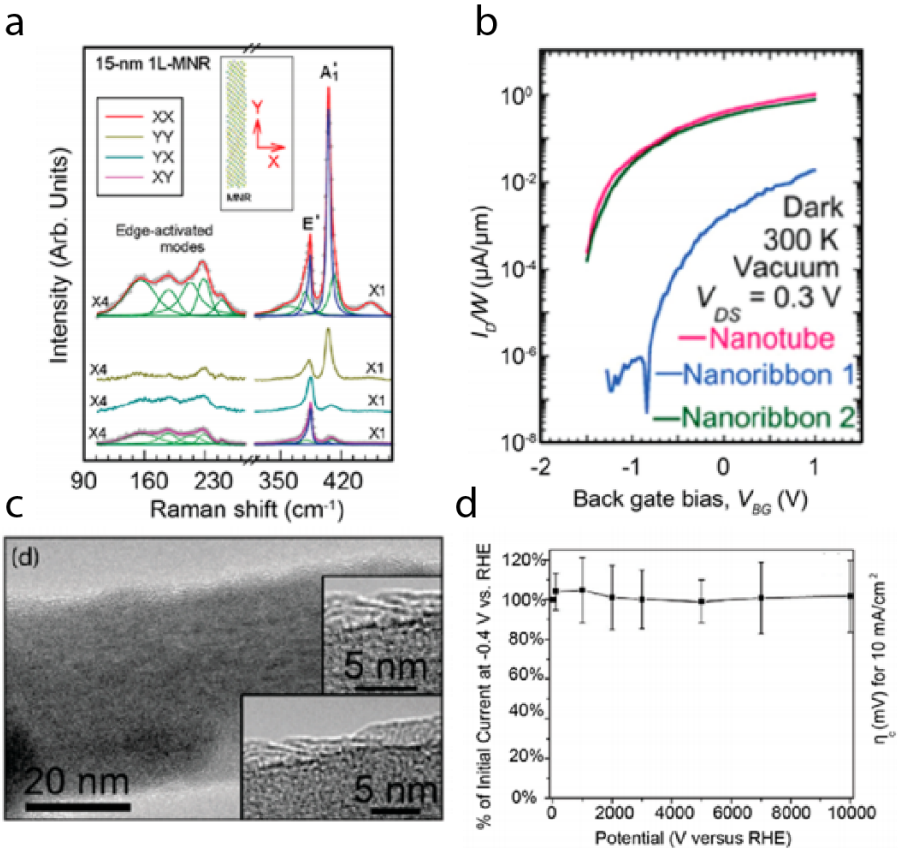

Figure 5.1. (a) Optical anisotropy in Raman signatures generated from incident light grazing the sample in different directions.[25] (b) TMD 1D nanotubes and nanoribbons exhibiting transiting behavior that behave both different from their 2D morphology and from each other.[3] (c) Transmission electron micrograph showing a core-shell nanotube morphology with a TMD shell for catalytic stability and activity.[24] (d) Plot showing current retention percentage and current density as a function of potential for the core-shell moiety shown in (c).

5.2 Experimental Methods

Aberration-Corrected (Cs) STEM

Before Cs-STEM characterization, TEM grids were transferred to sample cartridges and then baked in a vacuum (<1×10^{-6} torr) at 120 °C for 14 h. Next, the sample cartridges were transferred to the microscope column with < 1 min exposure to ambient conditions. The Cs-STEM (Nion, UltraSTEM-200X) was first aligned and then aberrations were removed using a 'standard' sample of gold evaporated on carbon. After this alignment and Cs-correction step, the TEM grids containing 1D MoS_2 crystals were inserted into the column for imaging. All images were collected using the microscope's HAADF detector, with the microscope operating at 60 kV and correction taken to the fifth order and 60 mrad. The STEM probe size was 130 pm. Shear transformation was performed by first estimating the coarse drift through measurement of distortion in the FFT (fast Fourier transform) pattern. Further refinement of the shear transformation matrix was performed by minimizing variance in the distances of the most intense FFT spots as obtained through iterative application of different affine transformations.

Raman and PL Spectroscopy

Micro-Raman scattering measurements were collected in a back-scattering geometry using a Horiba Jobin Yvon T46000 spectrometer equipped with a liquid N_2-cooled charge-coupled device detector in a single monochromator configuration. The excitation source was an $Ar^+/Kr-$ coherent laser operating at 514 nm and power of 1 mW. A ×50 objective lens was used. The laser probe size was ~2 μm. Raman spectra in the range 200–800 cm^{-1} were obtained using a spectral resolution of 2 cm^{-1}. Photoluminescence spectra in the range 500–800 nm were obtained with a spectral resolution of 0.2 nm. Horiba's proprietary DuoScan system was operated in stepper mode to map Raman and PL intensities within an area of interest encompassing <10 × 10 μm^2. Using this acquisition mode, the laser probe size and spatial resolution were ~1 μm and the spectral resolution was 1 nm. Time-dependent measurements were also carried out using the DuoScan system. All measurements were performed at room temperature and ambient pressure. Peak positions were extracted from Gaussian fits to the raw PL data performed in MATLAB.

2D Micro-PL Mapping

Micro-PL measurements were conducted on 1D MoS_2 crystals, which were transferred to SiO_2 on Si substrates using the protocol described in Transfer of 1D MoS_2 crystals to TEM grids, above. The samples were scanned with a continuous-wave green laser ($\lambda = 532$ nm), whose position over the sample was precisely controlled by a dual-axis scanning galvo system (Thorlabs). The PL signal was collected by a ×100/0.90 numerical aperture objective lens. The pump laser was excluded from the PL signal by a 532-nm high-pass filter. The collected PL signal was focused onto a single-mode fiber. A 50/50 fiber beam-splitter was used to direct the fiber-coupled light either to a spectrometer (Princeton Instruments, Acton SP2500) with a 300 lines mm^{-1} grating and silicon charge-coupled device or to the avalanche photodiode. Photoluminescence spectra were integrated over 5 min.

Near-Field PL Mapping

Near-field PL mapping was performed using an OmegaScope-R SPM (AIST-NT, now Horiba Scientific) coupled to a LabRAM HR Evolution Raman Spectrometer (Horiba Scientific). An Ag-coated OMNI-TERS probe covered by a protective layer (Horiba Scientific) was employed for near-field PL imaging. The samples were scanned with a laser, $\lambda_{excitation} = 633$ nm, with the power on the tip

being maintained at ~500 μW. The PL map in Fig. 5.11 (a) was obtained using a grating with 100 lines mm^{-1} and an integration time of 1 s per pixel. The PL spectra in Fig. 5.12 (b) were obtained using a grating with 600 lines mm^{-1} and an integration time of 5 min.

Crystal Transfer

One-dimensional MoS_2 crystals were transferred to SiO_2/Si substrates as follows. A PMMA (MicroChem, C6 resist) layer was deposited on a Si substrate containing as-grown 1D MoS_2 crystals by spin-coating at 4,000 r.p.m. for 40 s. The crystals were released from the Si substrate by etching in KOH solution for several hours at 70 °C. The 1D MoS_2 crystals remain adhered to the PMMA film as it floats on the surface of the KOH solution. This PMMA film, with attached crystals, was transferred to a dish of deionized water for rinsing, then transferred again to the device substrate (SiO_2/Si) and finally completely dried. Once dry, the PMMA layer was selectively removed by dipping the device substrate in acetone for 10 min.

Field Effect Transistor (FET) Fabrication

Electrical contacts (Ti (adhesion layer), 5 nm; Au (contact layer), 50 nm) were patterned over the 1D crystals by electron-beam lithography and then deposited through thermal evaporation. First, a PMMA (C6) layer was deposited

over the device substrates containing the 1D crystals by spin-coating at 4,000 r.p.m. for 40 s. The resists were subjected to baking at 280 °C for 150 s after the coating step. The contact patterns were defined by electron-beam lithography (JEOL, JSF-7001F) followed by resist development and rinsing in methyl isobutyl ketone and isopropyl alcohol for 90 and 30 s, respectively. A 5-nm-thick Ti adhesion layer followed by a 50-nm-thick Au layer was deposited by thermal evaporation. Residual metal lift-off was performed in acetone over 10 min.

Atomic Force Microscopy (AFM)

The height and topography of both 1D and 2D MoS_2 nanocrystals were measured on a Keysight 5500 AFM using an Al-coated Si probe tip (TAP190AL-G-10). AFM imaging was carried out in non-contact mode to prevent damage to, and unintentional displacement of, the atomically thin crystals during scanning. AFM raw images (.mi) were processed in Gwyddion 2.51. A second-order polynomial correction was applied to subtract background noise in the raw image. A three-point levelling with an averaging radius of five pixels was applied to correct for a linear offset across the whole image.

X-Ray Photoelectron Spectroscopy (XPS)

A sample of as-grown 1D MoS_2 crystals was analyzed in a PHI 5600 system under ultra-high-vacuum conditions (<10–8 torr). A Mg-Kα source

(1,253.6 eV) operating at 300 W and 15 kV was used to generate X-rays. The kinetic energy (in eV) of the ejected photoelectrons was measured using a hemispherical energy analyzer operating at a constant pass energy of 58.7 eV. The spot size of the incident X-ray beam was $0.8 \times 2.0\ mm^2$. The step-size of the measurement was 0.125 eV. The relative atom percentage concentration of the constituent elements was analyzed by taking into account the atomic sensitivity factors for the X-ray source inclined at 54.7°.

Transfer of 1D MoS_2 crystals to TEM grids

One-dimensional MoS_2 crystals grown on PH_3-treated Si substrates were transferred to TEM grids as follows. Spin-coating (spin speed, 2,500 r.p.m.; spin time, 60 s; acceleration time, 5 s) was used to deposit a layer of poly(methyl methacrylate) (PMMA;Sigma-Aldrich, MW ~996,000) over the 1D MoS_2 crystals residing on their Si–P_x growth substrates. The PMMA-coated sample was then baked at 135 °C for 15 min and transferred face-up onto the surface of a 1-M KOH solution. The solution was heated to, and maintained at, a temperature of 60 °C. After ~ 2 h, complete etching by KOH of the underlying Si substrate allowed the PMMA film to delaminate and float on the surface of the solution. The majority of the 1D MoS_2 crystals remained adhered to the PMMA film. The delaminated PMMA film was washed several times with de-ionized water by transferring it between beakers. Next, the PMMA film was extracted onto the

surface of a TEM specimen support grid (Quantifoil substrate, 658-300-AU, Ted-Pella) by holding the grid with a pair of fine inversion tweezers and using it to gather the floating PMMA film onto it. The TEM grid sample was allowed to dry in air. Special care must be taken during the extraction step to minimize damage to the atomically thin 1D MoS_2 crystals. Finally, the TEM grid was placed in a furnace and annealed at 450 °C for 4 h under an Ar atmosphere. This step is effective at removing PMMA without distorting the original morphology of the MoS_2 crystals.

Transistor Property Measurement

The fabricated FET devices were mounted to an x–y-translation stage, which is part of our home-built device characterization micro-probe station. The substrate back-side gate electrode was connected using silver paste. The devices were connected via Au-plated W probes and triax cables to an ultra-low-noise semiconductor parameter analyzer (Agilent, 4156C). The device drain current was recorded as a function of the applied back-side gate voltage.

5.3 Discussion

Scanning electron micrographs show a straight edge structure of MoS_2 nanoribbons with low-magnification images are shown in Fig 5.2. These nanoribbons offer pristine edge structures and confined dimensions to study various phenomena.

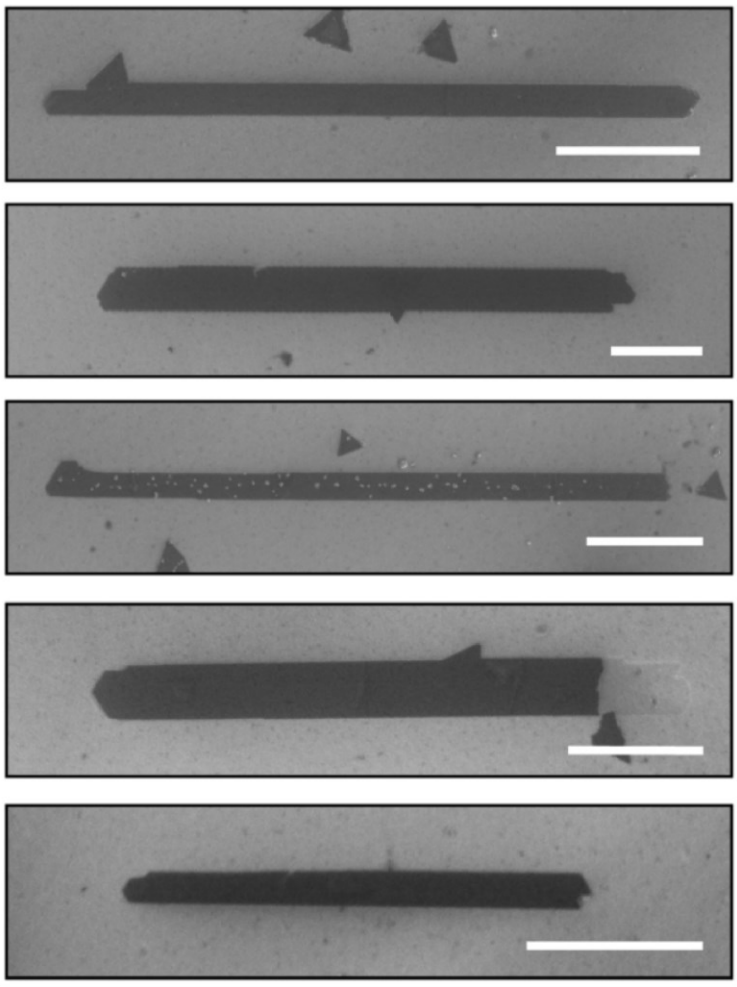

Figure 5.2. Gallery of high magnification scanning electron micrographs depicting several single MoS_2 nanoribbons. Crystals exhibit uniform width along their length. Scale bars, 1 μm.

Regions of interest on these samples can yield high amount of sample of a relatively narrow distribution of nanoribbons as discussed more explicitly for $MoSe_2$ nanoribbons in chapter 4. Several candidate micrographs are shown under high magnification (Fig. 5.2). However, some conditions upset the straight, high-quality edges exhibited in most of the nanoribbons as discussed in chapters 3 and 4. Occasionally, tapered nanoribbons are derived from the synthesis of majority smooth edge candidates (Fig. 5.3).

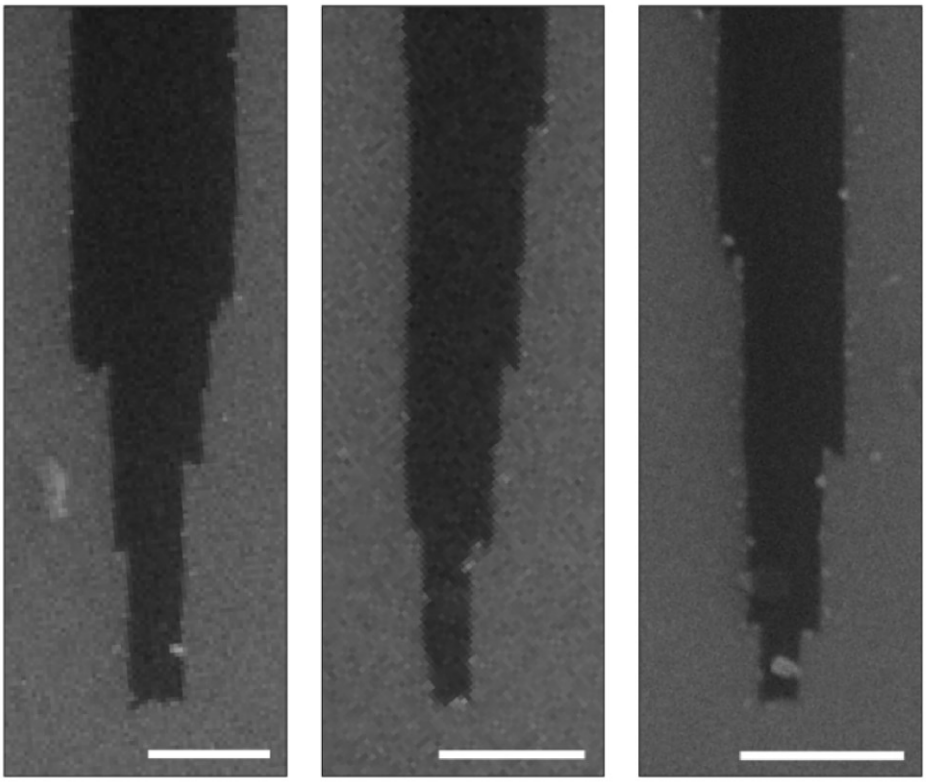

Figure 5.3. Scanning electron micrographs demonstrating tapering effects exhibited occasionally in the synthesis of MoS_2 nanoribbons. Scale bars, 500 nm.

The cause of this tapering in samples without significant H_2 driven surface reduction, as is the case with MoS_2 nanoribbons in chapter 3, is not yet known but likely is affected by the surface configuration of the P-containing. Deviation from the ideal structure is noted at narrower nanoribbons in the case of $MoSe_2$ nanoribbons as discussed in chapter 4. As can be seen in Figure 5.3, a high magnification image shows that the overall structure, while consistently smooth edged, undergoes inconsistent edge to edge width along its length with several terraced points of tapering throughout the crystal. Though this is unfortunate for consistency, it may be an avenue to achieving ultra-narrow nanoribbons and just as importantly allows us to study width-dependent phenomena on a single nanoribbon moiety. $MoSe_2$ nanoribbons exhibit similar smooth edge characteristics as shown in Fig. 4.5. However, this incidence of tapering profiles appears tied to carrier gas concentration as talked about in Chapter 4.

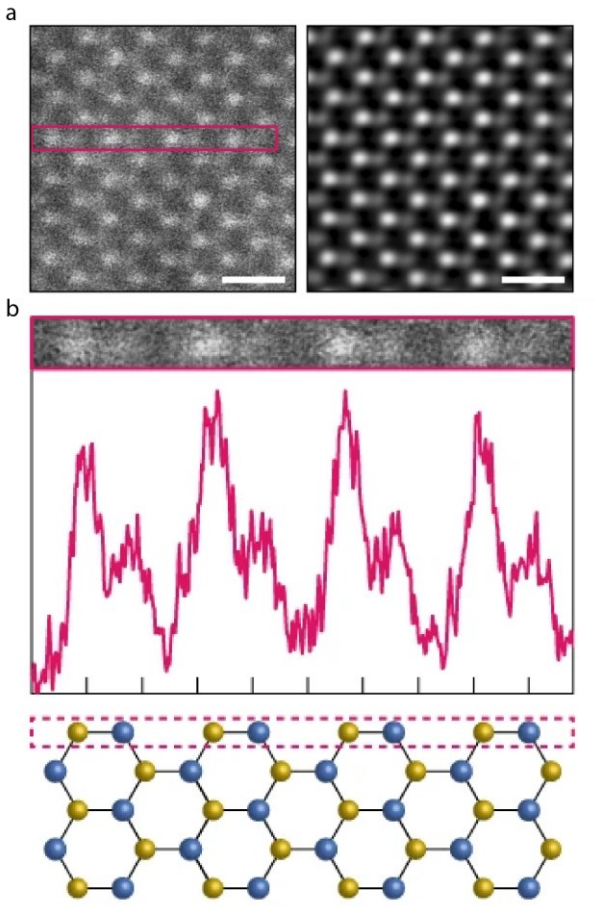

Figure 5.4. (a) Raw (left) and FFT-filtered (right) atomic resolution High angle annular dark field imaging (HAADF)-STEM images of a 1D MoS_2 nanoribbon sample. Scale bars, 5 Å. (b) HAADF intensity line scan across a row of atoms from the boxed region in (a). Illustration showing where the boxed region in (a) arrives in a lattice of MoS_2.

The one-dimensional MoS_2 nanoribbons show a 2H phase as demonstrated by high resolution STEM imaging (Fig 5.4). The hexagonal lattice shown in these data demonstrate a 2H phase MoS_2 material.[26] Integration of the STEM-HAADF intensity over a row of atoms in this lattice along the <1010>

direction shows a 2 to 1 ratio between adjacent atomic pairs. These patterns are consistent with Z-contrast exhibited from 2D 2H phase MoS_2 found previously.

Additionally, we note the majority of nanoribbons synthesized are of monolayer quality. An atomic force micrograph demonstrates a height of ~ 1.1 nm, which is indicative of monolayer MoS_2 formation (Fig 5.5). The surface roughness shown by the atomic force micrograph is much lower than expected on a purely SiO_2 substrate. This atomic force microscopy result shows that there are most likely no multi-layer growth from the genesis point of the nanoribbon or any unreacted oxides on the nanoribbons.

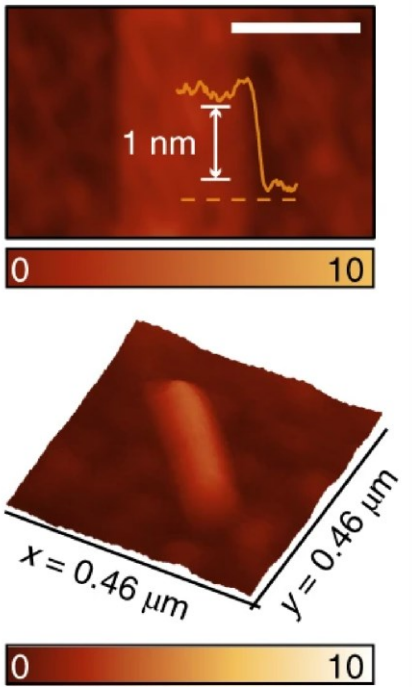

Figure 5.5. (a) Atomic force micrograph of a MoS_2 nanoribbon depicting a monolayer quality material. Scale bar, 250 nm. (b) 3d rendering of the profile generated through AFM showing a smooth quality in the nanoribbon.

STEM images also display an exceptionally phase pure material which possess extremely few defects (Fig 5.6). Fast Fourier transform patterns show a highly crystalline material of hexagonal structure that is indicative of MoS_2. Additionally, we note the mechanical flexibility of these nanoribbons as Fig. 5.6 demonstrates a one-dimensional moiety stretching across a grid holder and maintaining integrity as a 2H-MoS_2 crystal. Further, particular interest in almost all 1D materials centers around the edge quality of these materials.

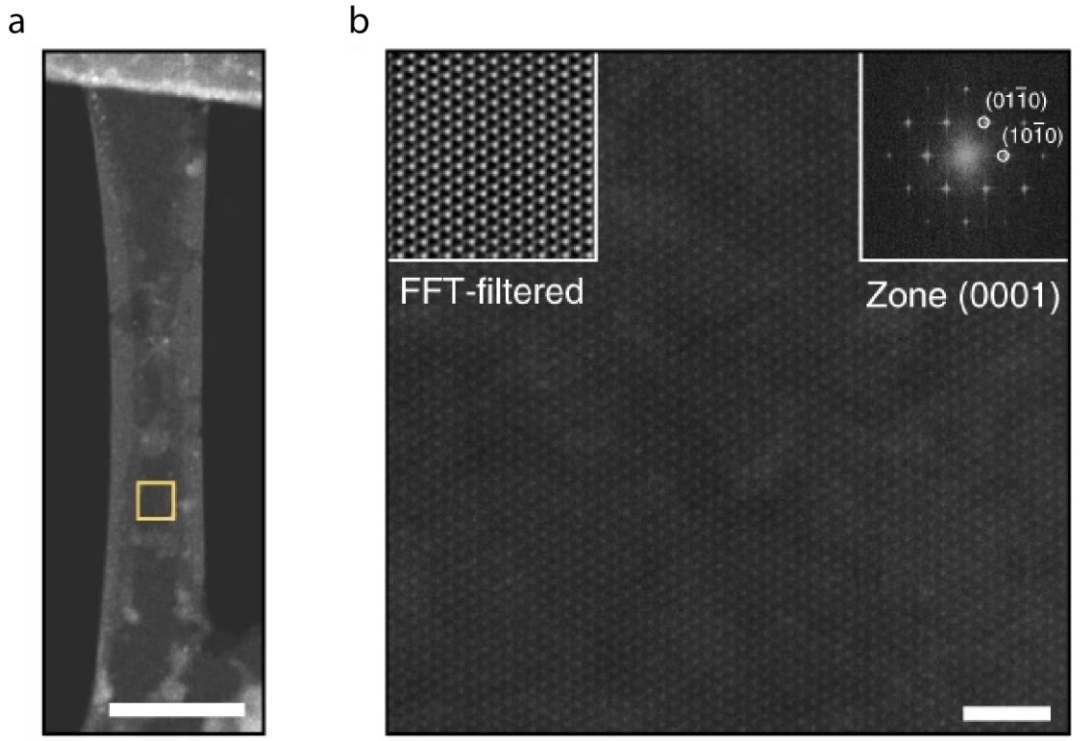

Figure 5.6. (a) Low-magnification scanning tunneling electron micrograph of a MoS_2 nanoribbon suspended over a hole on a grid. Scale bar, 100 nm. (b) HAADF-STEM image taken on the yellow boxed region in (a). Scale bar, 2 nm. Insets: (left) FFT-filtered image of the raw lattice data encompassed by the inset; (right) FFT of the raw lattice data shown in this panel, demonstrating highly crystalline quality.

High-resolution STEM images show zigzag edge configuration which is consistent with the majority of 2D TMDs and other 1D TMD nanoribbons that have not been specifically targeted for different edge structures (Fig 5.7).[27–29] These zigzag edges have been theorized and experimentally tested to be attractive features for electronic, optical and magnetic applications.[30–34] An

important parameter in assigning quality to the morphology of the edge structure is the edge deviation along a nanoribbon's length. The high quality of the edge character in these nanoribbons terms of its spatial edge variation is equal to or better than top-down fabrication methods and comparable to 2D MoS_2, with edge deviation no greater than 5 nm (Fig 5.7).[35–38] These near pristine edges may allow this technique to supersede other techniques as an avenue in construction of viable devices where edge fidelity is a crucial metric. Further, the folded edge exhibited Moire interference patterns with the underlying section of nanoribbon that the edge folded over. These Moire interference patterns are known to afford great control over excitonic characteristics in 2D materials as seen previously.[39–44] Those breakthroughs may be translated to TMD nanoribbons constructed through this method in the future. It is important to note, however, that it is unclear if the folded edge occurred due to mechanical strain during the transfer process to a grid suitable for transmission electron microscopy imaging from its growth substrate or if there was a natural folding process during the reaction. At present it seems unlikely that this folding occurred during the synthesis, but the pristine native edge quality does afford opportunities to specifically tailor or functionalize nanoribbons in the future to engage in spontaneous edge curling.

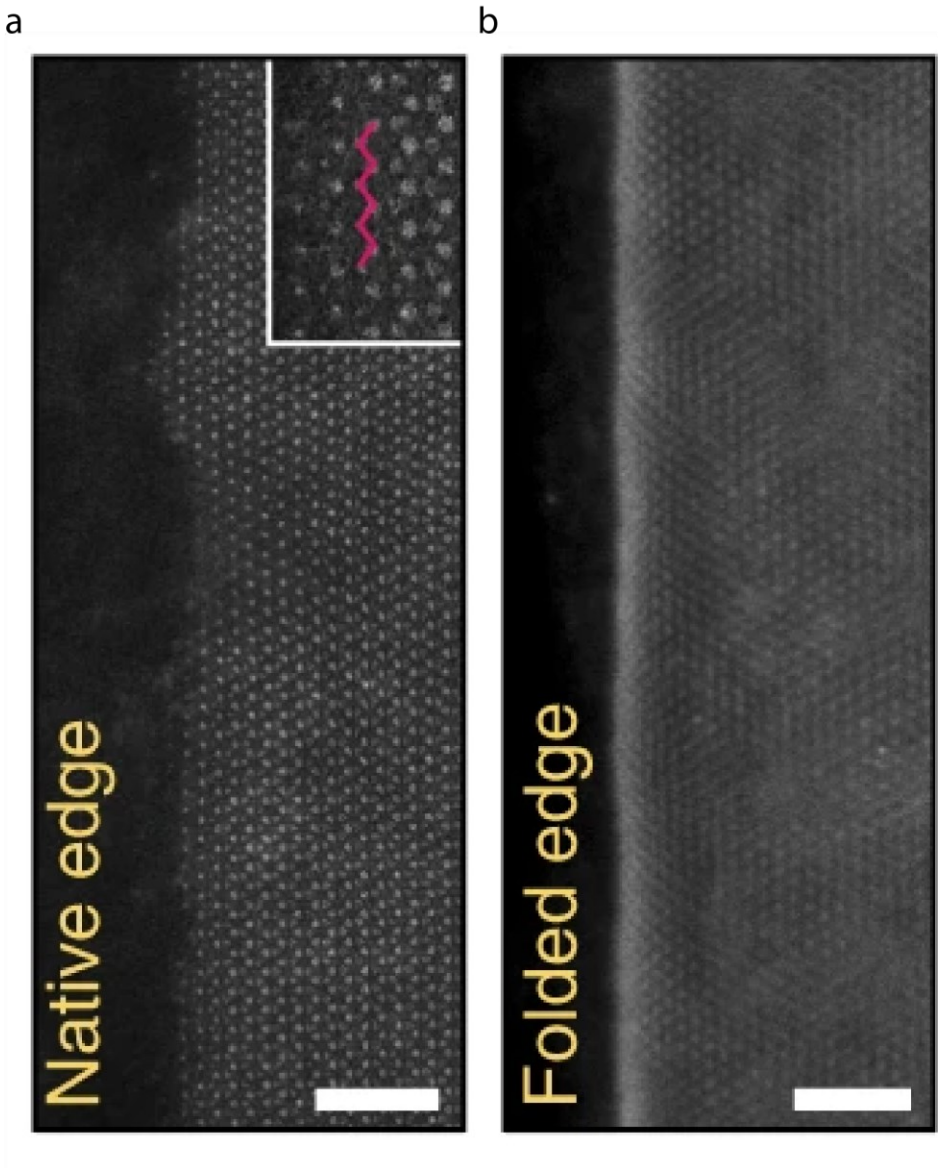

Figure 5.7. (a) HAADF-STEM image of a native edge of a MoS_2 nanoribbon. Scale bar, 2 nm. (b) HAADF-STEM image of a folded edge of a MoS_2 nanoribbon. Scale bar, 2 nm.

These bottom-up grown materials also demonstrate remarkable optical properties. First, Raman spectra indicate a monolayer quality for the 2D MoS_2 due to a A_{1g} and E_{2g} Raman mode separation of ~ 19 cm^{-1} (Fig 5.8).[45–47] However,

the one-dimensional MoS_2 nanoribbon assayed here possesses a Raman peak separation of ~ 24 cm^{-1} indicative of a 4-layer thick MoS_2 nanoribbon.[48] 2D MoS_2 is known to have a PL emission peak around 680 nm. However, there is a demonstrable 50 meV blue shift in the PL emission compared to the 2D variant in these MoS_2 nanoribbons (Figure 5.8).[49–52]

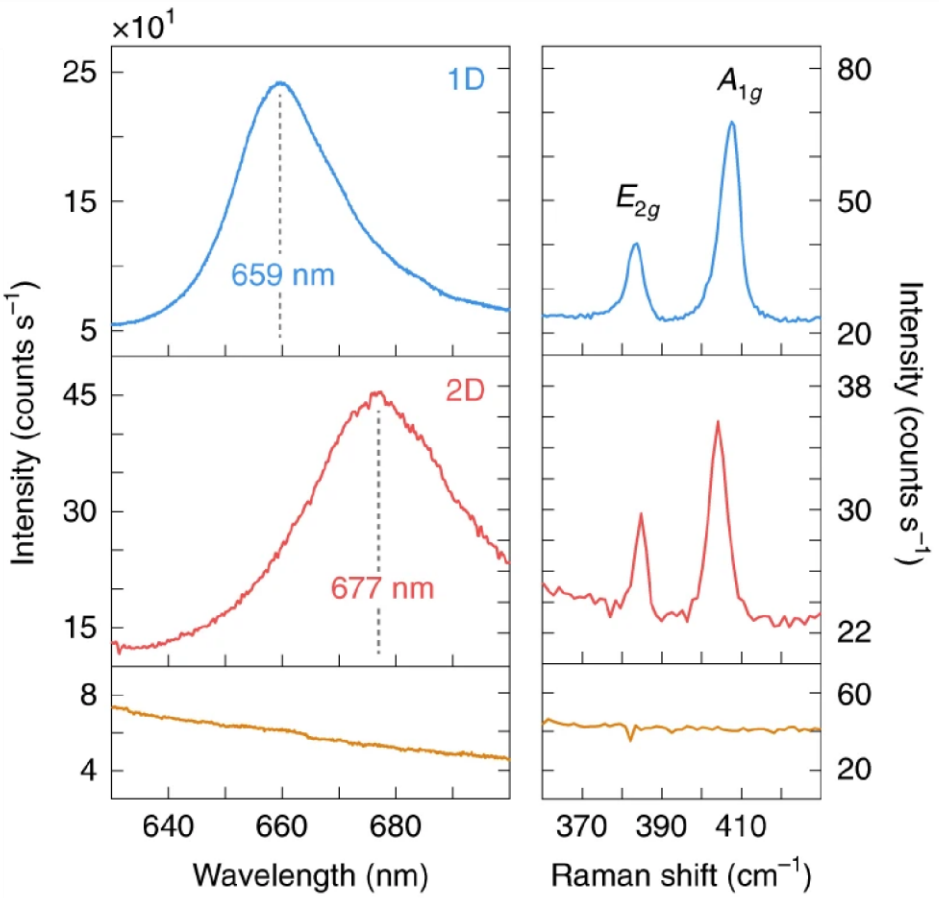

Figure 5.8. Photoluminescence and Raman spectra for 1D MoS_2 (blue, top), 2D MoS_2 (red, middle), and the Si-P_x substrate (brown, bottom). Photoluminescence spectra is blue shifted in the 1D MoS_2 nanoribbon ~ 60 meV relative to the 2D spectrum. Raman signatures show monolayer quality in both materials. The Si-P_x substrate gives no appreciable photoluminescence or Raman contribution.

Further, the brown trace in Figure 5.8 shows the lack of PL emission from the Si-P_x surface without any crystals grown on it. This precludes the surface exhibiting a strong PL emission that contributes to the shift. Though the neutral A exciton or the negative A^- trion has been shown to shift in response to crystal dielectric environment, it is unlikely that is the cause of this PL shift because the PL shift was observed both on 1D crystals grown on neat Si-P_x substrates and after transferring to clean SiO_2 substrates.[51,53–56] Notably, the PL intensity does not significantly attenuate in the same way as 2D MoS_2. PL intensity in 1D MoS_2 remained relatively constant up to 4 layers. This finding indicates a differing emission mechanism than encountered from MoS_2 2D monolayers which have rapid attenuation of PL intensity when materials have greater than 1 layer.[57] We also note that the peak positions of the 1D crystal and its intensity were relatively unchanged as spectral measurement was taken over 10 minutes. The emissive properties of these nanoribbons are both gradual and consistently correlated to width changing. For example, a tapered nanoribbon shows three distinctly different peak PL emission energy as a function of nanoribbon width as discussed later. We note that although it is unlikely to be the cause of all of the blue-shifted PL, strain in low-dimensional TMDs has caused shifts in spectral response.[58–62] However, as the nanoribbons exhibit the same magnitude PL shift for neat and transferred samples it is unlikely this is a major factor in the PL shift.

To confirm that this PL shift was due to the changing dimensionality and not chemical composition, STEM-EELS spectra were taken as shown in Fig. 5.9. This EELS spectrum shows two key features. First, The Mo and S edges are commensurate with previously reported two-dimensional MoS_2 EELS spectra acquired.[63] More importantly, however, is that we can discount P atoms incorporating into the lattice of the MoS_2 nanoribbon and thus disrupting or altering the structure and leading to new optical properties (Fig 5.9).

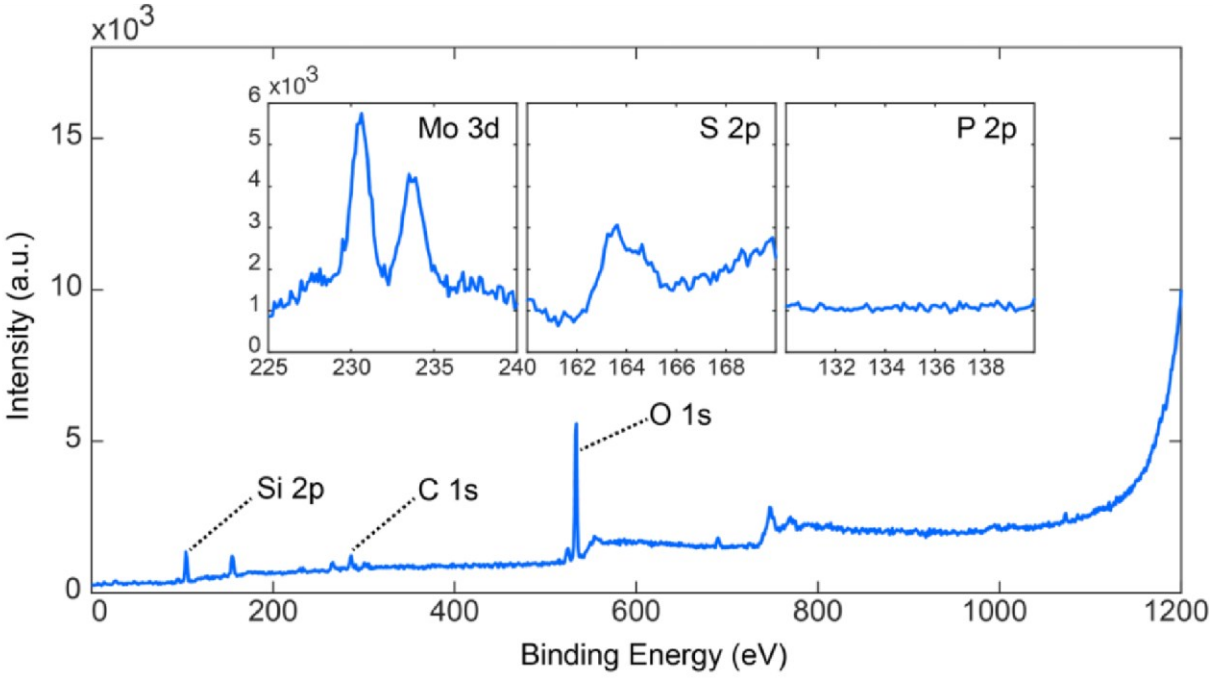

Figure 5.9. Electron energy loss spectroscopy (EELS) spectrum depicting Mo, S, and P edges of a MoS_2 nanoribbon. No P 2p edge signal is detected suggesting there is no incorporation of P atoms into the MoS_2 lattice.

This width dependance on PL energy in MoS_2 nanoribbons grown via bottom-up methods is novel but not unprecedented. Bao et al. demonstrated that in 2D monolayer regions there exists 'edge' regions up to 300 nm that exhibited anomalous small optical shifts compared to the interior of the material (Fig. 5.10).[64] Additionally, the intensity of the edge regions was significantly attenuated compared to the interior of the 2D flake.

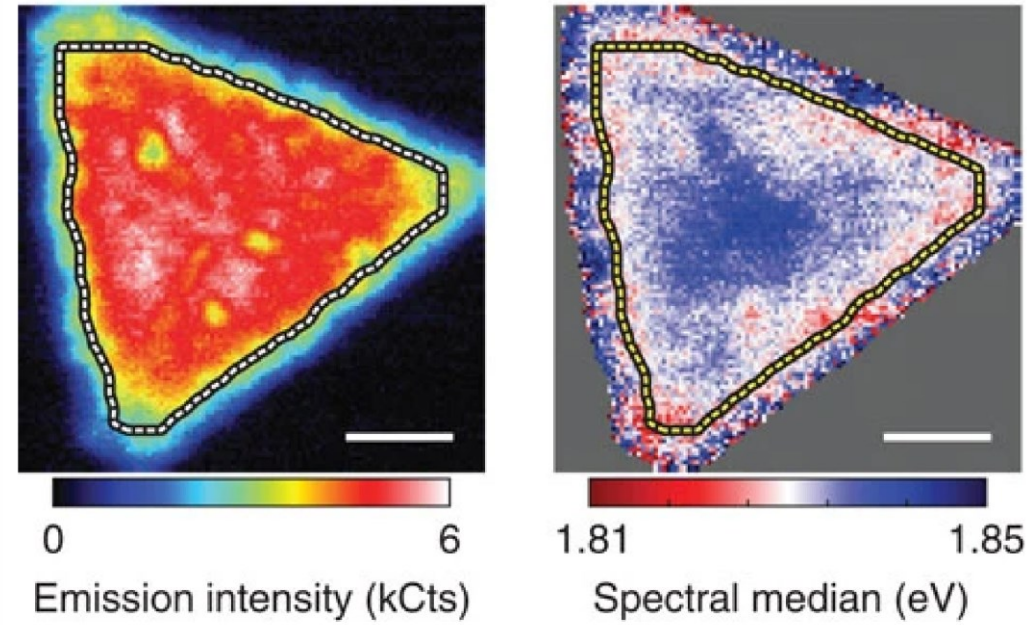

Figure 5.10.[64] Nano photoluminescence images of emission intensity and spectral median of a single domain of monolayer MoS_2. Images depict different emission intensities and a shift in spectral median in an edge region ~ 300 nm wide. Scale bars, 1 μm.

When comparing this result to our nanoribbons, where the entire edge-to-edge width is on the same order of magnitude as the 'edge' region exhibited in the prior 2D work, it is likely that new edge-mediated optical emission pathways

become available in a similar manner to the edge region of 2D TMD crystals. The interior of the 2D crystals likely emit at defect centers within the crystals as the lifetimes of the exciton is insufficient to reach the edge in a large 2D crystal.[65–69] However, in our 1D nanoribbon of relatively narrow width, the entirety of the excitons can possibly reach the edge of the nanoribbon for new optical pathways. In 2D morphologies, PL emission attenuates rapidly after the monolayer limit to bulk-like (none) PL at tri or quad layers. However, we see the robustness of the PL emission in these nanoribbons compared to their 2D cousins. This reinforces the idea that novel emissive pathways dominate at relevant widths of nanoribbons synthesized using the designer surface method.

To further investigate the photoluminescent properties of the MoS_2 nanoribbons, we turned to far field PL mapping of both 1D nanoribbon and 2D triangular moieties (Fig. 5.11). In these data we note that the emissive energies exhibited by the 2D flake was relatively constant across its area. This is not opposing the data seen in Fig. 5.10, but the technique used here was coarser and edge effects were not well resolved. In the 1D moiety we note a changing emission energy as a function of width down the length of the nanoribbon. Particularly in Fig. 5.11 (b), a tapered nanoribbon was examined in the PL mapping as shown and had 3 different spot PL scans taken at different points in its width. The spectral data clearly demonstrates that the shift in the PL spectra is

gradual with the changing nanoribbon width, indicating reduced dimensionality is the cause of the initial PL shifts seen in Fig. 5.8.

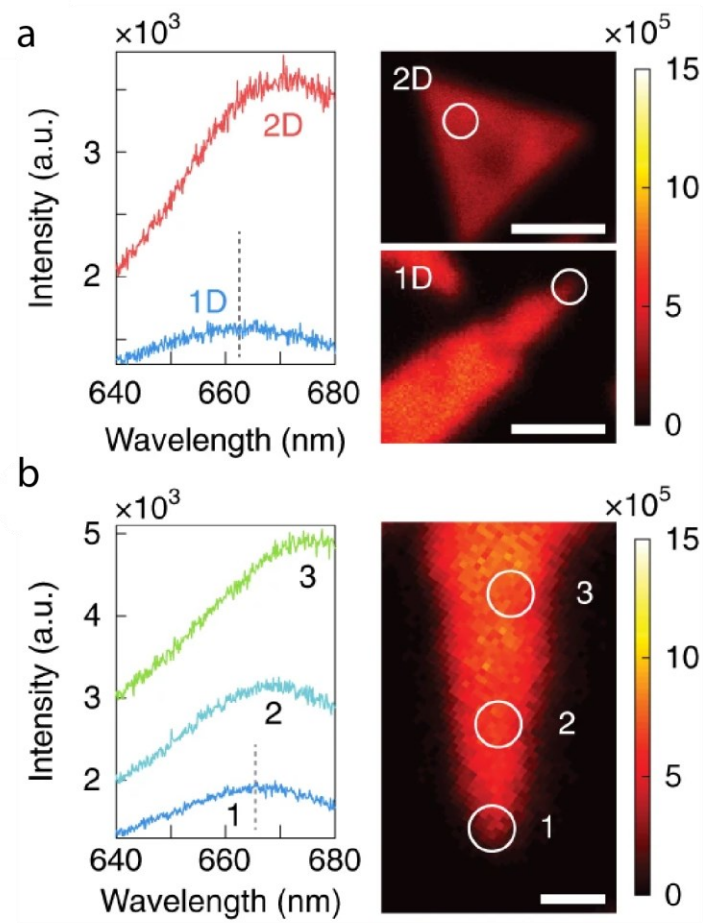

Figure 5.11. (a) Photoluminescence mapping (right) of both 1D and 2D MoS_2 moieties. Photoluminescence spot scans (left) taken at points denoted by the circle in the right images. Scale bars, 2 μm. (b) Photoluminescence mapping (right) of successively narrower portions of a tapering nanoribbon. Photoluminescence spot scans (left) taken at points denoted by the circle in the right images. Scale bar, 1 μm.

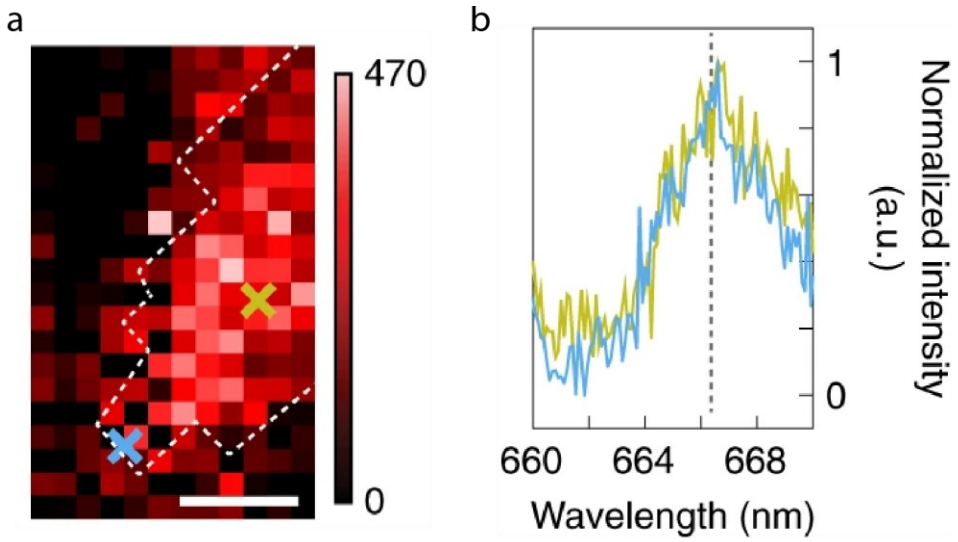

Figure 5.12. (a) Near field scanning optical (NSOM) map of a tapered nanoribbon that show consistent emission energy across its width. Scale bar, 100 nm. (b) Two spot scan photoluminescence measurements taken at the points denoted by the green and blue crosses, respectively.

However, far-field PL is a relatively coarse method in assigning differences between edge and interior regions when the dimensionality of the material is limited, as in this case. Spot sizes in the far field PL mapping approach 500 nm in diameter, thus limiting the ability to investigate how the MoS_2 nanoribbons behave at narrower limits as the entirety of the far-field probe consumed the whole width of the nanoribbon at the narrowest regimes as seen in spot 3 in Fig. 5.11. To further probe this PL dependence on width phenomenon and ascertain whether the nanoribbon exhibited uniform emission or if the edges deviated from the interior, as shown in large 2D flakes, we utilized near field scanning optical microscopy techniques. Figure 5.12 shows the near field

microscopy map of the end of a tapered nanoribbon area of a width ~ 200 nm. Notably, the emission energy is still around ~ 660 nm for the nanoribbon as a whole, but importantly has uniform emission across the width of the nanoribbon. The resolution of the NSOM method employed was ~ 20 nm and each step is in line with the same emission wavelength. Additionally, spot scans at the very tip of the nanoribbon where the width is narrowest shows a commensurate emission energy as the 200 nm width region. This may indicate that there is a limit to the dimensionally instigated shift in the PL energy.

To further probe the optical deviation from the 2D variants, we wanted to explore other TMD compositions to confirm that this phenomenon was not restricted to MoS_2.

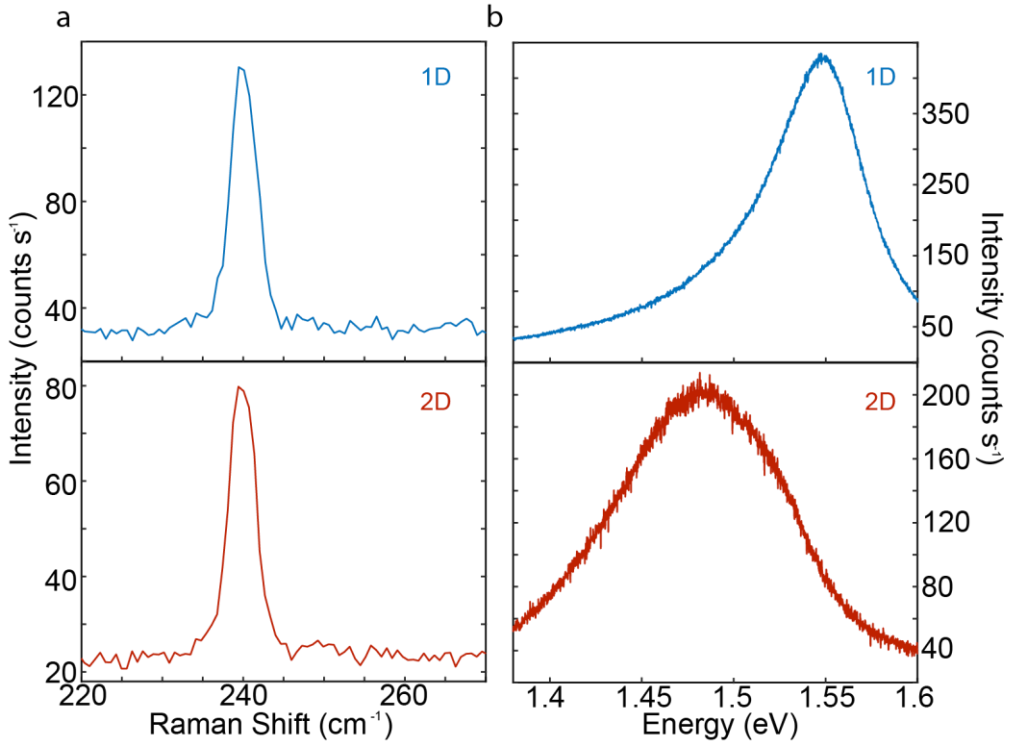

Figure 5.13. (a) Photoluminescence and Raman spectra of 1D $MoSe_2$ (top, blue) and 2D $MoSe_2$ (bottom, red). Raman spectra show a similar $MoSe_2$ A_{1g} signature. Photoluminescence emission is shifted ~ 50 meV in the 1D $MoSe_2$ with respect to its 2D variant.

Figure 5.13 shows PL spectra of 2D and 1D $MoSe_2$ nanoribbons where we note the same trend in a blue-shifted emission of ~ 60 meV from the 2D monolayer to 1D nanoribbon.[50,52,70,71] This was done on a sample of on average 400 nm width $MoSe_2$ nanoribbons. The $MoSe_2$ nanoribbons assayed here appear to be of monolayer quality due to the peak position of their A_{1g} Raman mode at ~ 240 cm^{-1}.[46,52,72,73] Since this optical behavior holds across different TMD compositions, the optical phenomena most likely is occurring due to the change in

dimensionality. Further optical control may be exhibited by ultra-narrow (< 20 nm) nanoribbons constructed with this method.

Electronically these materials exhibit different properties from the 2D variants as well. While device processing of these materials is not as trivial as large 2D sheets, Au contacts were deposited onto the substrate with a Ti adhesion layer. The electronic response for a field effect transistor configuration was consistent with expectation. Figure 5.14 shows a I-V characteristic as several different source-drain voltages. These characteristics show a modest performance in drain current as a function of voltage, however, the ability to exhibit transistor behavior in these dimensionally restricted materials differently than commensurate 2D materials shows there is opportunity to tune 1D materials for electronic applications beyond what 2D TMDs can offer.

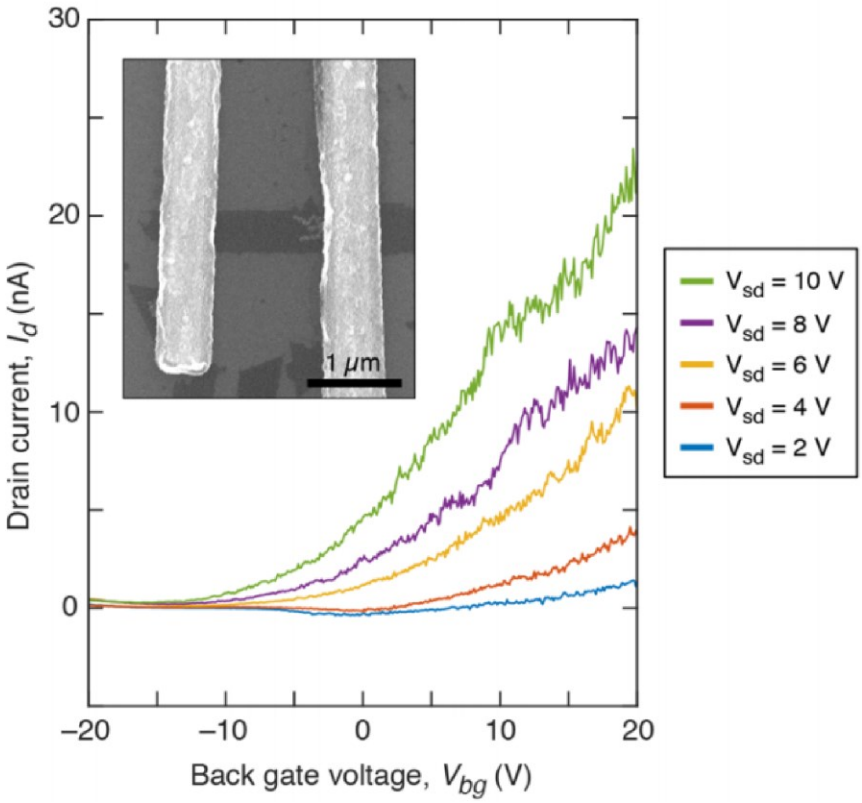

Figure 5.14. Electronic response of a MoS_2 nanoribbon between two Au contacts exhibiting field effect transistor behavior. Five I_d-V_{bg} transfer characteristics were obtained for source-drain biases of 2, 4, 6, 8, and 10 V. Inset: High resolution scanning electron micrograph image of the 1D MoS_2 nanoribbon field effect device.

In this work we identified several attributes of MoS_2 and $MoSe_2$ nanoribbons including optical, electrical, and physical properties. Notably, these nanoribbons exhibit high quality edges, a notable, blue-shifted photoluminescence emission, and optical resiliency to multiple layers not seen in 2D TMDs. These properties may lead to TMD nanoribbons gaining traction as a material system for a wide array of useful technological applications. Further, the

future application of vertical heterostructures fabricated out of TMD nanoribbons offers opportunities to probe the effect of confinement in heterostructure phenomena such as Moire superlattices.

5.4 References

(1) Colomés, E.; Franz, M. Antichiral Edge States in a Modified Haldane Nanoribbon. *Phys. Rev. Lett.* **2018**, *120* (8), 086603.

(2) Chen, R.; Zhao, T.; Wu, W.; Wu, F.; Li, L.; Qian, J.; Xu, R.; Wu, H.; Albishri, H. M.; Al-Bogami, A. S.; El-Hady, D. A.; Lu, J.; Amine, K. Free-Standing Hierarchically Sandwich-Type Tungsten Disulfide Nanotubes/Graphene Anode for Lithium-Ion Batteries. *Nano Lett.* **2014**, *14* (10), 5899–5904.

(3) Fathipour, S.; Remskar, M.; Varlec, A.; Ajoy, A.; Yan, R.; Vishwanath, S.; Rouvimov, S.; Hwang, W. S.; Xing, H. G.; Jena, D.; Seabaugh, A. Synthesized Multiwall MoS_2 Nanotube and Nanoribbon Field-Effect Transistors. *Appl. Phys. Lett.* **2015**, *106* (2), 022114.

(4) Strojnik, M.; Kovic, A.; Mrzel, A.; Buh, J.; Strle, J.; Mihailovic, D. MoS_2 Nanotube Field Effect Transistors. *AIP Adv.* **2014**, *4* (9), 097114.

(5) Bai, Y.; Zhang, R.; Ye, X.; Zhu, Z.; Xie, H.; Shen, B.; Cai, D.; Liu, B.; Zhang, C.; Jia, Z.; Zhang, S.; Li, X.; Wei, F. Carbon Nanotube Bundles with Tensile Strength over 80 GPa. *Nat. Nanotechnol.* **2018**, *13* (7), 589–595.

(6) Xu, K.; Wang, F.; Wang, Z.; Zhan, X.; Wang, Q.; Cheng, Z.; Safdar, M.; He, J. Component-Controllable $WS_{2(1-x)}Se_{2x}$ Nanotubes for Efficient Hydrogen Evolution Reaction. *ACS Nano* **2014**, *8* (8), 8468–8476.

(7) Zhang, S.; Jin, H.; Long, C.; Wang, T.; Peng, R.; Huang, B.; Dai, Y. MoSSe Nanotube: A Promising Photocatalyst with an Extremely Long Carrier Lifetime. *J. Mater. Chem. A* **2019**, *7* (13), 7885–7890.

(8) Zhang, Y. J.; Ideue, T.; Onga, M.; Qin, F.; Suzuki, R.; Zak, A.; Tenne, R.; Smet, J. H.; Iwasa, Y. Enhanced Intrinsic Photovoltaic Effect in Tungsten Disulfide Nanotubes. *Nature* **2019**, *570* (7761), 349–353.

(9) Botello-Méndez, A. R.; López-Urías, F.; Terrones, M.; Terrones, H. Metallic and Ferromagnetic Edges in Molybdenum Disulfide Nanoribbons. *Nanotechnology* **2009**, *20* (32), 325703.

(10) Durr, R. A.; Haberer, D.; Lee, Y.-L.; Blackwell, R.; Kalayjian, A. M.; Marangoni, T.; Ihm, J.; Louie, S. G.; Fischer, F. R. Orbitally Matched Edge-Doping in Graphene Nanoribbons. *J. Am. Chem. Soc.* **2018**, *140* (2), 807–813.

(11) Orlof, A.; Ruseckas, J.; Zozoulenko, I. V. Effect of Zigzag and Armchair Edges on the Electronic Transport in Single-Layer and Bilayer Graphene Nanoribbons with Defects. *Phys. Rev. B* **2013**, *88* (12), 125409.

(12) Cai, Y.; Zhang, G.; Zhang, Y.-W. Polarity-Reversed Robust Carrier Mobility in Monolayer MoS_2 Nanoribbons. *J. Am. Chem. Soc.* **2014**, *136* (17), 6269–6275.

(13) Chen, K.; Deng, J.; Ding, X.; Sun, J.; Yang, S.; Liu, J. Z. Ferromagnetism of 1T′-MoS_2 Nanoribbons Stabilized by Edge Reconstruction and Its Periodic Variation on Nanoribbons Width. *J. Am. Chem. Soc.* **2018**, *140* (47), 16206–16212.

(14) Dias, A. C.; Qu, F.; Azevedo, D. L.; Fu, J. Band Structure of Monolayer Transition-Metal Dichalcogenides and Topological Properties of Their Nanoribbons: Next-Nearest-Neighbor Hopping. *Phys. Rev. B* **2018**, *98* (7), 075202.
(15) Pan, H.; Zhang, Y.-W. Edge-Dependent Structural, Electronic and Magnetic Properties of MoS_2 Nanoribbons. *J. Mater. Chem.* **2012**, *22* (15), 7280–7290.
(16) Ridolfi, E.; Lima, L. R. F.; Mucciolo, E. R.; Lewenkopf, C. H. Electronic Transport in Disordered MoS_2 Nanoribbons. *Phys. Rev. B* **2017**, *95* (3), 035430.
(17) Cheng, F.; Xu, H.; Xu, W.; Zhou, P.; Martin, J.; Loh, K. P. Controlled Growth of 1D $MoSe_2$ Nanoribbons with Spatially Modulated Edge States. *Nano Lett.* **2017**, *17* (2), 1116–1120.
(18) Zhang, H.; Li, X.-B.; Liu, L.-M. Tunable Electronic and Magnetic Properties of WS_2 Nanoribbons. *J. Appl. Phys.* **2013**, *114* (9), 093710.
(19) Pandey, N.; Kumar, A.; Chakrabarti, S. First Principle Study of Temperature-Dependent Magnetoresistance and Spin Filtration Effect in WS_2 Nanoribbon. *ACS Appl. Mater. Interfaces* **2019**, *11* (42), 39248–39253.
(20) Wang, M.; Pang, Y.; Liu, D. Y.; Zheng, S. H.; Song, Q. L. Tuning Magnetism by Strain and External Electric Field in Zigzag Janus MoSSe Nanoribbons. *Comput. Mater. Sci.* **2018**, *146*, 240–247.
(21) Cui, P.; Choi, J.-H.; Chen, W.; Zeng, J.; Shih, C.-K.; Li, Z.; Zhang, Z. Contrasting Structural Reconstructions, Electronic Properties, and Magnetic Orderings along Different Edges of Zigzag Transition Metal Dichalcogenide Nanoribbons. *Nano Lett.* **2017**, *17* (2), 1097–1101.
(22) Zhang, H.; Zhao, X.; Gao, Y.; Wang, H.; Wang, T.; Wei, S. Electronic and Magnetic Properties of $MoSe_2$ Armchair Nanoribbons Controlled by the Different Edge Structures. *Superlattices Microstruct.* **2018**, *115*, 30–39.
(23) Yu, L.; Sun, S.; Ye, X. Electronic and Magnetic Properties of the Janus MoSSe/WSSe Superlattice Nanoribbon: A First-Principles Study. *Phys. Chem. Chem. Phys.* **2020**, *22* (4), 2498–2508.
(24) Chen, Z.; Cummins, D.; Reinecke, B. N.; Clark, E.; Sunkara, M. K.; Jaramillo, T. F. Core–Shell MoO_3–MoS_2 Nanowires for Hydrogen Evolution: A Functional Design for Electrocatalytic Materials. *Nano Lett.* **2011**, *11* (10), 4168–4175.
(25) Wu, J.-B.; Zhao, H.; Li, Y.; Ohlberg, D.; Shi, W.; Wu, W.; Wang, H.; Tan, P.-H. Monolayer Molybdenum Disulfide Nanoribbons with High Optical Anisotropy. *Adv. Opt. Mater.* **2016**, *4* (5), 756–762.
(26) Ataca, C.; Şahin, H.; Ciraci, S. Stable, Single-Layer MX_2 Transition-Metal Oxides and Dichalcogenides in a Honeycomb-Like Structure. *J. Phys. Chem. C* **2012**, *116* (16), 8983–8999.
(27) Xu, H.; Ding, Z.; Nai, C. T.; Bao, Y.; Cheng, F.; Tan, S. J. R.; Loh, K. P. Controllable Synthesis of 2D and 1D MoS_2 Nanostructures on Au Surface. *Adv. Funct. Mater.* **2017**, *27* (19), 1603887.
(28) Chen, Q.; Li, H.; Xu, W.; Wang, S.; Sawada, H.; Allen, C. S.; Kirkland, A. I.; Grossman, J. C.; Warner, J. H. Atomically Flat Zigzag Edges in Monolayer MoS_2 by Thermal Annealing. *Nano Lett.* **2017**, *17* (9), 5502–5507.

(29) Wu, D.; Shi, J.; Zheng, X.; Liu, J.; Dou, W.; Gao, Y.; Yuan, X.; Ouyang, F.; Huang, H. CVD Grown MoS_2 Nanoribbons on MoS_2 Covered Sapphire(0001) Without Catalysts. *Phys. Status Solidi RRL* **2019**, *13* (7), 1900063.
(30) Kou, L.; Tang, C.; Zhang, Y.; Heine, T.; Chen, C.; Frauenheim, T. Tuning Magnetism and Electronic Phase Transitions by Strain and Electric Field in Zigzag MoS_2 Nanoribbons. *J. Phys. Chem. Lett.* **2012**, *3* (20), 2934–2941.
(31) Xiao, S.-L.; Yu, W.-Z.; Gao, S.-P. Edge Preference and Band Gap Characters of MoS_2 and WS_2 Nanoribbons. *Surf. Sci.* **2016**, *653*, 107–112.
(32) Yang, S.; Li, D.; Zhang, T.; Tao, Z.; Chen, J. First-Principles Study of Zigzag MoS_2 Nanoribbon as a Promising Cathode Material for Rechargeable Mg Batteries. *J. Phys. Chem. C* **2012**, *116* (1), 1307–1312.
(33) Li, Y.; Wu, D.; Zhou, Z.; Cabrera, C. R.; Chen, Z. Enhanced Li Adsorption and Diffusion on MoS_2 Zigzag Nanoribbons by Edge Effects: A Computational Study. *J. Phys. Chem. Lett.* **2012**, *3* (16), 2221–2227.
(34) Li, Y.; Zhou, Z.; Zhang, S.; Chen, Z. MoS_2 Nanoribbons: High Stability and Unusual Electronic and Magnetic Properties. *J. Am. Chem. Soc.* **2008**, *130* (49), 16739–16744.
(35) Shi, Y.; Li, H.; Li, L.-J. Recent Advances in Controlled Synthesis of Two-Dimensional Transition Metal Dichalcogenides via Vapour Deposition Techniques. *Chem. Soc. Rev.* **2015**, *44* (9), 2744–2756.
(36) Wang, X.; Dai, H. Etching and Narrowing of Graphene from the Edges. *Nat. Chem.* **2010**, *2* (8), 661–665.
(37) Abbas, A. N.; Liu, G.; Liu, B.; Zhang, L.; Liu, H.; Ohlberg, D.; Wu, W.; Zhou, C. Patterning, Characterization, and Chemical Sensing Applications of Graphene Nanoribbon Arrays Down to 5 nm Using Helium Ion Beam Lithography. *ACS Nano* **2014**, *8* (2), 1538–1546.
(38) Stanford, M. G.; Pudasaini, P. R.; Cross, N.; Mahady, K.; Hoffman, A. N.; Mandrus, D. G.; Duscher, G.; Chisholm, M. F.; Rack, P. D. Tungsten Diselenide Patterning and Nanoribbon Formation by Gas-Assisted Focused-Helium-Ion-Beam-Induced Etching. *Small Methods* **2017**, *1* (4), 1600060.
(39) Bai, Y.; Zhou, L.; Wang, J.; Wu, W.; McGilly, L. J.; Halbertal, D.; Lo, C. F. B.; Liu, F.; Ardelean, J.; Rivera, P.; Finney, N. R.; Yang, X.-C.; Basov, D. N.; Yao, W.; Xu, X.; Hone, J.; Pasupathy, A. N.; Zhu, X.-Y. Excitons in Strain-Induced One-Dimensional Moiré Potentials at Transition Metal Dichalcogenide Heterojunctions. *Nat. Mater.* **2020**, 1–6.
(40) Choi, J.; Hsu, W.-T.; Lu, L.-S.; Sun, L.; Cheng, H.-Y.; Lee, M.-H.; Quan, J.; Tran, K.; Wang, C.-Y.; Staab, M.; Jones, K.; Taniguchi, T.; Watanabe, K.; Chu, M.-W.; Gwo, S.; Kim, S.; Shih, C.-K.; Li, X.; Chang, W.-H. Moiré Potential Impedes Interlayer Exciton Diffusion in van Der Waals Heterostructures. *Sci. Adv.* **2020**, *6* (39), eaba8866.
(41) Seyler, K. L.; Rivera, P.; Yu, H.; Wilson, N. P.; Ray, E. L.; Mandrus, D. G.; Yan, J.; Yao, W.; Xu, X. Signatures of Moiré-Trapped Valley Excitons in $MoSe_2/WSe_2$ Heterobilayers. *Nature* **2019**, *567* (7746), 66–70.

(42) Tran, K.; Moody, G.; Wu, F.; Lu, X.; Choi, J.; Kim, K.; Rai, A.; Sanchez, D. A.; Quan, J.; Singh, A.; Embley, J.; Zepeda, A.; Campbell, M.; Autry, T.; Taniguchi, T.; Watanabe, K.; Lu, N.; Banerjee, S. K.; Silverman, K. L.; Kim, S.; Tutuc, E.; Yang, L.; MacDonald, A. H.; Li, X. Evidence for Moiré Excitons in van Der Waals Heterostructures. *Nature* **2019**, *567* (7746), 71–75.
(43) Xu, Y.; Horn, C.; Zhu, J.; Tang, Y.; Ma, L.; Li, L.; Liu, S.; Watanabe, K.; Taniguchi, T.; Hone, J. C.; Shan, J.; Mak, K. F. Creation of Moiré Bands in a Monolayer Semiconductor by Spatially Periodic Dielectric Screening. *Nat. Mater.* **2021**, 1–5.
(44) Yu, H.; Liu, G.-B.; Tang, J.; Xu, X.; Yao, W. Moiré Excitons: From Programmable Quantum Emitter Arrays to Spin-Orbit–Coupled Artificial Lattices. *Sci. Adv.* **2017**, *3* (11), e1701696.
(45) Saito, R.; Tatsumi, Y.; Huang, S.; Ling, X.; Dresselhaus, M. S. Raman Spectroscopy of Transition Metal Dichalcogenides. *J. Phys.: Condens. Matter* **2016**, *28* (35), 353002.
(46) Zhang, X.; Qiao, X.-F.; Shi, W.; Wu, J.-B.; Jiang, D.-S.; Tan, P.-H. Phonon and Raman Scattering of Two-Dimensional Transition Metal Dichalcogenides from Monolayer, Multilayer to Bulk Material. *Chem. Soc. Rev.* **2015**, *44* (9), 2757–2785.
(47) Zhou, K.-G.; Withers, F.; Cao, Y.; Hu, S.; Yu, G.; Casiraghi, C. Raman Modes of MoS_2 Used as Fingerprint of van Der Waals Interactions in 2-D Crystal-Based Heterostructures. *ACS Nano* **2014**, *8* (10), 9914–9924.
(48) Lee, C.; Yan, H.; Brus, L. E.; Heinz, T. F.; Hone, J.; Ryu, S. Anomalous Lattice Vibrations of Single- and Few-Layer MoS_2. *ACS Nano* **2010**, *4* (5), 2695–2700.
(49) Splendiani, A.; Sun, L.; Zhang, Y.; Li, T.; Kim, J.; Chim, C.-Y.; Galli, G.; Wang, F. Emerging Photoluminescence in Monolayer MoS_2. *Nano Lett.* **2010**, *10* (4), 1271–1275.
(50) Han, H.-V.; Lu, A.-Y.; Lu, L.-S.; Huang, J.-K.; Li, H.; Hsu, C.-L.; Lin, Y.-C.; Chiu, M.-H.; Suenaga, K.; Chu, C.-W.; Kuo, H.-C.; Chang, W.-H.; Li, L.-J.; Shi, Y. Photoluminescence Enhancement and Structure Repairing of Monolayer $MoSe_2$ by Hydrohalic Acid Treatment. *ACS Nano* **2016**, *10* (1), 1454–1461.
(51) Scheuschner, N.; Ochedowski, O.; Kaulitz, A.-M.; Gillen, R.; Schleberger, M.; Maultzsch, J. Photoluminescence of Freestanding Single- and Few-Layer MoS_2. *Phys. Rev. B* **2014**, *89* (12), 125406.
(52) Tonndorf, P.; Schmidt, R.; Böttger, P.; Zhang, X.; Börner, J.; Liebig, A.; Albrecht, M.; Kloc, C.; Gordan, O.; Zahn, D. R. T.; Vasconcellos, S. M. de; Bratschitsch, R. Photoluminescence Emission and Raman Response of Monolayer MoS_2, $MoSe_2$, and WSe_2. *Opt. Express, OE* **2013**, *21* (4), 4908–4916.
(53) Mak, K. F.; He, K.; Lee, C.; Lee, G. H.; Hone, J.; Heinz, T. F.; Shan, J. Tightly Bound Trions in Monolayer MoS_2. *Nat. Mater.* **2013**, *12* (3), 207–211.
(54) Dubey, S.; Lisi, S.; Nayak, G.; Herziger, F.; Nguyen, V.-D.; Le Quang, T.; Cherkez, V.; González, C.; Dappe, Y. J.; Watanabe, K.; Taniguchi, T.; Magaud, L.; Mallet, P.; Veuillen, J.-Y.; Arenal, R.; Marty, L.; Renard, J.; Bendiab, N.; Coraux, J.; Bouchiat, V. Weakly Trapped, Charged, and Free Excitons in Single-Layer MoS_2 in the Presence of Defects, Strain, and Charged Impurities. *ACS Nano* **2017**, *11* (11), 11206–11216.

(55) Lin, Y.; Ling, X.; Yu, L.; Huang, S.; Hsu, A. L.; Lee, Y.-H.; Kong, J.; Dresselhaus, M. S.; Palacios, T. Dielectric Screening of Excitons and Trions in Single-Layer MoS_2. *Nano Lett.* **2014**, *14* (10), 5569–5576.
(56) Jadczak, J.; Kutrowska-Girzycka, J.; Kapuściński, P.; Huang, Y. S.; Wójs, A.; Bryja, L. Probing of Free and Localized Excitons and Trions in Atomically Thin WSe_2, WS_2, $MoSe_2$ and MoS_2 in Photoluminescence and Reflectivity Experiments. *Nanotechnology* **2017**, *28* (39), 395702.
(57) Mak, K. F.; Lee, C.; Hone, J.; Shan, J.; Heinz, T. F. Atomically Thin MoS_2: A New Direct-Gap Semiconductor. *Phys. Rev. Lett.* **2010**, *105* (13), 136805.
(58) Lin, Z.; Carvalho, B. R.; Kahn, E.; Lv, R.; Rao, R.; Terrones, H.; Pimenta, M. A.; Terrones, M. Defect Engineering of Two-Dimensional Transition Metal Dichalcogenides. *2D Mater.* **2016**, *3* (2), 022002.
(59) Kumar, S.; Kaczmarczyk, A.; Gerardot, B. D. Strain-Induced Spatial and Spectral Isolation of Quantum Emitters in Mono- and Bilayer WSe_2. *Nano Lett.* **2015**, *15* (11), 7567–7573.
(60) Yang, S.; Wang, C.; Sahin, H.; Chen, H.; Li, Y.; Li, S.-S.; Suslu, A.; Peeters, F. M.; Liu, Q.; Li, J.; Tongay, S. Tuning the Optical, Magnetic, and Electrical Properties of $ReSe_2$ by Nanoscale Strain Engineering. *Nano Lett.* **2015**, *15* (3), 1660–1666.
(61) Dhakal, K. P.; Roy, S.; Jang, H.; Chen, X.; Yun, W. S.; Kim, H.; Lee, J.; Kim, J.; Ahn, J.-H. Local Strain Induced Band Gap Modulation and Photoluminescence Enhancement of Multilayer Transition Metal Dichalcogenides. *Chem. Mater.* **2017**, *29* (12), 5124–5133.
(62) Wang, Y.; Cong, C.; Yang, W.; Shang, J.; Peimyoo, N.; Chen, Y.; Kang, J.; Wang, J.; Huang, W.; Yu, T. Strain-Induced Direct–Indirect Bandgap Transition and Phonon Modulation in Monolayer WS_2. *Nano Res.* **2015**, *8* (8), 2562–2572.
(63) Li, M.-Y.; Shi, Y.; Cheng, C.-C.; Lu, L.-S.; Lin, Y.-C.; Tang, H.-L.; Tsai, M.-L.; Chu, C.-W.; Wei, K.-H.; He, J.-H.; Chang, W.-H.; Suenaga, K.; Li, L.-J. Epitaxial Growth of a Monolayer WSe_2-MoS_2 Lateral p-n Junction with an Atomically Sharp Interface. *Science* **2015**, *349* (6247), 524–528.
(64) Bao, W.; Borys, N. J.; Ko, C.; Suh, J.; Fan, W.; Thron, A.; Zhang, Y.; Buyanin, A.; Zhang, J.; Cabrini, S.; Ashby, P. D.; Weber-Bargioni, A.; Tongay, S.; Aloni, S.; Ogletree, D. F.; Wu, J.; Salmeron, M. B.; Schuck, P. J. Visualizing Nanoscale Excitonic Relaxation Properties of Disordered Edges and Grain Boundaries in Monolayer Molybdenum Disulfide. *Nat. Commun.* **2015**, *6* (1), 7993. .
(65) Selig, M.; Berghäuser, G.; Raja, A.; Nagler, P.; Schüller, C.; Heinz, T. F.; Korn, T.; Chernikov, A.; Malic, E.; Knorr, A. Excitonic Linewidth and Coherence Lifetime in Monolayer Transition Metal Dichalcogenides. *Nat. Commun.* **2016**, *7* (1), 13279.
(66) Palummo, M.; Bernardi, M.; Grossman, J. C. Exciton Radiative Lifetimes in Two-Dimensional Transition Metal Dichalcogenides. *Nano Lett.* **2015**, *15* (5), 2794–2800.
(67) Zheng, W.; Jiang, Y.; Hu, X.; Li, H.; Zeng, Z.; Wang, X.; Pan, A. Light Emission Properties of 2D Transition Metal Dichalcogenides: Fundamentals and Applications. *Adv. Opt. Mater.* **2018**, *6* (21), 1800420.

(68) Wu, Z.; Zhao, W.; Jiang, J.; Zheng, T.; You, Y.; Lu, J.; Ni, Z. Defect Activated Photoluminescence in WSe_2 Monolayer. *J. Phys. Chem. C* **2017**, *121* (22), 12294–12299.
(69) Schuler, B.; Cochrane, K. A.; Kastl, C.; Barnard, E. S.; Wong, E.; Borys, N. J.; Schwartzberg, A. M.; Ogletree, D. F.; Abajo, F. J. G. de; Weber-Bargioni, A. Electrically Driven Photon Emission from Individual Atomic Defects in Monolayer WS_2. *Sci. Adv.* **2020**, *6* (38), eabb5988.
(70) Shaw, J. C.; Zhou, H.; Chen, Y.; Weiss, N. O.; Liu, Y.; Huang, Y.; Duan, X. Chemical Vapor Deposition Growth of Monolayer $MoSe_2$ Nanosheets. *Nano Res.* **2014**, *7* (4), 511–517.
(71) Tongay, S.; Zhou, J.; Ataca, C.; Lo, K.; Matthews, T. S.; Li, J.; Grossman, J. C.; Wu, J. Thermally Driven Crossover from Indirect toward Direct Bandgap in 2D Semiconductors: $MoSe_2$ versus MoS_2. *Nano Lett.* **2012**, *12* (11), 5576–5580.
(72) Chen, S.-Y.; Zheng, C.; Fuhrer, M. S.; Yan, J. Helicity-Resolved Raman Scattering of MoS_2, $MoSe_2$, WS_2, and WSe_2 Atomic Layers. *Nano Lett.* **2015**, *15* (4), 2526–2532.
(73) Late, D. J.; Shirodkar, S. N.; Waghmare, U. V.; Dravid, V. P.; Rao, C. N. R. Thermal Expansion, Anharmonicity and Temperature-Dependent Raman Spectra of Single- and Few-Layer $MoSe_2$ and WSe_2. *ChemPhysChem* **2014**, *15* (8), 1592–1598.